Cavitation in Nozzle of Fuel Injector and Its Effect on Discharged Liquid Jet

Prasetya, Rubby

(Degree)
博士（工学）

(Date of Degree)
2019-09-25

(Date of Publication)
2020-09-01

(Resource Type)
doctoral thesis

(Report Number)
甲第7615号

(URL)
https://hdl.handle.net/20.500.14094/D1007615

博　士　論　文

Cavitation in Nozzle of Fuel Injector and Its Effect on Discharged Liquid Jet

(燃料インジェクタ内キャビテーション挙動の解析と液体噴流に及ぼす影響)

令和元年０８月

神戸大学大学院海事科学研究科
RUBBY PRASETYA

DEDICATION

For my parents

ACKNOWLEDGEMENTS

This dissertation was written with the support and guidance of many people. First and foremost, I would like to thank Prof. Akira Sou, my academic supervisor. I appreciate all of his contributions of time, ideas, and funding during the course of my study. I am also thankful for all the examples he has provided in how one should act in the world of academia. I would also like to thank the rest of my thesis committee, Profs. Shigeru Nishio and Tomohisa Dan for all of their insightful comments and discussion during the writing process of this dissertation.

My sincere thanks also goes to Prof. Seoksu Moon of Inha University. His expertise in x-ray phase contrast imaging has helped me numerous times during manuscript preparations of my x-ray papers. I also thank Drs. Raditya Hendra Pratama and Weidi Huang of National Institute of Advanced Industrial Science and Technology (AIST), who gave me access to the research facilities and equipment needed to conduct the x-ray imaging experiments. In addition, I also extend my gratitude to Mr. Nobuhiro Yasuda of Japan Synchrotron Radiation Research Institute (JASRI) for his technical assistance during the x-ray imaging experiments.

I also thank Profs. Keiya Nishida, Akira Nakashima, Yoichi Ogata, and Ms. Yukika Kuga of Hiroshima University, as well as Dr. Junichi Oki of Japan Aerospace Exploration Agency (JAXA) for their cooperation during the tomographic stereo PIV experiments. Thanks to their assistance, I was able to give some interesting result from 3-hole mini-sac nozzle experiments.

Special thanks to Dr. Hideaki Yokohata and Messrs. Yoshiharu Ueki and Yoshitaka Wada from Mazda Motor Corporation. Their support and advice for the experimental setup and nozzle designs, in addition to the research funding they provided, has helped me for various occasions.

I would also like to express my gratitude to the Ministry of Education, Culture, Sports, Science, and Technology (MEXT) of Japan, who provided me with academic scholarship, as well as Dr. Nobuko Umeki, who helped me in securing conference funding.

Lastly, I would like to acknowledge all the student members and technical support staffs during my time in Energy and Fluid Science Laboratory. Without their invaluable help, I would not be able to finish my Ph.D. study.

TABLE OF CONTENTS

LIST OF PUBLICATIONS

This PhD dissertation is written based on the following publications:

Journal papers:

1. Rubby Prasetya, Akira Sou, Seoksu Moon, Raditya Hendra Pratama, Yoshitaka Wada, Hideaki Yokohata, "In-nozzle cavitation and discharged liquid jet during transient injection process," *Atomization and Sprays*, vol. 29, no. 2, pp. 123–141, 2019.
2. Rubby Prasetya, Akira Sou, Seoksu Moon, Raditya Hendra Pratama, Yoshitaka Wada, Hideaki Yokohata, "X-Ray Phase Contrast Imaging of Cavitation and Discharged Liquid Jet in Nozzles with Various Sizes," *Atomization and Sprays*, vol. 29, no. 1, pp. 59–78, 2019.
3. Rubby Prasetya, Akira Sou, Junichi Oki, Akira Nakashima, Yoshitaka Wada, Hideaki Yokohata, "Three-dimensional flow structure and string cavitation in a fuel injector and their effects on discharged liquid jet," *Int. J Engine Res*, 2019.

Conference papers:

1. Rubby Prasetya, Takashi Miwa, Akira Sou, Seoksu Moon, Yoshitaka Wada, Hideaki Yokohata, "X-ray Imaging of Transient Cavitation Motion in Nozzles under Steady Injection Condition," in *Proceedings of the 10th International Cavitation Symposium (CAV2018)*, 2018.
2. Rubby Prasetya, Takumi Kasahara, Kazuya Kotani, Takashi Miwa, Akira Sou, Seoksu Moon, Yoshitaka Wada, Yoshiharu Ueki, Hideaki Yokohata, "X-Ray Imaging and Measurement of Cavitation Flow in Fuel Injector Nozzles with Various Geometries," *Proceedings of the 19th Annual Conference on Liquid Atomization and Spray Systems (ILASS-Asia 2017)*, 2017.
3. Rubby Prasetya, Takashi Miwa, Akira Sou, "Effect of Nozzle Size and Ambient Pressure on Cavitation in Fuel Injector Nozzle and Liquid Jet *(燃料インジェクタ内キャビテーションと液体噴流に及ぼすノズルサイズと雰囲気圧の影響)*," *Proceedings of the 27th Internal Combustion Engine Symposium (*第 27 回内燃機関シンポジウム), 2016.
4. Rubby Prasetya, Takumi Kasahara, Takashi Miwa, Akira Sou, Yoshitaka Wada, Hideaki Yokohata, "Effect of Ambient Pressure on Cavitation in Fuel Injector Nozzle and Liquid Jet," *Proceedings of the 27th Annual Conference on Liquid Atomization and Spray Systems (ILASS-Europe 2016)*, 2016.
5. Rubby Prasetya, Makoto Mashida, Yukimasa Yamada, Akira Sou, "Effect of Nozzle Inlet Roundness and Nozzle Length on Cavitation and Liquid Jet," *Proceedings of 13th International Conference on Liquid Atomization and Spray Systems (ICLASS 2015)*, 2015.

ABSTRACT

Internal combustion engines are subject to an increasingly tougher emission requirements in recent years. To comply with these stringent requirements, a precise control over the combustion process is needed, as the combustion process greatly affects the thermal efficiency and the resulting emission from the exhaust gas. In this regard, a design for fuel injector that can generate fuel sprays with desirable characteristics for combustion processes are continually developed. Cavitation phenomena in fuel injector nozzles are known to play a large role in determining the characteristics of the resulting fuel spray. Thus, a complete understanding of in-nozzle cavitation phenomena us required for the development of next-generation fuel injectors.

In this study, visualizations of in-nozzle cavitation were conducted using several visualization techniques, in order to clarify various aspects of cavitation development in the nozzle and how it affects the break-up of discharged liquid jet from the nozzle. Amongst the techniques used were shadowgraph, high-speed imaging, x-ray phase contrast imaging (XPCI), and tomographic stereoscopic particle image velocimetry (TSPIV). The visualizations were conducted using nozzles with both simplified and realistic geometries with various sizes.

XPCI of two-dimensional (2D) nozzles with various sizes and upstream geometry revealed that in-nozzle cavitation follows the similarity law, that is, the cavitation bubbles scales proportionally to the nozzle size. XPCI also reveals the non-spherical shapes of cavitation bubble, which is caused by the velocity profile of a cavitating nozzle. Additionally, it was found that jet break-up is suppressed as nozzle size gets smaller, as a result of the increasing surface tension effect on smaller nozzles. For symmetrical nozzle, jet deformation is reduced at hydraulic flip regimes, but keeps stable at mini-sac nozzle as a result of imperfect hydraulic flip (IHF), caused by the increased turbulence from the asymmetrical upstream inflow from the nozzle inlet.

High-speed imaging of 2D nozzle under steady and transient injection condition were carried out to examine the applicability of steady injection data of in-nozzle cavitation and discharged liquid jet to the transient injection processes. Furthermore, XPCI was carried out to investigate the morphology of cavitation development in the nozzle. The result confirms the applicability of data from steady injection conditions to transient injection processes. It was also revealed that cavitation inception process in the nozzle is caused by two kinds of heterogeneous nucleation. The first one results from an expansion of a microbubble that is trapped in the nozzle surface, while the second one results from the breakup of a bubble that enters from upstream of the nozzle and breaks up near velocity boundary layer.

High-speed imaging and TSPIV of an enlarged three-hole mini-sac fuel injector and its discharged liquid jet at two different needle lifts was carried out to investigate the effect of string cavitation and geometrical cavitation to the discharged liquid jet angle. It was revealed that at low needle lift, a vortex ring flow is formed in the sac, which induces helical flow in the nozzle. The radial gradient of the vertical velocity varies over time, and string cavitation occurs when a microbubble

travels to the core of the vortex at the exact time when the gradient is particularly large. In the case of high needle lift, the vortex ring flow is not formed and the flow field is relatively uniform. As a result, discharged liquid jet angle is mainly governed by string cavitation at low needle lift and geometrical cavitation at high needle lift.

The study concluded that visualization experiments conducted using several visualization techniques on nozzles with various sizes and geometries have resulted in a deeper understanding of cavitation phenomena in the nozzle. Bases on this understanding, a new design strategy of fuel injector, i.e. by controlling the vortex ring formation on the nozzle and taking into account the size similarity law and cavitation bubbles' non-sphericity for numerical simulation of in-nozzle cavitation, a better control over cavitation in fuel injectors can be obtained.

LIST OF TABLES

LIST OF FIGURES

ABBREVIATIONS

2D : Two-Dimensional
3D : Three-Dimensional
CCD : Charged-Coupled Device
CFD : Computational Fluid Dynamics
ECU : Engine Control Unit
EU : European Union
EV : Electric Vehicle
IHF : Imperfect Hydraulic Flip
IMO : International Maritime Organization
HC : Hydrocarbon
LDV : Laser Doppler Velocimetry
PIV : Particle Image Velocimetry
PM : Particulate Matters
PEEK : Polyether Ether Ketone
THF : Total Hydraulic Flip
SC : String Cavitation
TSPIV : Tomographic Stereoscopic PIV
VCO : Valve-Covered Orifice
WHO : World Health Organization
XPCI : X-ray Phase Contrast Imaging

NOMENCLATURE

D	Nozzle diameter [mm]
D_e	Equivalent bubble diameter [-]
DH	Hydraulic diameter of the nozzle[m]
V	Mean flow velocity in the nozzle [m/s]
L	Nozzle length [mm]
L_c	Cavitation length [mm]
L_{p1}	Pipe length between pressure vessel and solenoid valve [m]
L_{p2}	Pipe length between solenoid valve and nozzle [m]
P_i	Injection pressure [MPa]
P_v	Vapour saturation pressure [MPa]
P_t	Vessel pressure [MPa]
R	Curvature radius of the nozzle inlet [μm]
r	Radial distance in the sac [mm]
Re	Reynolds number [-]
T	Nozzle thickness [mm]
T_{cav}	Time needed until maximum radius of a cavitation nucleus is reached [μs]
T_F	Time needed for a separated boundary layer to be formed in the nozzle [μs]
T_Q	Time to reach peak flow rate in the nozzle [μs]
t_v	Virtual time history of TSPIV result [μs]
W	Nozzle width [mm]
W_c	Cavitation width [mm]
We	Weber number [-]
X_b	cavitation bubble horizontal chord length [mm]
Y_b	cavitation bubble vertical chord length [mm]
y	Vertical position measured from the nozzle outlet [mm]
Z	Needle seat gap [mm]
z	Horizontal plane of TSPIV measurement [mm]
γ	Surface tension [N/m]
θ	Liquid jet angle [degree]
λ	Perturbation length scale [-]
v	Kinematic viscosity [m^2/s]
$ø_1$	Diameter of the pipe between pressure vessel and solenoid valve [mm]
$ø_2$	Diameter of the pipe between solenoid valve and nozzle [mm]
ρ	Liquid density [kg/m^3]
τ	injection time scale [-]

1 INTRODUCTION

1.1 Background

With climate change continuing to be an important problem around the world, various means to reduce the effect of climate change are still ongoing up to the present day. In line with this problem, since the early nineties, numerous regulatory agencies and legislative organizations have begun to enforce a more stringent emission standard (in accordance with the target established at Kyoto Protocol) for hydrocarbon-burning engines. The combined efforts of these agencies have resulted in such regulations as IMO NOx regulations, European emission standard, and California Air Resources Board standard [1]. These regulations have been an effective first step in enforcing emission reduction worldwide.

Of course, a drastic cutback in emission cannot happen overnight. Air pollution continues to be a serious problem nowadays. A high concentration of particulate matters (PM), especially the deadly $PM_{2.5}$, can still easily be found all over the globe [2]. This poses a real concern from a global health perspective, as a study concluded that even the recommended WHO “safe” guidelines of 10 $\mu g/m^3$ [3] have been proven to increase the risk of lung cancer by 36% [4]. Worse still, in countries with emerging market economies like China and India, the average concentration can reach as high as 30-60 $\mu g/m^3$ [5], which is more than several times the value of the WHO standard.

Although the current state of global air pollution still leaves much to be desired, it is important to remember that emission regulations were designed with a long-term goal in mind. For example, the latest revision of European emission standard, Euro 6, was finalized in 2014 but it will not come into force until 2020 [6]. For the last two decades, such long grace period has traditionally provided enough time for engine makers and automotive producers alike to implement the regulations. However, difficulties began to emerge as the limit grew stringer. In a recent study, Annenberg et al. [7] have found that over half of new passenger cars in major automobile markets around the world do not conform to the obligatory emission requirements in their respective regions. Worse, a separate study by Fontaras et al. [8] found that vehicles that did pass the requirements in laboratory tests showed totally different road performance, with the difference ranges in the order of 30-40%. It was evident that automobile producers are having a hard time to keep up with the stringer emission standard.

Ultimately, the difficulties have led the automakers to cheat the testing processes, which caused a recent string of emission-related scandals globally [9]–[11]. The scandals have caused a severe backlash from governmental regulatory agencies to the automakers, with the strictest reactions came from the European Union (EU). Several cities in the EU zone have already implemented or announced their intention to ban the use of diesel and/or gasoline cars inside the

city limits. At the national levels, several countries such as the United Kingdoms and France have announced their plan to end the use of fossil fuel vehicles by 2040 [12].

As the rules grew stricter, consumers and automakers alike are scrambling to find an alternative solution. One answer lies in the adoption of alternative fuel vehicles. Both hydrogen-based fuel cells vehicles and electric vehicles (EV) are often championed as the most likely replacement for fossil fuel vehicles, although EV has seen a wider success compared to fuel cell vehicles. Since the emission scandals broke out, the EV adoption rate has grown by more than 56% [13]. As expected, countries with the highest growth are all located in the EU zone, with Norway, Iceland, and Sweden leading the new EV sales worldwide. Nonetheless, China leads in terms of raw number, with a market share of 39% of total EVs in the world [14].

With EV sales continues to increase every year, EV shows some promise as a replacement for fossil fuel vehicles. However, it is important to note that the growth in EV sales has mainly resulted from policy changes created as a response to the emission scandals [13]. Many technical challenges to a wider EV adoption remain, such as the relatively shorter cruising range of EV (compared to fossil fuel vehicles), limitations of battery technologies, scarcity of battery materials, and the lack of EV-supporting infrastructures [13], [15], [16]. Additionally, EVs are associated with higher financial costs, which is probably the most important factor for most consumers looking to buy a new vehicle [17]–[20]. Currently, most countries introduced various kinds of financial incentives to offset the higher financial costs of EV adoption. It is important to note that the incentives are only a temporary measure, and will disappear at some point. When they do, EV sales often dropped drastically. Tesla, one of the most famous EV manufacturer in the world, has demonstrated this twice. Once in 2017 when Hong Kong stopped EV-associated tax break [21] and once again recently, when several federal governments in the US cut the tax incentives for new EV purchase [22]. When the incentives in other countries eventually stop, it is questionable whether the current trend in EV sales can last long enough to replace fossil fuel vehicles.

In the end, the current policy of fossil fuel vehicle limitations and/or ban were mostly caused by reactionary changes. Such changes are not sustainable in the long run, especially when the total market share of EV is still very low (less than 2% globally) [13]. Some consultants have even suggested that automakers are overestimating the demand of EV [23]. Considering that it might take 10 to 80 years for the world to complete the transition to alternative energy sources [24], it might be unrealistic to decide that the sole answer to climate change from transportation perspectives is to rely on EV. Besides continuing the development of EV, Automakers should still consider “traditional” approaches of increasing thermal performance and reducing exhaust gas emissions of fossil fuel vehicles.

1.2 Fuel Injectors

The thermal performance and exhaust gas emission of internal combustion engines are mostly affected by the combustion processes of the engines itself. As such, most of the approaches to

increase the thermal efficiency of internal combustion engines are usually focused on increasing combustion efficiency. This usually involves the installation of additional equipment, such as exhaust gas heat recovery system or using a turbocharger to increase the amount of air in the combustion chamber so fuel can be burned cleanly. In the latter's case, thermal efficiency is increased by achieving better mixture formation between fuel and air. However, better mixture formation can be achieved without introducing additional components to the engine. This can be done by which is by increasing the atomization quality of the fuel injection system through better fuel injector design. Theoretically speaking, a perfect mixture can be achieved if the fuel injection system of an engine performs flawlessly.

As the name suggests, a fuel injection system in an internal combustion engine serves to deliver fuel to the combustion chamber. Since modern engines operate at a variable power output, the fuel injection system should also be able to deliver a precise amount of fuel at varying degree. In addition, as the combustion should happen at the exact timing the piston reaches the combustion chamber, precise timing of fuel delivery is also needed. In short, the fuel injection system works by delivering a precise amount of fuel to the combustion chamber at a precise time, so that the engine can deliver the required power output.

Of course, proper delivery timing and amount of fuel alone does not decide the result of combustion. Sufficient amount of oxygen is also needed so that the fuel can burn properly. Just like the fuel, delivery of air to the combustion chamber must be managed precisely to achieve good combustion characteristics. The proper mix between fuel and oxygen is needed so the fuel can burn cleanly, as determined by the ideal (stoichiometric) air-to-fuel ratio. Too much fuel and some leftover droplet might remain by the end of injection, which can cause soot buildup and increase the formation of particulate matters. Conversely, too much air will reduce the thermal efficiency of the combustion, which reduces overall engine performance. In reality, a little amount of excess air is always present in the combustion chamber, in order to prevent incomplete combustion. An ideal stoichiometric ratio between air and fuel is hard to achieve because the different densities between fuel and air made them hard to mix completely. Because of this, atomization properties of the fuel should also be considered when designing a fuel injection system.

A typical automobile engine can operate in the range of up from 800 RPM (idling) to 10,000 RPM (cruising). To accommodate the fast revolution speed, the combustion process needs to happen instantly, in a very short time span. With the exception of gas turbines, all internal combustion engines use liquid fuel as their fuel sources. Attempting to burn liquid fuel as-is in the combustion chamber would only lead to a slow and localized burning process, with much fuel left unburned after the combustion is done. Hence why atomization process is crucial for internal combustion engines. Atomization is essentially a process where bulk liquid is converted into sprays, which consists of small drops. By atomizing the fuel, specific surface area of the fuel increases, which means it can burn more easily and completely. This is not to mention the additional benefits, such as better mixing

between the fuel and oxygen, higher volumetric heat release rate, and reduced pollutant in the exhaust emission [25].

Atomization of any kind of liquid can be achieved in various kinds of ways, although the basic processes always involve subjecting the liquid to high relative velocity with the surrounding gas. By doing so, a highly turbulent condition is created, which will promote the growth of disturbance in the liquid. Eventually, the disturbance will lead to disintegration of the liquid, in the form of ligaments and droplets. At this stage, the liquid has the same bulk mass before it was atomized, but the total surface area massively increases.

Atomization of fuel in internal combustion engines is commonly carried out with plain-orifice type atomizer. In this kind of atomizer, the fuel is passed through a small circular passage which is called a nozzle. Should the injected liquid's pressure is high enough to exceed the ambient gas pressure, a high-velocity liquid jet is formed, which then rapidly disintegrates to atomized spray [25]. As the air inside the combustion chamber normally has a high pressure due to piston compression, spray formation is only achievable under very high injection pressure. Figure 1 shows a cutout image of a fuel injector and the enlarged view of the nozzle. The injection is carried out with pulsed timing, by way of a needle valve in the injector. The timing of closing and opening in the valve is controlled with an engine control unit (ECU) for modern engines.

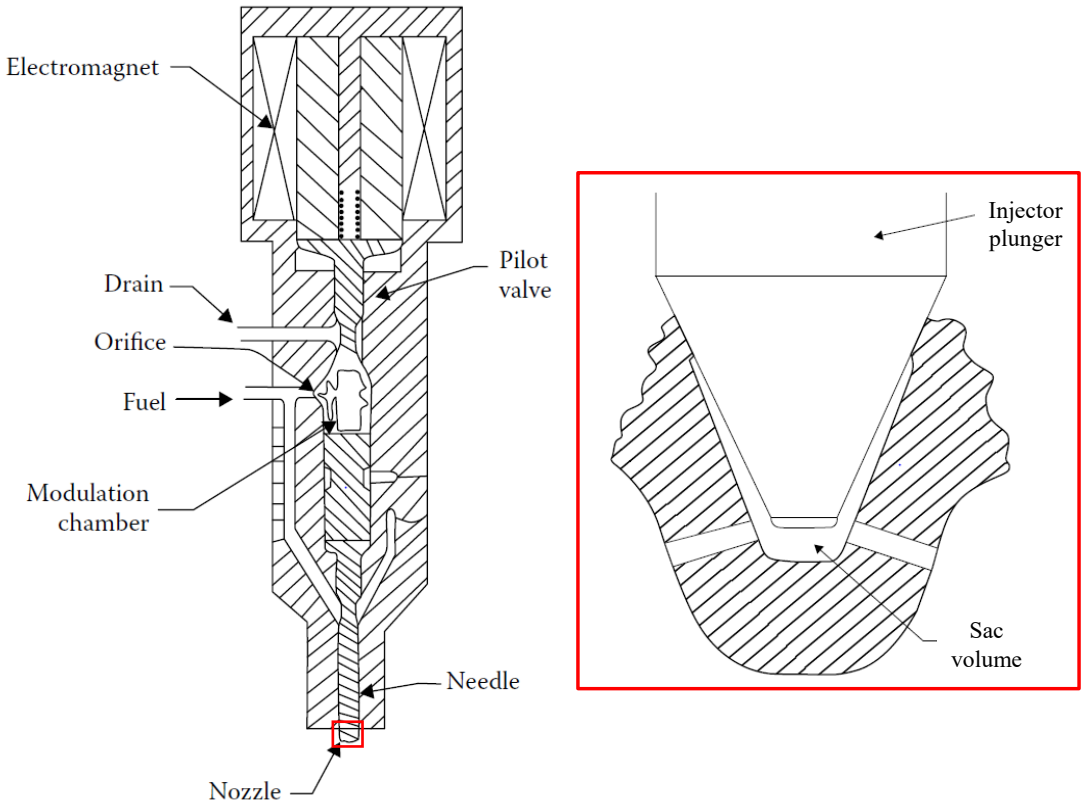

Figure 1 Profile image of a fuel injector and enlarged view of the nozzle [25]

Figure 2 shows an illustration of a combustion chamber in a direct-injection diesel engine. Modern internal combustion engines rely on internal mixture formation of fuel and air in the combustion chamber, be it gasoline or diesel engines. Controlling the fuel-air mixture in the

combustion chamber is crucial to achieve good, clean combustion, especially for diesel engine, where combustion occurs without the help of spark plug (auto-ignition combustion). To achieve a suitable mixture between fuel and air, the fuel spray has to possess several desired characteristics. These characteristics include spray penetration, angle, and mean droplet size in the spray. The characteristics are affected by several factors, with the most important being, the physical properties of the fuel (surface tension and viscosity) and the internal flow of fuel inside the injector. The internal flow itself is highly affected by the injector geometry. Because of this, injector geometry is one of the most critical factors that determine the fuel's atomization quality. Good atomization will result in good combustion with fewer particulate leftovers from unburned fuel. Consequently, injector geometry directly affects exhaust gas emission, as illustrated in Figure 3. An optimal injector design can help to improve these factors without inflicting any major changes to the existing engine design.

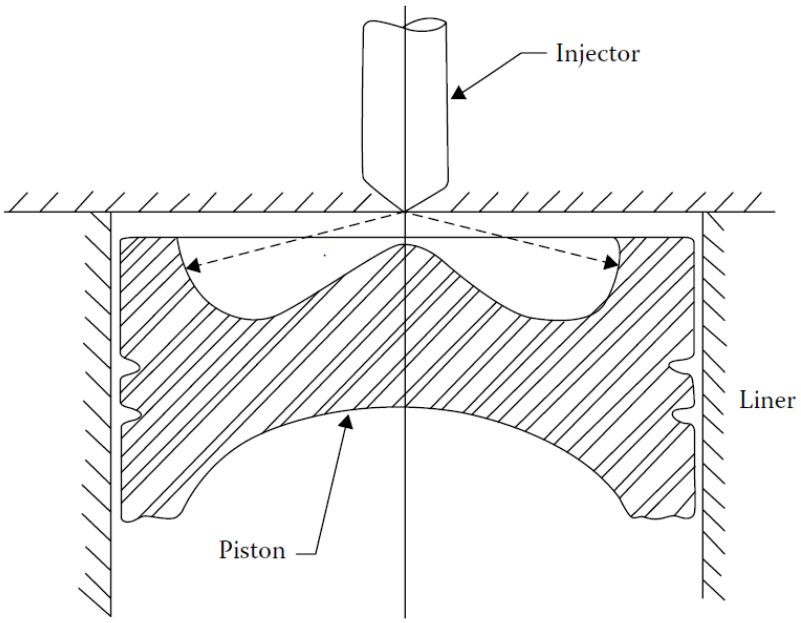

Figure 2 Typical profile of a combustion chamber in a direct-injection diesel engine [25]

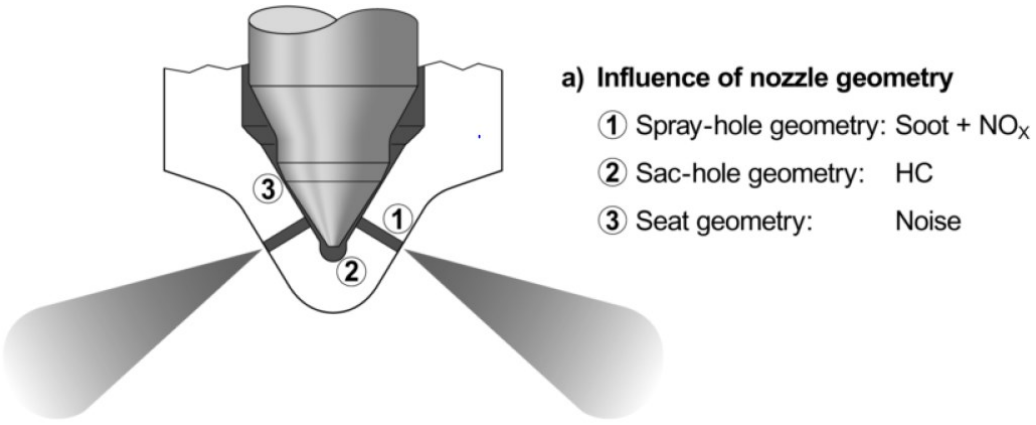

Figure 3 Illustration of the effect of nozzle design on exhaust gas emission [26]

Various studies over the year have been dedicated to investigating the effects of injector geometry on spray characteristics. As a result of the complicated shapes of modern fuel injectors, which often comprised of multi-hole injectors with various nozzle and sac configurations, these studies are not only limited to the geometries of the nozzle but also includes the geometries of the sac hole and the needle [26]. However, the bulk of the attention is paid to the factors that influence the internal flow of the nozzle, such as hole-to-hole interactions [27], nozzle shapes [7], nozzle size [28]–[30], and nozzle geometries [31]–[34]. This is to be expected, considering that internal flow in the nozzle might be the single biggest factor affecting the primary atomization characteristics of the spray [35].

1.3 Cavitation in Fuel Injector

The word “cavitation” was first suggested by R.E. Froude to Barnaby and Thornycroft, who were the first two people who discovered and investigated the formation of vapor bubbles on HMS Daring’s propeller blades [36]. Cavitation can be defined as a phenomenon where a sudden pressure drop caused bubble nuclei in a liquid to expand, which results in a rapid vapor formation in the liquid body. In regards to the result, i.e. the formation of vapor bubbles, this phenomenon is very similar to the boiling process. The one main difference between cavitation and boiling is the thermodynamic process path that leads to vapor formation. Cavitation occurs when local pressure in a liquid pressure drops below the vapor pressure, while boiling occurs when the bulk liquid temperature rises above the saturated vapor/liquid temperature [37]. The pressure drop can be caused by either fast-flowing liquid (hydrodynamic cavitation) or high-intensity sound wave (acoustic cavitation) [38]. Note that rapid void formation caused by a sudden local deposition of energy is also called ‘cavitation,’ which are the case for optic cavitation and particle cavitation [39]. For the sake of brevity, all terms of ‘cavitation’ in the current work is used to refer to hydrodynamic cavitation hereafter.

First studies of cavitation were conducted experimentally [40]. Following these experimental studies, Lord Rayleigh [41] laid the first theoretical foundation for the formation and collapse of a spherical bubble in a stationary liquid. Plesset [42] expanded on this work by conducting additional numerical and experimental studies. Plesset’s study was the first to classify cavitation in flowing liquid into three different regimes, which are non-cavitating flow, cavitating flow with a small number of bubbles, and cavitating flow with a single large cavity (Figure 4). In addition, Plesset also applied Rayleigh’s equation on a flowing liquid while taking the effect of surface tension into account, which resulted in the Rayleigh-Plesset equation. Although this equation is only valid for spherical bubbles, it is still widely employed for numerical studies of cavitation nowadays. Additional aspects of cavitation studies are discussed in detail by Brennen [37], which includes the discussion of bubble nucleation, bubble dynamics and collapse, as well as various types of cavitating flows.

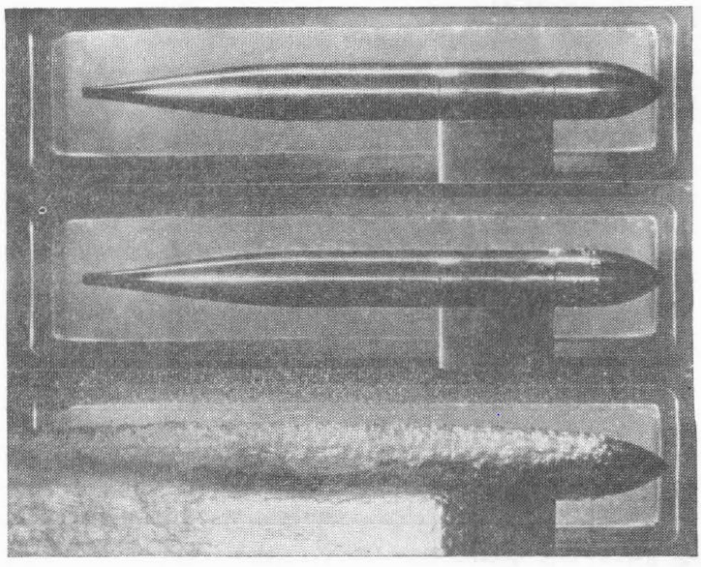

Figure 4 Three regimes of cavitating flow; top: non-cavitating flow, middle: cavitating flow with a small number of bubbles, down: cavitating flow with a single large cavity [42]

In the field of engineering, cavitation is often discussed from the viewpoint of its drawback. Specifically, the material damages it can cause to solid surfaces. When a cavitation bubble collapses, it produces either a shockwave (Figure 5) or a microjet (Figure 6). When it hits a solid surface near the point of collapse, the solid surface is exposed to a highly localized stress, which damages the surface. The damage is especially apparent when the bubble is located at less than twice its maximum radius from the solid surface [43]. Given repeated loading from numerous bubble collapses, fatigue failure that leads to material flaking in the surface can occur. This is the main mechanism of cavitation damage [37]. As the flaking also caused a small cluster of pits in the material, for metallic materials, erosion can further heighten the extent of damage caused by cavitation.

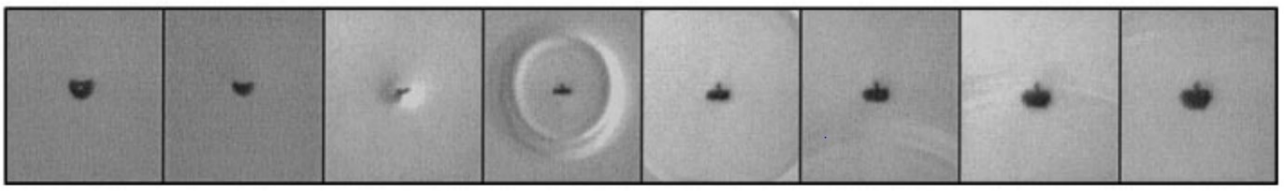

Figure 5 Shockwave produced by a single cavitation bubble collapse [43]

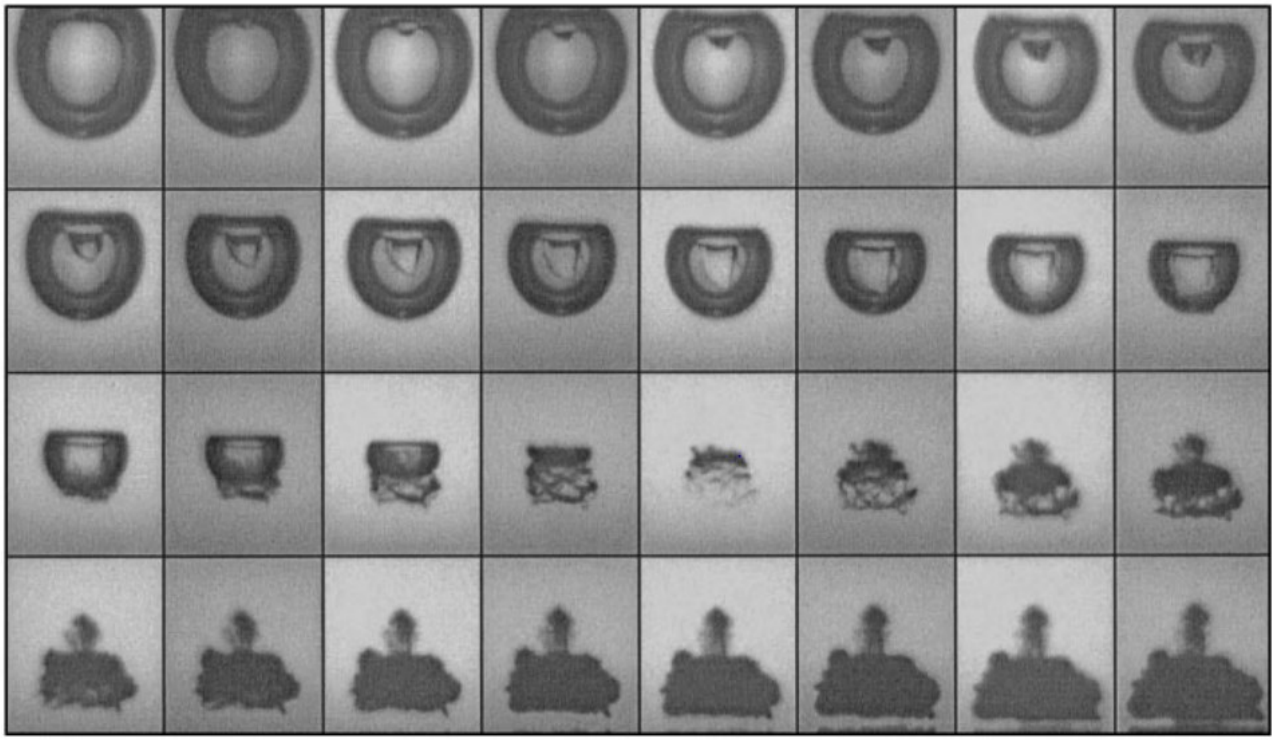

Figure 6 Microjet produced by a single cavitation bubble collapse [43]

As with other systems that involve high-pressure non-compressible liquid, fuel injectors are also subject to cavitation. In a closed space such a fuel injector, cavitation can occur when a moving liquid is accelerated, which causes an increase in dynamic pressure and a decrease in static pressure. The faster the liquid moves, the more likely it is for cavitation to occur. In addition to the high operating pressure, which results in a high liquid velocity in the system, fuel injector has numerous contractions where high pressure drop are prone to occur, which also increases the probability of cavitation occurrences. This can be seen in Figure 7, which shows the example of cavitation damage in multiple places inside fuel injector. Although any kind of damage is detrimental to the operation of the fuel injector, the most important is arguably the damages caused by cavitation on the nozzle and/or the sac, which can be seen in Figure 8. Given its location on the very tip of the injector, any disturbance to the flow, which is likely to occur when the sac and/or nozzle surface is altered as a result of the damages, can affect the characteristics of the spray's primary break-up. Additionally, even when cavitation damage has not occurred yet (e.g. in new fuel injectors), the disturbance in the flow caused by cavitation is equally likely to alter the flow characteristics, which also affects the resulting spray. The effects of cavitation are not always detrimental to atomization characteristics. The disturbance caused by the collapse of cavitation bubbles can induce high-intensity turbulence in the flow, and when it occurs near nozzle exit, the resulting spray have a larger angle. The mechanism of spray angle enhancement by the cavitation process is shown in Figure 9.

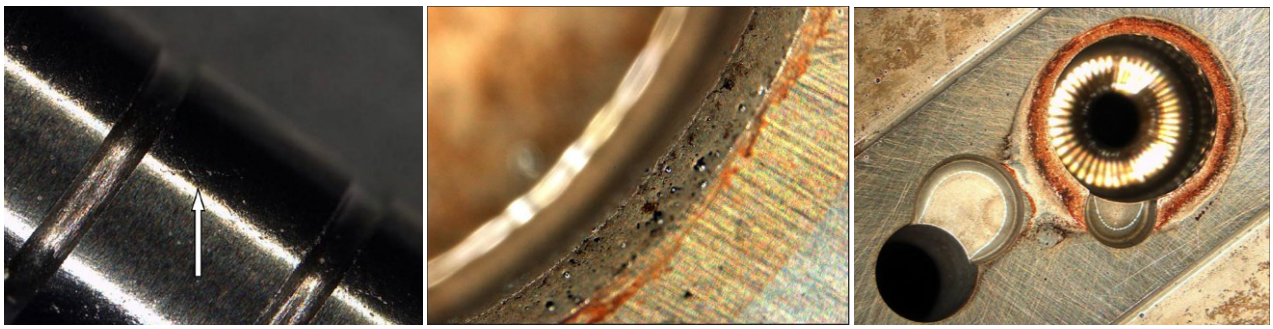

(a) Cavitation pitting in piezoelectric injector needle

(b) Cavitation erosion in piezoelectric injector overflow valve

(c) Cavitation erosion in solenoid injector overflow valve

Figure 7 Example of cavitation damages in multiple places inside fuel injector [44]

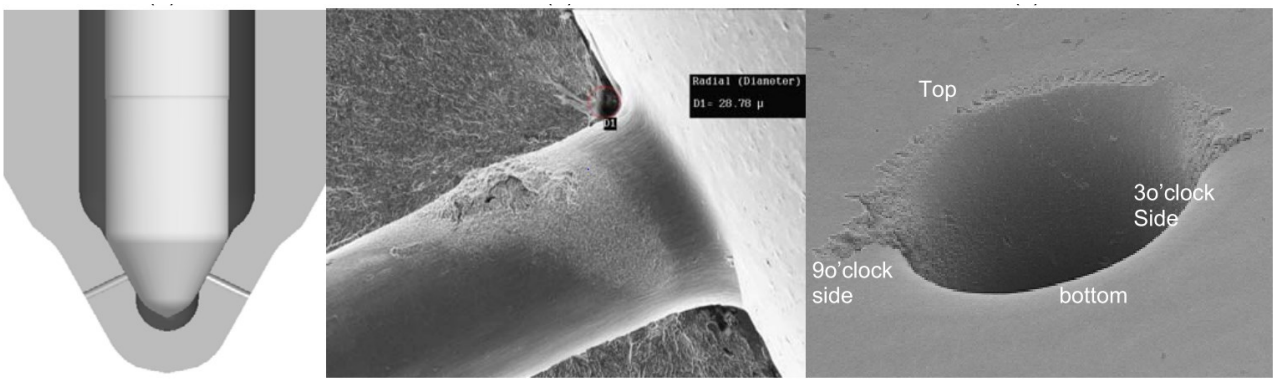

Figure 8 Damages caused by cavitation erosion in the nozzle [45]

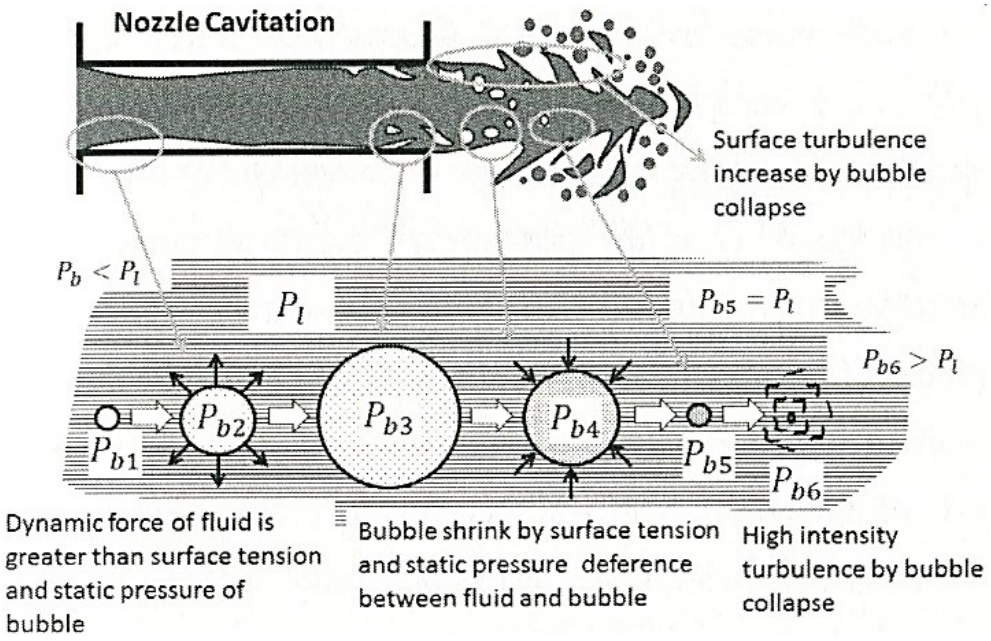

Figure 9 Mechanism of spray angle enhancement by cavitation process [46]

Cavitation in fuel injectors are typically categorized into two broad categories. The first one is the geometrical or hole cavitation. As the name indicates, this type of cavitation is commonly found on the nozzle hole, where sudden flow contraction and flow separation occurs. Instances of geometrical cavitation can also be found in locations where there are flow contractions, such as the

needle valve seat during the valve opening process [47]. The contraction causes flow separation to occur, which leads to a massive decrease in the fluid's static pressure in the recirculation flow area. Cavitation occurs as a result of the high pressure drop. Geometrical cavitation can take place as either a bubbly flow or a large, contiguous vapor film, as shown in Figure 10. The second type of cavitation is vortical cavitation. This kind of cavitation is commonly found in region with concentrated vorticity, such as the end tail of a propeller. Figure 11 shows an example of a vortical cavitation from the tip of a propeller blade. In fuel injectors, high vorticity can be found in the sac area, which occurs as a result of hole-to-hole interaction in multi-hole injectors [47], [48], as well as the eccentricity and low lift of the needle valve [49]–[56]. High pressure drop occurs in the core of a vortex. When a bubble nucleus enters the vortex core, it will begin to expand and elongates into a string-like cavity, as can be seen in Figure 12. Because of its string-like appearance, vortex cavitation is also commonly known as "string cavitation" in studies of fuel injector. Both geometrical and string cavitation affects the internal flow in the nozzle and the resulting spray in different ways. This will be explored in more detail in a later chapter.

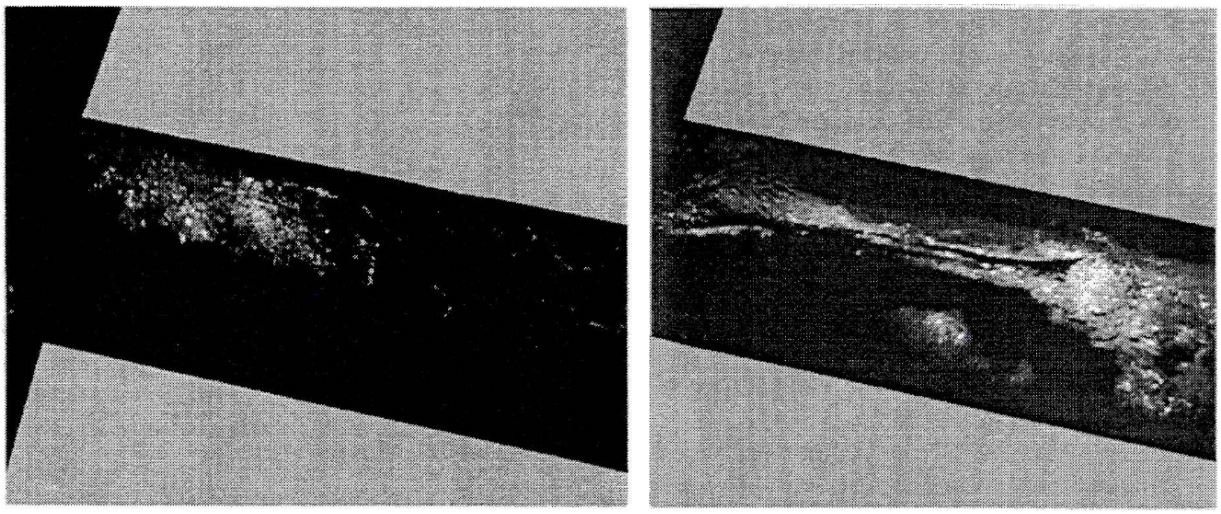

(a) Bubbly (incipient) cavitating flow (b) Cavitation film

Figure 10 Geometrical cavitation in the nozzle [57]

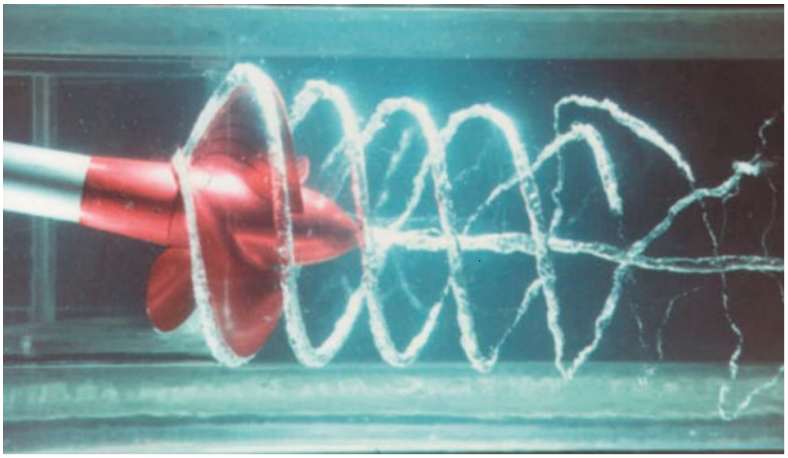

Figure 11 Vortical cavitation from the tip of propeller [58]

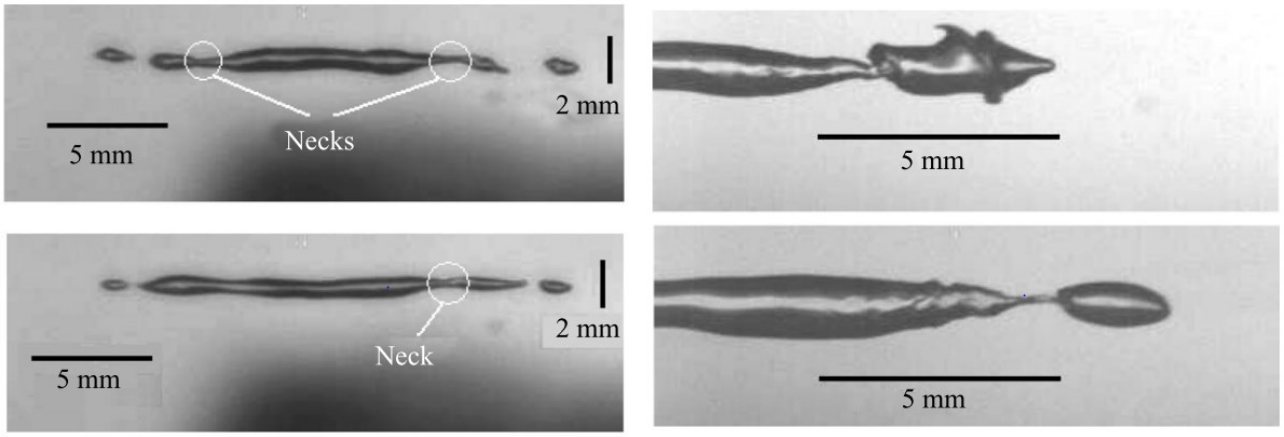

Figure 12 Growth and collapse of a vortical cavitation bubble [59]

Cavitation in fuel injector nozzles greatly affects the internal flow in both positive and negative ways. As discussed previously, various studies over the year have been dedicated to studying the internal flow of the nozzle. Because of its complexity, these internal flow studies are often dedicated solely to study in-nozzle cavitation. Various approaches used in these studies will be discussed next.

1.4 Numerical Simulation of In-nozzle Cavitation

Experimental studies often conducted for measurements of liquid spray and jet. Optical measurements liquid spray and jet are very common and has been carried out with various imaging techniques [60]. However, applying these techniques for internal flow in the nozzle is considerably more difficult. For example, the small size of the nozzle necessitates the use of optical equipment with higher capabilities than what is needed to take the images of spray. Oftentimes, measurement is only conducted on the spray, while the internal flow of the nozzle is estimated using discharge coefficient and non-dimensionless cavitation number [61], [62]. For this reason, internal flow of the nozzle is often investigated with Computational Fluid Dynamics (CFD). Besides overcoming the physical limitation of experimental approaches, CFD has an added benefit of giving the information that cannot be obtained experimentally, such as overall prediction of the flow field under various conditions (as opposed to specific conditions only, as often the case with experimental studies). Of course, it is important to note that cavitation is a complex phenomenon that is difficult to be properly modeled. This subchapter will discuss several numerical approaches that are commonly used in the study of in-nozzle cavitation.

Early instances of cavitation models were developed in the field of physics for open channel flow [63], [64]. For fuel injectors, one of the earliest models was developed by Schmidt, who simulated cavitation in simple single-hole nozzles with various inlet corner radius, length, and sac corner angle [65], [66]. The model used by Schmidt is a single-fluid model, which is also known as homogeneous Eulerian model. In this model, liquid and vapor phases are uniformly distributed in each cell without slip condition, and the effects of surface tension are neglected. Schmidt also gives some prediction of how these geometrical parameters influence the exit momentum and coefficient of discharge of the jet. Although the result was rudimentary, it provided some important insight into

how geometrical changes affect the internal cavitating flow in the nozzle, as well as its impact on the liquid jet.

Later works on nozzle cavitation CFD were carried with a more realistic nozzle geometry using two-fluid models. Two-fluid models can be further divided into Eulerian-Eulerian and Eulerian-Lagrangian in accordance with how the mass transfer between liquid and vapor phases is tracked. For in-nozzle cavitation, Eulerian-Lagrangian approach is commonly used. In this approach, the fluid is considered as a continuous phase in the Eulerian frame of reference, while vapor bubbles are considered as Lagrangian elements. Rayleigh-Plesset equation is used to monitor the growth and collapse of the bubbles. Examples of this approach can be found in the works by Payri [67] and Giannadakis [68], who modeled cavitation in multi-hole injectors with realistic geometry using Reynolds-Averaged Navier-Stokes (RANS) equations. Additionally, several studies underscored the importance of vortical structures in the nozzle and conducted Large-Eddy Simulation (LES) to simulate turbulent cavitating flow in the nozzle [69]–[71].

It should be noted that several of the studies mentioned previously were only focused on internal cavitating flow in the nozzle, and did not discuss how it affects jet breakup after it is discharged from the nozzle. Although various cavitation models developed over the years can predict internal flow in the nozzle with reasonable accuracy, correctly predicting the effect of cavitation on jet break-up is harder. Because of this, numerical simulations of internal flow are often conducted in tandem with optical measurements of the spray, to help to validate the result of the simulations. Examples of this approach can be seen in these studies [72]–[75].

1.5 Visualization of In-nozzle Cavitation

Even with all the developments in cavitation CFD, flow visualization conducted with transparent model nozzle is still widely utilized for in-nozzle cavitation study. This is because flow visualization enables direct correlation between internal flow parameters and the characteristics of the liquid jet break-up. Of course, there are various difficulties associated with internal flow visualization. These difficulties often necessitate some simplification for the setup used in internal flow visualization. This subchapter will explore some simplifications that are commonly used for visualization of in-nozzle cavitation, as well as recent developments of visualization techniques for internal flow.

1.5.1 Size aspects

As briefly discussed in the previous subchapter, high-capability optical setup is needed for visualization of internal flow in the nozzle. As cavitation is an inherently transient phenomenon, time-series images are needed to fully capture cavitation development in the nozzle. Modern fuel injector nozzles have a very small size, with a diameter in the range of ~100 μm. Together with the high operating pressure of fuel injector, this means that cavitation in the nozzle develops in a very short time, in the order of μm/ μs. Because of this, a high speed camera with sufficient magnification is needed to take cavitation images with sufficient temporal and spatial resolution. Furthermore, as sufficient light has to enter the camera’s sensor in such small time and space, a light source with

high intensity is often needed. Put together, this means that simply taking images of cavitation development in the nozzle requires the use of high-speed camera equipped with sufficient objective lens and high-intensity light source.

In addition to the complicated optical setup, another problem can result from the small size of the nozzles. It is hard to control for surface imperfections that may occur during the manufacturing process of small nozzles. As the imperfection is likely to influence the internal flow [76], results from experiments carried out with nozzles that were not controlled for surface imperfection may be flawed.

With such complications resulting from the small size of the nozzles, it is not surprising that the most common simplifications carried out for internal flow visualization were the utilization of enlarged nozzles. Although the flow field of small and enlarged nozzle might be different, this approach can help to visualize cavitation development in the nozzle and its effect on jet break-up with satisfactory temporal and spatial resolution. In fact, the first visualization of internal cavitating flow by Bergwerk [77] was conducted with several enlarged, transparent model of single-hole diesel injector nozzles. Water and Shell fusus oil were used as the working liquid in Bergwerk's experiment. The experiment resulted in the first images of cavitation and its effect on the liquid jet break-up, as can be seen in Figure 13. Bergwerk was also the first to identify the cavitation regime known as "hydraulic flip," where the vapor region in the nozzle has expanded until it reaches past the nozzle exit. At this regime, the surrounding gas enters the nozzle, which prevented the reattachment of separated flow to the wall and suppresses liquid jet break-up.

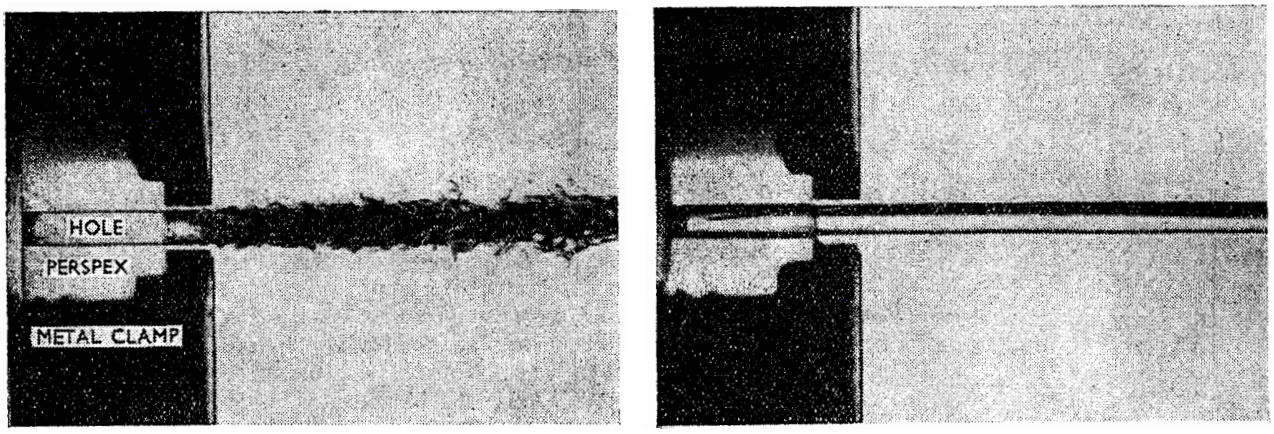

Figure 13 First images of nozzles' internal flow and liquid jet under cavitating (left) and hydraulic flip condition. Nozzle diameter was 10 mm and Shell fusus oil was used as the working liquid [77]

Although Bergwerk's study was the first to visualize in-nozzle cavitation and its effect liquid jet break up, the study did not give detailed analysis on the development of internal cavitating flow or the mechanism of liquid jet break-up enhancement by cavitation. Bergwerk's work would be expanded later by Nurick [78], who conducted experiments with enlarged nozzles with cylindrical and rectangular geometries. Nurick provided some explanation on the condition of cavitation inception and cavitation effect on the discharged jet. The mechanism of liquid jet break-up enhancement by cavitation is provided by Hiroyasu et al. [79], [80]. Hiroyasu et al. showed that flow

reattachment occurs when there is cavitation in the nozzle. At the tail end of the cavitation where the separated flow reattaches to the wall, intense turbulence is generated. This turbulence increases surface disturbance, which helps to decrease the break-up length of the liquid jet. The disturbance is especially strong when cavitation has sufficiently developed until it nearly reaches the nozzle exit, otherwise known as the supercavitation regime [81]. This mechanism is illustrated in Figure 14.

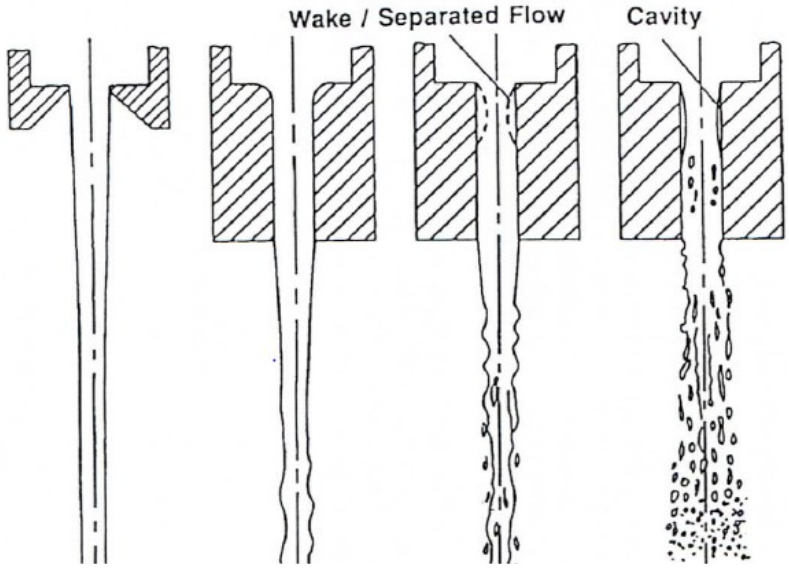

Figure 14 Liquid jet break-up enhancement on cavitation occurrence [80]

The early studies have given some valuable insights on the development of cavitation in the nozzles and how it affects liquid jet break-up. Following these studies, additional studies of internal cavitating flow that were conducted with enlarged nozzles followed. These subsequent studies were focused on various specific factors that influence cavitation development. For example, Soteriou et al. [82] showed that asymmetric inflow in sac-type nozzles, which includes mini-sac and Valve-Covered Orifice (VCO) nozzles, can result in a different kind of hydraulic flip from the one identified by Bergwerk. For nozzles with asymmetric inflow, it is possible for flow reattachment to still occur periodically even after hydraulic flip regime has been reached in the nozzle. Soteriou et al. named this type of hydraulic flip as Imperfect Hydraulic Flip (IHF) to distinguish it from Total Hydraulic Flip (THF) discovered by Bergwerk. Arcoumanis et al. [57] and Roth et al. [83] showed that cross flow resulting from the hole-to-hole interaction in multi-hole nozzles creates a strong vortex in the sac, which may result in the formation of string cavitation (Figure 15). Additional studies showed that besides hole-to-hole interaction, eccentric sac configuration can also result in strong vortex, which may enable the formation of string cavitation in single-hole nozzles [47], [50]. Studies carried out with biodiesel [84], [85] and variable fuel temperature [86] also showed how the difference in liquid's physical properties (density, viscosity, surface tension, and vapor pressure) affects cavitation development in the nozzle.

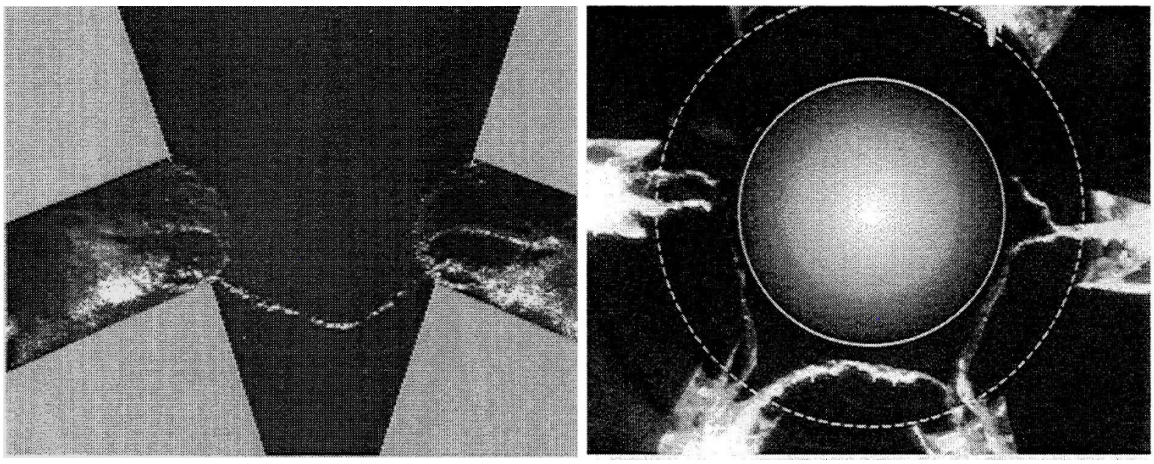

Figure 15 Side and bottom view of string cavitation in nozzle sac [57]

Although enlarged nozzles have been successfully utilized to study internal cavitating flow, the difference in scale of the nozzles used in the studies and nozzles of real fuel injectors were still of concern for many researchers. Because of this, some studies were conducted with real-scale nozzles [49], [87], [88], in spite of the difficulties associated with the visualization of real-scale nozzles. These early visualization studies often resulted in images with resolution that are too poor to be used in quantitative measurement, as can be seen in Figure 16. Which is why some of the studies are sometimes supplanted with numerical simulation results [88] to help explain the development of cavitation and jet break-up. However, imaging technology has advanced far since the time of early cavitation visualization studies. Nowadays, visualization studies conducted with real-scale nozzles conducted produced clear images of cavitation and jet break-up with high temporal resolution [52], [54], [89], [90], as shown in Figure 17. This raised some questions regarding the applicability of results from enlarged nozzle studies to the practical operating condition of fuel injectors, although studies have confirmed the similarity between flow in enlarged and real-scale nozzles [28], [30], [91].

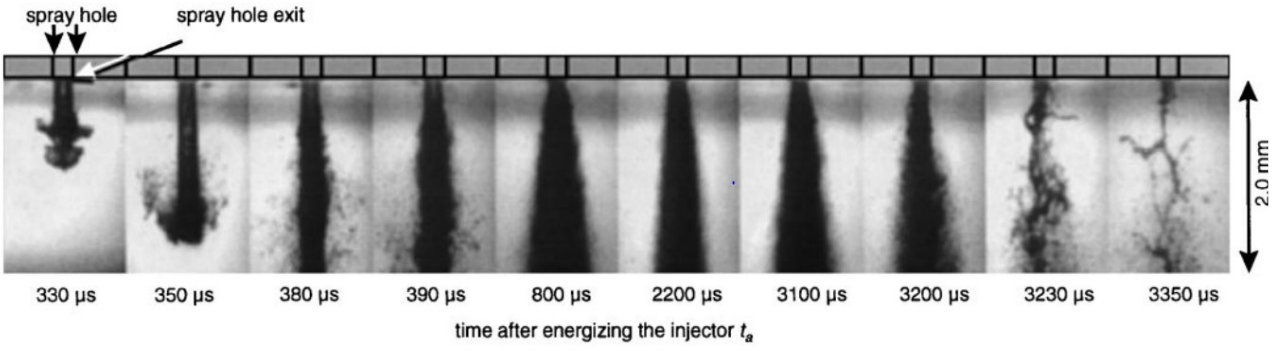

Figure 16 Shadowgraph of a discharged jet from a nozzle with D = 0.2 mm and L = 1.0 mm. Rail pressure is 25 MPa, with 1.5 MPa back pressure [87]

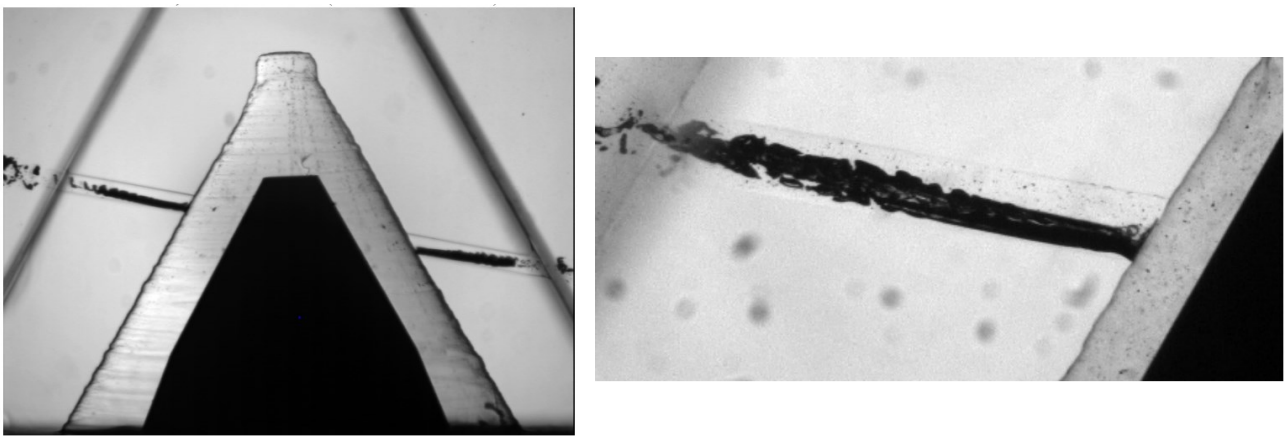

Figure 17 Shadowgraph of a real-scale VCO injector (Nozzle diameter = 150 μm) [89]

1.5.2 Geometrical aspects

Complicated geometry of fuel injector nozzles can make it difficult to single out individual effects of the nozzles' various geometrical parameters, such as nozzle length, width, inlet roundness, angle, and sac shape. Furthermore, these parameters are sometimes interdependent with each other [35], which further complicates the analysis of individual parameters' effects. This is the reason many studies were carried out with symmetrical single hole-nozzle [7], [52], [88], [92]–[95]. Although the geometry is not representative of real fuel injector nozzles, utilization of single-hole nozzle helped to control the effects of individual geometrical parameters of the nozzle, which is very useful for fundamental study of in-nozzle cavitation.

Although the utilization symmetrical single-hole nozzles enabled the investigation of individual geometrical parameters, a clear profile of cavitation cannot be obtained by observing cavitation in cylindrical nozzles. When in-nozzle cavitation has undergone the transition from bubbly flow to film formation, the internal flow of the nozzle is obscured by vapor region developing along the nozzle wall. Hence, some studies further simplified the nozzles used for visualization, by using so-called two-dimensional (2D) nozzles [96]–[102]. These nozzles were essentially rectangular shaped plain-orifice nozzles, whose ratio of thickness/width were often kept very low ($T/W \leq 1/4$). Although the structures of rectangular nozzles are even more different than common fuel injector nozzles, it has the advantage of keeping cavitation from obstructing the front wall of the nozzle. This enables the visualization of clear cavitation structure. In addition, as the internal flow is not obscured by cavitation, quantitative measurement of flow can also be carried out for developed cavitation regimes. Examples of Laser Doppler Velocimetry (LDV) measurements of 2D nozzles' internal flow [97] can be seen in Figure 18. Detailed velocity profile of the nozzle can be obtained even for supercavitation regime.

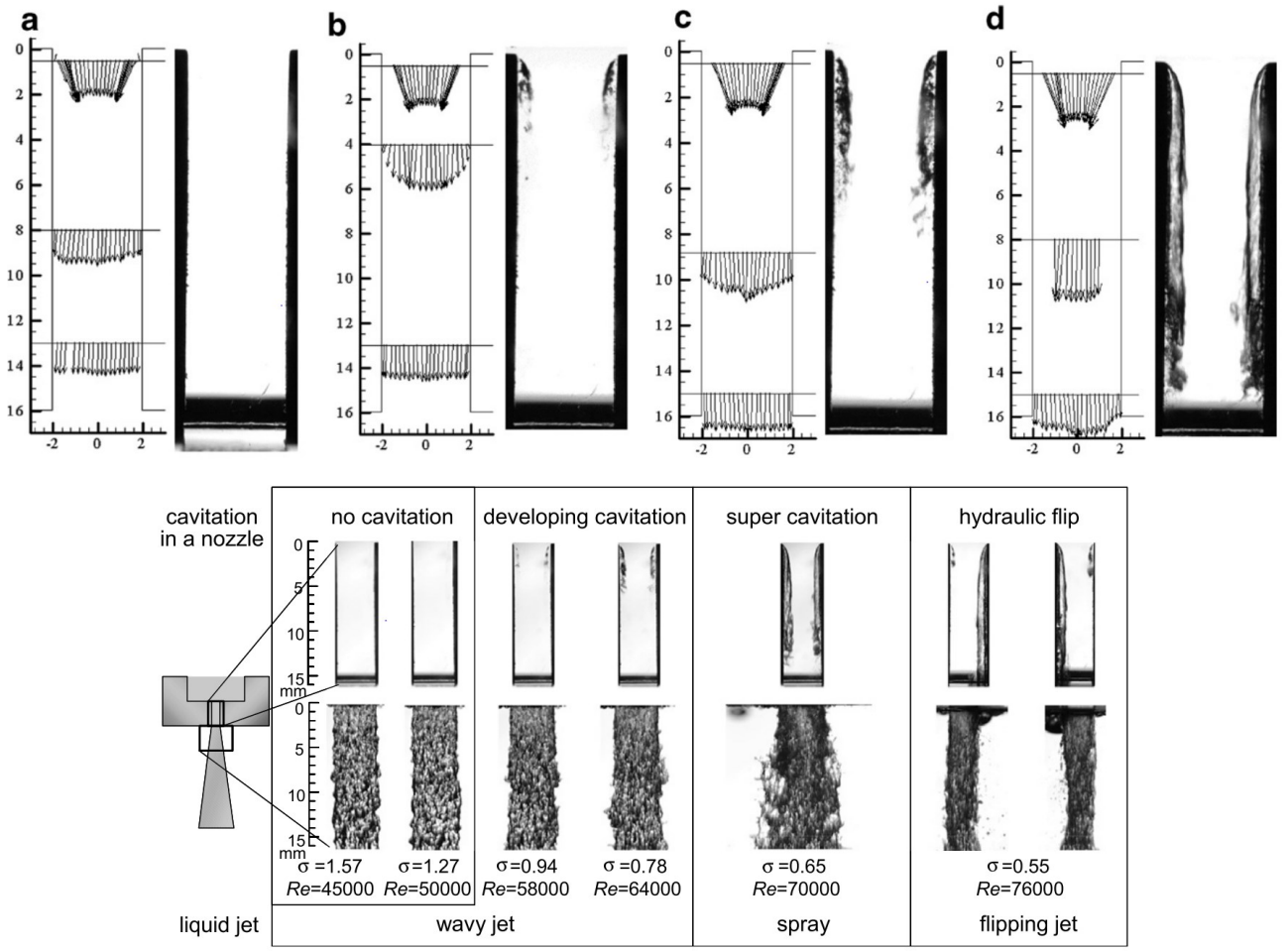

Figure 18 LDV measurements of internal flow and visualizations of discharged liquid jet under different cavitation regimes in 2D nozzles [97]

Despite its advantages, some phenomenon such as string cavitation simply cannot be recreated in 2D nozzles. For this reason, visualization of internal flow in nozzles with more complicated/realistic geometries remains important. Examples of such visualizations can be seen in the studies by Reid et al., [103]–[105], who showed how the flow between nozzle holes in multi-hole nozzles affected the vorticity and string cavitation formation in the nozzle upstream. Another work by Pratama and Sou [50] showed that string cavitation can even occur in single-hole nozzles, given an eccentric sac configuration with low enough lift. Examples of string cavitation formation in single-hole nozzles are shown in Figure 19.

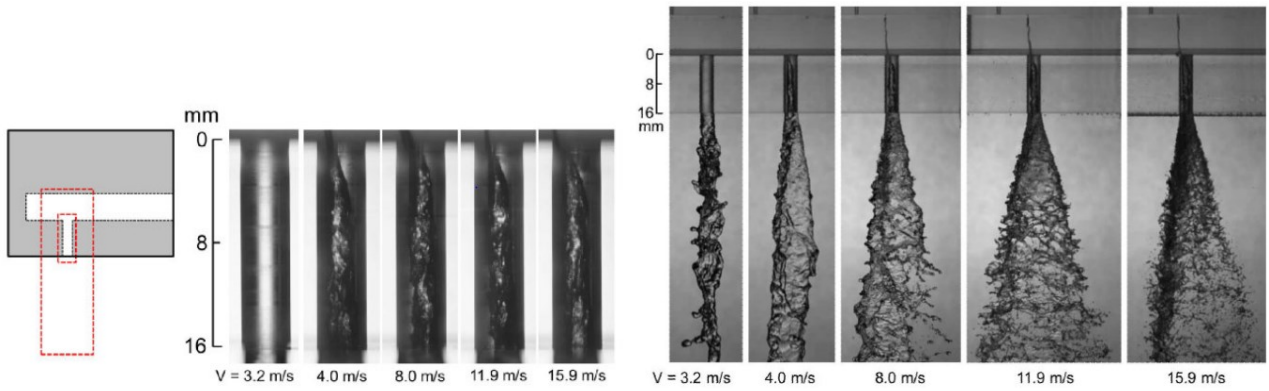

Figure 19 String cavitation in a single-hole injector with eccentric sac configuration [50]

From an engineering standpoint, it is important to have flow measurement data with geometry that is as close as possible to real injectors. Examples of such measurements can be seen in the studies by Arcoumanis et al., [57], [83], [106], who conducted LDV measurements on an enlarged multi-hole VCO nozzles to obtain some important data of geometrical parameters effects on velocity profile in the nozzle. Another examples can be found in the works by Hayashi et al., [53], [90], [107], who carried out a 2D Particle Image Velocimetry (PIV) on transparent mini-sac and VCO nozzles with realistic geometry. Example of the result is shown in Figure 20. The result helps to clarify the flow field in the nozzle when string cavitation occurs, especially at low needle lift. The studies help to clarify the effects of string cavitation in the nozzle on liquid jet break-up, although detailed explanation on its mechanism were not clarified yet.

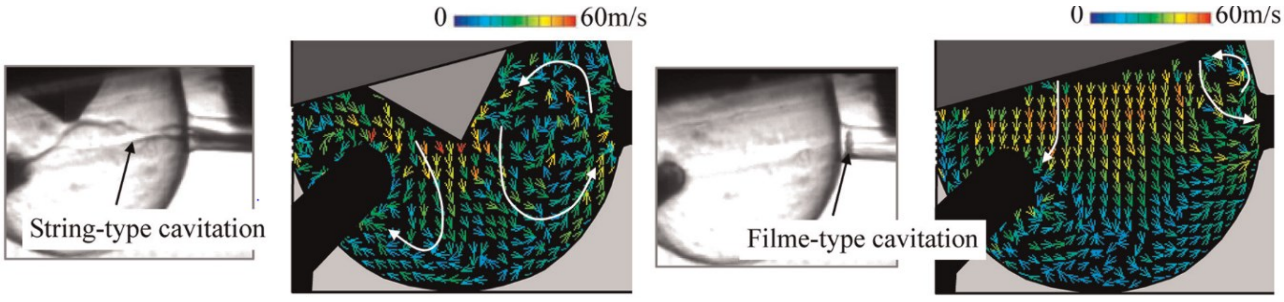

Figure 20 2D PIV in the sac of a real-scale mini-sac fuel injector [90]

1.5.3 Flow visualizations in metal nozzles

So far, all of the visualization studies discussed in the current subchapter were carried out with model nozzles. These model nozzles are usually created from various kinds of optically transparent materials, such as Polyether Ether Ketone (PEEK), acrylic, quartz or sapphire. As transparent materials are normally less resistant to plastic deformation than metallic nozzles, these nozzles are often unable to reach the operating pressure in real fuel injectors before they break [108]. This does not include sapphire, whose strength properties closely resembles steel. However, sapphire's refractive index is quite different from the fuel that is normally used for combustion engines. The difference in refractive index can cause serious refraction problem in flow visualization of objects with extreme curvature, as is the case with fuel injector nozzles. For such cases, refractive index

matching [109], [110] between the working liquid (fuel) and the nozzle can be carried out. Refractive index matching is carried out by adding additives to the liquid, with the concentration determined by index difference of the nozzle and the liquid. However, there is a possibility that this will alter the physical properties of the liquid, which affects cavitation behavior in the nozzle. This is the risk of intrusive measures such as refractive index matching.

For non-intrusive measurement of multiphase flow field in opaque materials, an alternative of using transparent materials is conducting visualization with x-ray sources [111]. For multiphase flow, besides its ability to visualize flow inside opaque materials, x-ray also has the advantage of providing high contrasts in optically dense areas, such recirculation area where cavitation clouds are shed. In such areas, only the outermost profile of the vapor fraction can be visualized under visible light source. This is caused by phase boundaries between the liquid and vapor causes multiple scattering of light in the visible spectrum. However, x-ray has a shorter wavelength than visible light, which means it can pass such areas without undergoing scattering.

For visualization of internal flow of the nozzle and fuel spray, x-ray visualization techniques with synchrotron x-ray sources [112] are getting increasingly used in recent years. The difference between synchrotron x-ray source and common laboratory x-ray source is essentially its strength. X-ray beam generated by synchrotron have the unique characteristics of having a very high photon flux and very short wavelength. Because of this, synchrotron x-ray source can provide a far greater degree of brilliance than laboratory sources. This allows for a greater scope of x-ray diagnostic techniques to be used. For in-nozzle cavitation, some commonly used x-ray diagnostics include radiography [113]–[115], fluorescence spectroscopy [116]–[118], and phase contrast imaging [30], [116], [119]–[124]. X-ray phase contrast imaging (XPCI) is especially notable as one of the most widely utilized x-ray diagnostics in multiphase flow studies [112]. Example of XPCI image in a real steel nozzle is shown in Figure 21. As evident from Figure 21, XPCI enables clear visualization of cavitation structure like those obtained from 2D nozzles. Further explanation about XPCI will be discussed in the next subchapter.

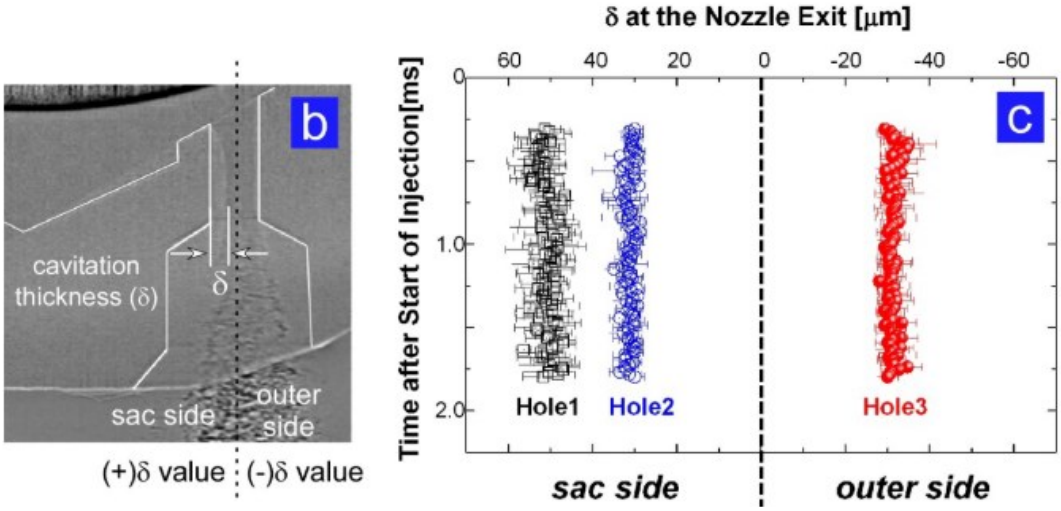

Figure 21 XPCI image and cavitation thickness measurement of a steel injector [120]

1.6 Flow Visualization Techniques

Most flows involve fluids, whether it is gas or liquid, whose motions are invisible to the human eye. Thus, for observation purposes, the motion of the flow must be made visible by certain techniques. Such techniques are called flow visualization, and they play an important role in the understanding of fluid-mechanical problems [125]. Besides enabling direct observation of fluid in motion, another important advantage of flow visualization is its ability to derive quantitative data that can be useful for further analysis of the flow.

The methods of flow visualization can be broadly classified into three categories [125]. The first one involves the addition of visible foreign material particles into the flow. If the particles are small enough, it can be assumed that the particles move in a motion that is almost the same as the flow, in respect to the direction and magnitude of the velocity vectors. Given that the observation is not carried out on the flow itself but on the particles, this method is an indirect method of observation. Thus, care should be taken to minimize the density difference between the particles and the fluid, which can cause relaxation phenomena in the particle. When such thing occurs, the particles do not reflect the “correct” motion of the flow. This is especially important for flow with variable density, such as compressible flow or multiphase flow. For such flows, visualization utilizing variation of the fluid density can give a more accurate result. Since refractive index is a function of density, visualization methods that are sensitive to changes in refractive index can visualize flow with variable density with high contrast. The density variation as usually reflected in the resulting images as local intensity variation. Such methods are known as optical flow visualization, which is the second category of flow visualization method. The third method of flow visualization combines the characteristics of the first and second methods. Commonly known as flow field marking, this method is carried out by adding energy (electricity or heat) at a certain point in the flow. This will increase the energy level of the “marked” fluid, causing them to become self-luminous. As such, the marked fluid can then be singled out from the rest of the fluid in the flow. This method is also called spark tracer method, and is usually only used for low-density fluids.

According to Dudukovic [126], multiphase flow visualization techniques should have (i) High spatial and temporal resolution for local phase fraction and velocity field measurements, and (ii) the capability to provide instantaneous and time history snapshots of the flow. However, a single experimental system that can satisfy both of these requirements does not exist, hence why multiple approaches are sometimes used to study a single sample/case. In the next part, several flow visualization techniques relevant to this dissertation will be briefly explained. Each explanation includes examples of the result obtained with each technique.

1.6.1 Shadowgraph

The simplest method of visualizing flow with different refractive index is the shadowgraph, which was first used by Dvorak in 1880 [127]. Shadowgraph falls to the second category of flow visualization, the optical flow visualization. As the name suggests, shadowgraph utilizes the variation

of the shadow cast by materials with different densities to reveal non-uniformities in a sample. For multiphase flow, this means that disturbance that occurs in the structures of fluid with different densities is observable in shadowgraph images. Because of its simplicity, the most basic shadowgraph observation can be done even without any additional optical component.

Schematic of a typical shadowgraph system is shown in Figure 22. For shadowgraph imaging, a point light source is commonly used. When the incident light transmitted from the light source hits the flow, the light is bent by refraction and have an angle of inclination with respect to their path, as shown in Figure 23. Figure 23(a) is equivalent to a fluid field with constant density. If the density in the flow is not constant, the shadow images will reflect the density variation by showing different local intensity in the captured images, as shown in Figure 23(b)-(d). Thus, to accurately reflect the structure of the flow, it is important to have a uniform illumination in all parts of the imaging plane.

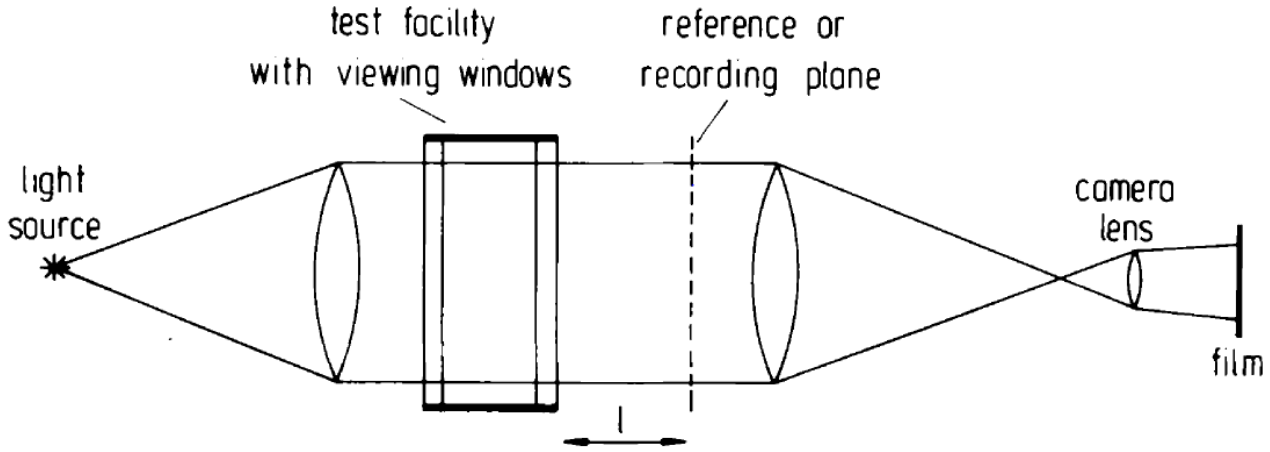

Figure 22 Typical shadowgraph imaging setup [125]

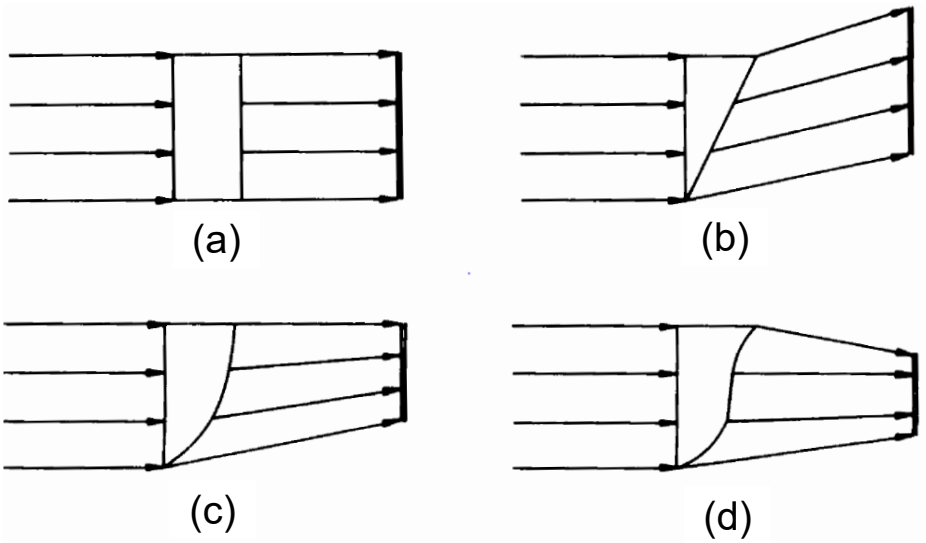

Figure 23 Deflection of coherent light in fluid with (a) constant density, (b) constant density gradient, (c) constant second derivative density, and (d) variable second derivative density

Because of its simplicity, shadowgraph is one of the most widely used flow visualization techniques for multiphase flow. In addition, shadowgraph's capability to observe granular flow

structure is also advantageous for visualization of turbulent flow. Figure 24 shows an example of such case, for cloud cavitation vortex shedding in a nozzle. It should be noted that although the structure of the flow can be reflected with fair accuracy with shadowgraph, a more detailed quantitative information, such as local void fraction and velocity profile, could not be obtained without additional integration from the shadowgraph images alone. This is because of the three-dimensional nature of a turbulent flow.

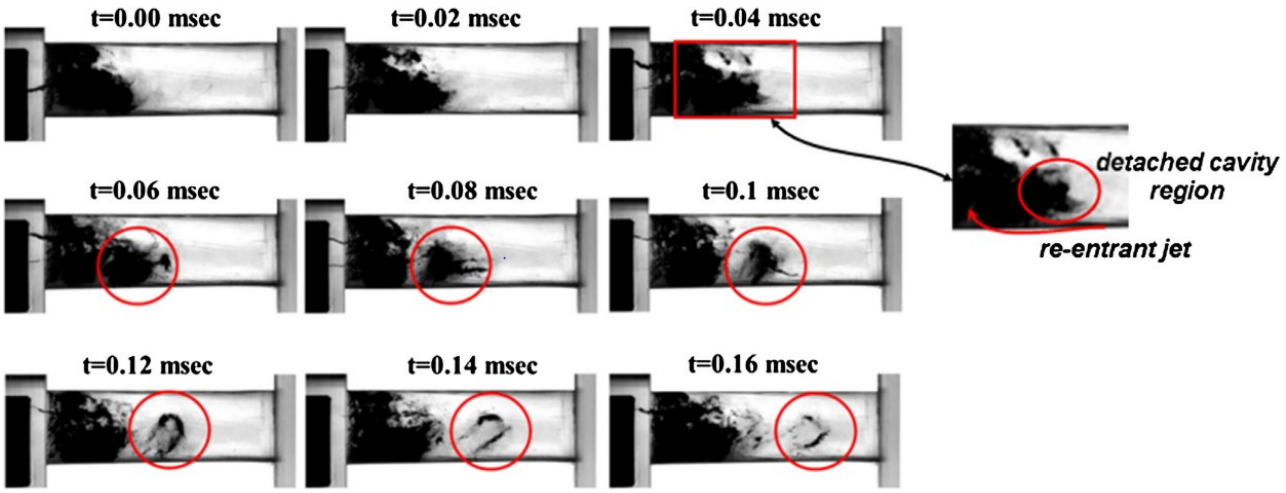

Figure 24 Images of cloud cavitation vortex shedding obtained with shadowgraph [94]

1.6.2 Tomographic Stereo Particle Image Velocimetry (TSPIV)

As explained previously, by adding visible foreign particles to fluid flow, it is possible to observe the motion of the flow by observing the particles' movement. This is the principle behind Particle Image Velocimetry (PIV), as can be seen in Figure 25 [128]. Should the appropriate particle size and density are used, it can be assumed that the particles represent the flow pattern of the fluid, thus the dynamics of the fluid can be quantitatively analyzed. Quantitative data such as velocity vector and magnitude can be obtained by evaluating the captured particles images, usually by conducting cross-correlation analysis.

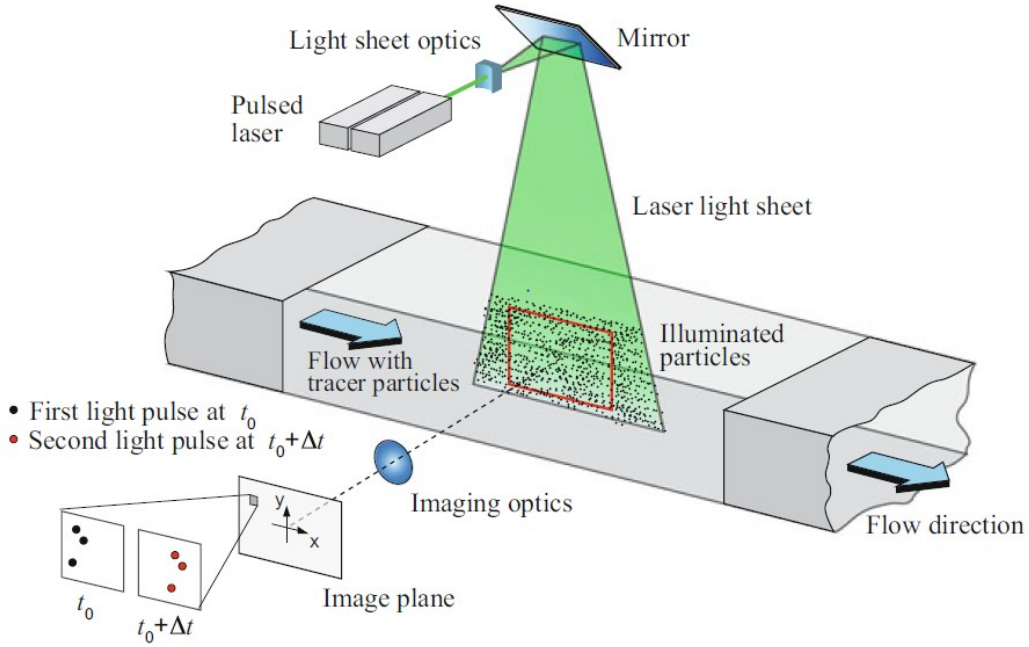

Figure 25 Basic configuration of a 2D PIV system [128]

Given its ability to extract velocity data from the flow, PIV is an indispensable tool for experimental fluid mechanics. Given that turbulence is still considered an unsolved problem in the field of physics, PIV is event more instrumental for revealing fundamental aspects of turbulent flow structure [129]. However, a conventional PIV can only obtain 2D flow components. In other words, only velocity components for two axes, i.e. x and y, can be derived by conventional PIV analysis, as 2D images were used. For most real-world cases, the flow is generally three-dimensional (3D). this can introduce additional rotational component to the flow, which necessitates the measurement of third velocity component, i.e. z-axis velocity component, to represent the flow structure correctly. Stereoscopic PIV was developed for such case. By adding a second camera to an initial 2D PIV setup, two simultaneous but distinct off-axis views of the same region of interest can be obtained. The two views can then combined with to obtain the three-dimensional velocity components of the flow [130]. Example of a stereoscopic PIV schematic is shown in Figure 26.

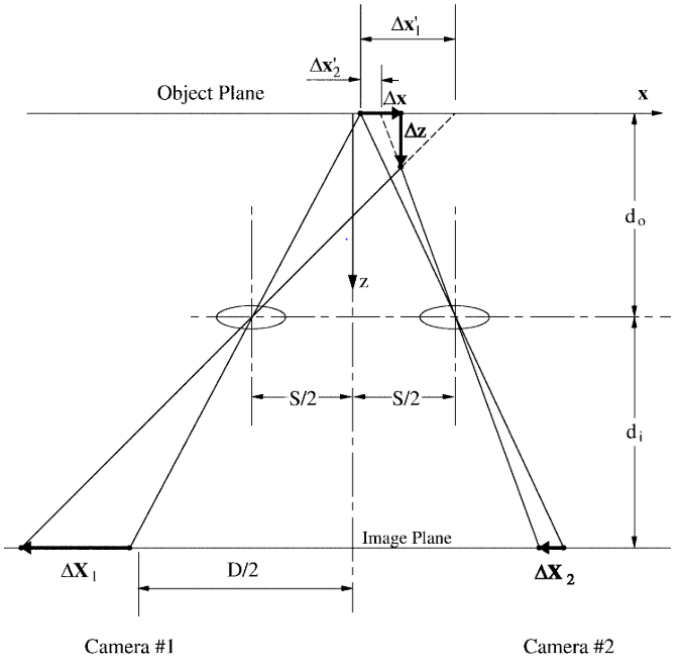

Figure 26 Basic schematic of a stereoscopic PIV system [130]

Although 3D velocity components can be obtained with stereoscopic PIV, the velocity components are still limited to a single plane of measurement. For flow field in a complex geometry, such as the internal flow of a fuel injector, 3D velocity components of a single plane is rarely sufficient to explain the flow. Because of this, sometimes stereoscopic PIV is carried out on multiple planes of measurement, by adding a second set of cameras (which makes for four cameras in total) [131]. Such PIV system is known by several names, such as multi-plane stereoscopic PIV, dual-plane stereoscopic PIV, or Tomographic Stereoscopic PIV (TSPIV) [132]. Similar to the stereoscopic PIV, TSPIV takes four views of the same region of interest. By utilizing 3D light intensity distribution, the views are then reconstructed as a single 3D image, which contains 3D velocity components data from multiple planes. Example of 3D velocity components obtained from TSPIV is shown in Figure 27.

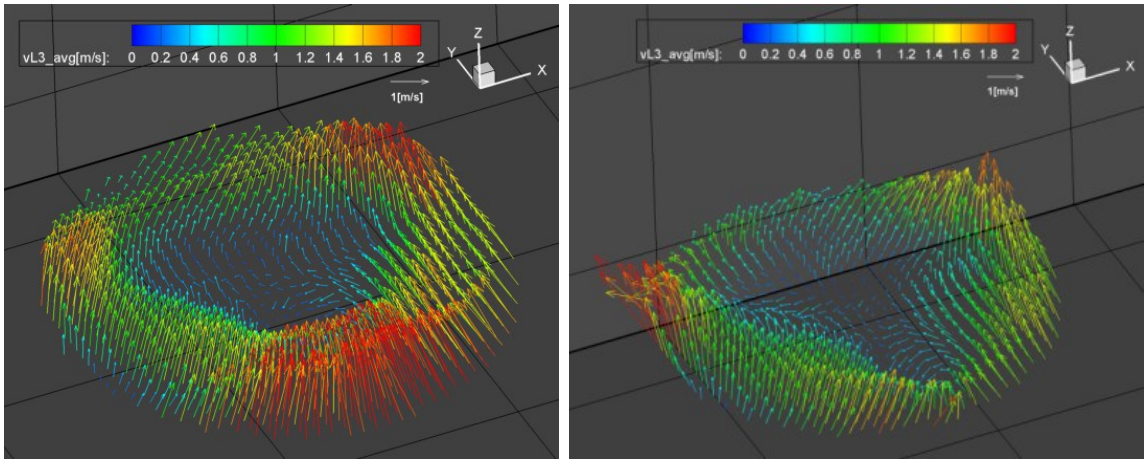

z=-2 mm z=-1 mm

Figure 27 3D velocity components of a mini-sac fuel injector as measured by TSPIV

1.6.3 X-ray phase contrast imaging (XPCI)

Thus far, all the flow visualization methods described in the current subchapter relies on light in the visible spectrum to capture images of the flow. However, as explained before, objects with different densities refract light rays differently. With visible light, this can cause multiple scattering problem when capturing images of flow in regions with continually changing void fraction, such as cavitation cloud. Thus, for such optically dense region, visible light can only be used to capture the outermost profile. However, beams with a very short wavelength and high photon flux, such as those generated by synchrotron x-ray source, can pass through optically dense sample without suffering from severe scattering. Hence, synchrotron x-ray beam can be used to visualize optically dense areas in multiphase flow field that is otherwise impossible to be visualized with visible light.

Although various synchrotron diagnostic techniques exist, X-ray phase contrast imaging (XPCI) is especially notable as one of the most widely utilized x-ray diagnostics in multiphase flow studies [112]. The principle of XPCI is built on the differences of refractive index between objects with different densities [133], [134]. When x-ray beam passes through an object, the diffracted x-ray will cause the incident x-ray to phase shift, which results in a Fresnel diffraction pattern along the object and its surrounding. For multiphase flows, this pattern is useful to visualize the boundaries of the gas/liquid interface of a complex sample with a high contrast. Furthermore, as with other x-ray diagnostics techniques, objects with different density causes different intensity attenuation from the absorption, which is also reflected in the images captured with XPCI. These properties make it possible to capture high-contrast images of complex multiphase flows with XPCI. In XPCI images, cavitation bubbles show up as the region with high intensity, whose boundaries from the surrounding liquid is marked by darker Fresnel fringes. Example of cavitation XPCI images can be seen in Figure 28.

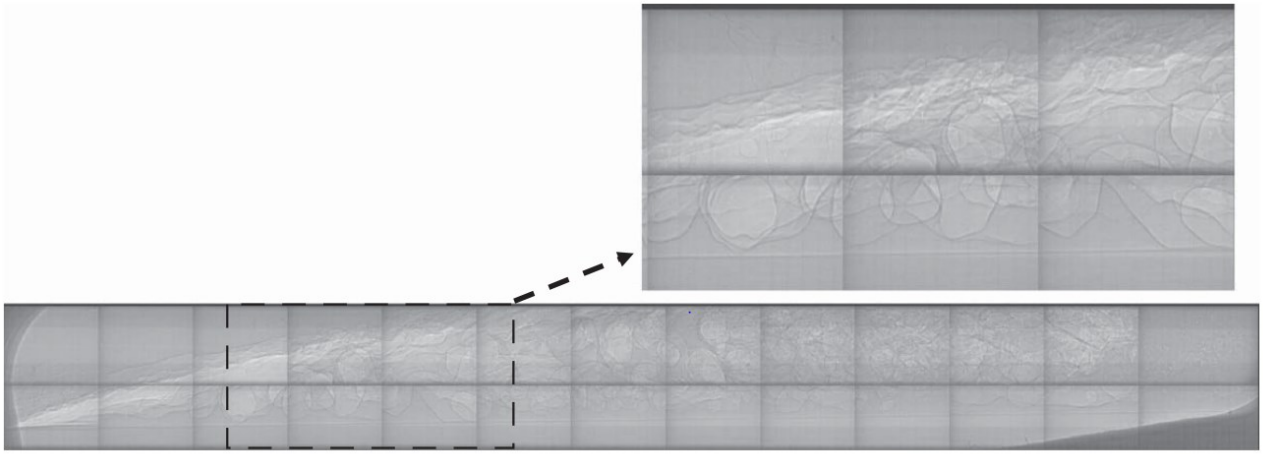

Figure 28 XPCI image of bubbles shedded from cavitation film in a venturi nozzle [135]

1.7 Objectives

From the background and the discussion of the previous studies, we have known that there still are unsolved problems and gaps in how in-nozzle cavitation affects the primary break-up of discharged liquid jet. Too much variation exists in the scope of the available studies, e.g. nozzle geometry, nozzle size, injection scheme, etc. The current study is conducted to fill the gap between the studies of in-nozzle cavitation carried out in laboratory setting vs those carried out under real operating condition. The objectives of the dissertation are as follows:

1. Quantitatively evaluate the effect of the difference in nozzle size and nozzle upstream geometry to incipient cavitation bubbles and the discharged liquid jet from 2D nozzles with various sizes
2. Investigate the applicability of the data obtained under steady injection condition to transient injection processes, as well as clarifying the cavitation inception process under transient and steady injection condition.
3. Individually clarifying the effects of string cavitation and geometrical cavitation to discharged liquid jet, as well as revealing the mechanism behind string cavitation formation.

1.8 Dissertation Structure

This dissertation is written in five chapters. A brief explanation of the contents of each chapter is given as follows:

1. Chapter 1 explains the background of this research. Following the background, a brief explanation of fuel injector and cavitation is discussed to let the readers understand the importance of fuel injector for a combustion engine, the physical phenomenon of cavitation, and why its occurrence is important for studies of fuel injector. Literature review of the studies on in-nozzle cavitation is also given in the current chapter, which gives the explanation on the understanding obtained from previous studies and where they still fall short. The readers can then understand the importance of this dissertation in terms of contribution to the field of cavitation studies.
2. Chapter 2 discusses the effect of the difference in nozzle size to incipient cavitation bubbles and the discharged liquid jet. XPCI visualization of in-nozzle cavitation and discharged liquid jet from 2D nozzles under various cavitation regimes were carried out. In addition, XPCI images of nozzles with different upstream geometry was also carried out. Quantitative analyses of the result were conducted and the result is given in this chapter.
3. Chapter 3 investigates the applicability of steady injection data to transient injection processes. A lot of cavitation studies were carried out under steady injection condition, which is different from the transient injection processes in real fuel injector nozzles. Comparison between the two processes was shown in this chapter, to clarify the validity of result of in-nozzle cavitation studies obtained under steady injection condition. Additionally, XPCI imaging of cavitation inception at

transient and steady injection condition was carried out to clarify the cavitation development process.

4. Chapter 4 gives the result of an investigation carried out with an enlarged 3-hole mini-sac injector with realistic geometry. Several studies have tried to clarify the mechanism behind string cavitation occurrence, although the mechanism is still hitherto unknown. This chapter presents the result of TSPIV analysis on the nozzle, which clarified the occurrence of string cavitation. Furthermore, high-speed imaging of internal flow in the nozzle and the discharged liquid jet is also carried out to individually clarify the effects of geometrical and string cavitation.
5. Chapter 5 concludes the overall achievement obtained during the course of this research. This chapter also summarizes all the discussion given during the course of this dissertation.

2 X-RAY STILL IMAGING OF CAVITATION IN NOZZLES AND DISCHARGED LIQUID JET

2.1 Advantages of still x-ray imaging for in-nozzle cavitation

In this chapter, results of the investigation carried out on x-ray still images of in-nozzle cavitation and discharged liquid jet are presented. Many studies have been conducted in nozzles with various sizes, ranging from real scale nozzles (⌀ ≈ 100 μm) to enlarged model nozzles with ⌀ ≈ 4000 μm. A wealth of data has been obtained from these studies, although there are some doubts regarding the applicability of studies conducted with enlarged nozzles to real-world operating conditions. As multiple scattering phenomena prevent clear visualization of cavitation bubbles, these doubts have been unresolved thus far. Hence, X-Ray Phase Contrast Imaging (XPCI) was carried out on nozzles with various sizes to investigate the effects of nozzle size difference on cavitation bubbles. XPCI was also carried out on the wavy interface structure of the discharged liquid jet to clarify the effects of cavitation in nozzles with different sizes. Finally, comparison of XPCI images in symmetrical and mini-sac nozzles with similar sizes was also carried out to investigate the effect of different upstream geometry to in-nozzle cavitation and discharged liquid jet.

2.2 Methodology

2.2.1 Experimental setup of X-ray still imaging

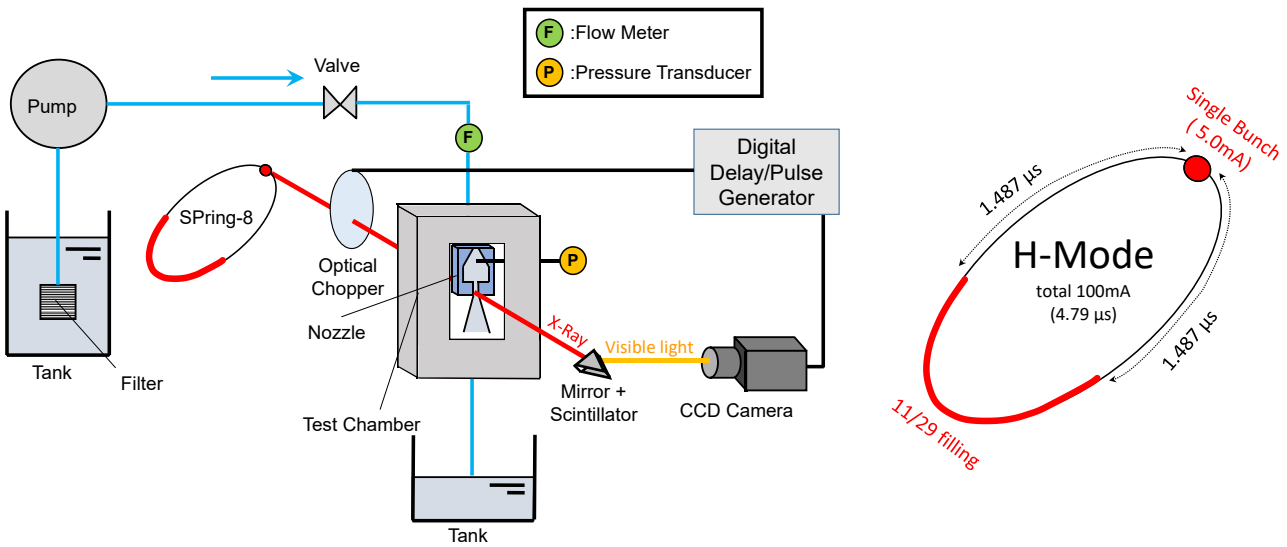

(a) Experimental setup (b) H-Mode filling pattern of SPring-8

Figure 29 Experimental setup of the X-ray still imaging

The experimental setup is shown in Figure 29(a). The XPCI experiment was carried out with a polychromatic pink x-ray beam at the Experimental Hutch 2 of the BL40XU beamline [136], which is located at the Super Photon Ring – 8 GeV (SPring-8) synchrotron radiation facility. XPCI was carried out with a polychromatic pink beam, a quasi-monochromatic x-ray beam with a sharp energy bandwidth possessing nearly 100 times higher photon flux than normal monochromatic beams [137].

Further details of the BL40XU beamline is available from SPring-8's website [138]. The imaging was carried out with an x-ray beam with 12 keV energy, which possesses a photon flux of 1 x 10^{15} phs/s. An optical chopper chopped the generated x-ray beam so that the x-ray beam was only passed to the nozzles at the instance of the imaging. This helps to reduce the heat load at both the sample and the optics. Single electron bunch from the SPring-8's H-mode filling pattern (11/29 + 1 bunch, 1487 ns interval) was used in this study. The H-mode filling pattern is illustrated in Figure 29(b). The single electron bunch of H-mode has 5.0 mA in current, with 80 ps in full width at half maximum (FWHM) length. A Lu-Si-O scintillator crystal was used to convert x-ray beam into visible light (420 nm), which was then reflected by 45° mirror and captured by a CCD camera (Hamamatsu Photonics Orca II-ER; equipped with Mitutoyo M Plan APO 20x objective lens). The timing of the optical chopper and the camera trigger was controlled with a digital delay/pulse generator (Stanford Research System DG5353). Imaging area size was about 0.4 mm x 0.5 mm, with a spatial resolution of 1.0 μm / pixel. In theory, this resolution could resolve bubbles whose sizes are larger than 1.0 μm. However, in practice, bubbles with less than 4.0 μm in diameter cannot be observed clearly.

Injection was carried out under atmospheric ambient pressure and room temperature condition, with an injection pressure $P_i \approx 0.2$ MPa. A plunger-type pump was used to discharge filtered tap water at room temperature through the nozzle, which was mounted in the test chamber. The flow rate of the pump was varied to produce different cavitation regimes in the nozzle. Still images of in-nozzle cavitation and the discharged liquid jet from the nozzles under incipient cavitation, super cavitation, and hydraulic flip regimes were taken with XPCI. The cavitation regimes were determined from the ratio of average cavitation length L_c normalized against the nozzle length L, where $0 < L_c/L < 0.6$ for incipient cavitation, $0.6 \leq L_c/L < 1$ for super cavitation, and $L_c = 1$ for hydraulic flip. Average velocity V in the nozzle, which was derived from the flow rate of the pump using mass continuity equation, was used to predict L_c/L [98]. The Reynolds number Re and Weber number We of all experimental conditions are shown in Table 1. Re and We are given by:

$$\mathrm{Re} = \frac{VW}{\nu} \quad (1)$$

$$\mathrm{We} = \frac{\rho V^2 W}{\gamma} \quad (2)$$

where V is the average velocity in the nozzle, W is the nozzle width (taken as the characteristic length), ν is the kinematic viscosity of the liquid ($\nu = 0.8007$ mm^2/s), and γ is the surface tension ($\gamma = 0.0719$ N/m).

Table 1 Experimental conditions of the x-ray still imaging

Nozzle type	Nozzle width W [mm]	Cavitation regime	V [m/s]	Re [-]	We [-]
Symmetrical nozzle	0.25	Incipient	15.3	4700	810
		Super	17.0	5300	1000
		Hydraulic flip	17.7	5530	1090
	0.50	Incipient	14.3	8930	1420
		Super	16.0	9990	1770
		Hydraulic flip	16.7	10430	1930
	1.0	Incipient	13.0	16200	2340
		Super	16.2	20200	3630
		Hydraulic flip	17.0	21230	4000
	2.0	Incipient	11.5	28700	3660
		Super	16.6	41400	7630
		Hydraulic flip	17.5	43700	8490
Mini-sac nozzle	1.0	Incipient	11.7	14610	1900
		Super	14.7	18360	3000
		Hydraulic flip	15.8	19700	3450

2.2.2 Schematics of the nozzles used for x-ray still imaging

The schematics of the 2D nozzles are shown in Figure 2. Four symmetrical nozzles and a mini-sac nozzle with different sizes were used in the experiment. All of the nozzles have an identical length/width ratio (L/W = 4). For the symmetrical nozzles, the width of the nozzles vary from 2.0, 1.0, 0.50, and 0.25 mm. The mini-sac nozzle width is 1 mm. The symmetrical nozzles with W= 2.0, 0.50, and 0.25 mm, as well as the mini-sac nozzle were comprised of a single aluminum or stainless steel plate, which was tightened between two acrylic plates with 3 mm in thickness. The symmetrical nozzle with W = 1.0 mm was created from two acrylic plates, one of which has a rectangular-shaped channel. Because the front and the back plates of all nozzles are made from acrylic, these nozzles have higher x-ray flux transmission compared to metal nozzles.

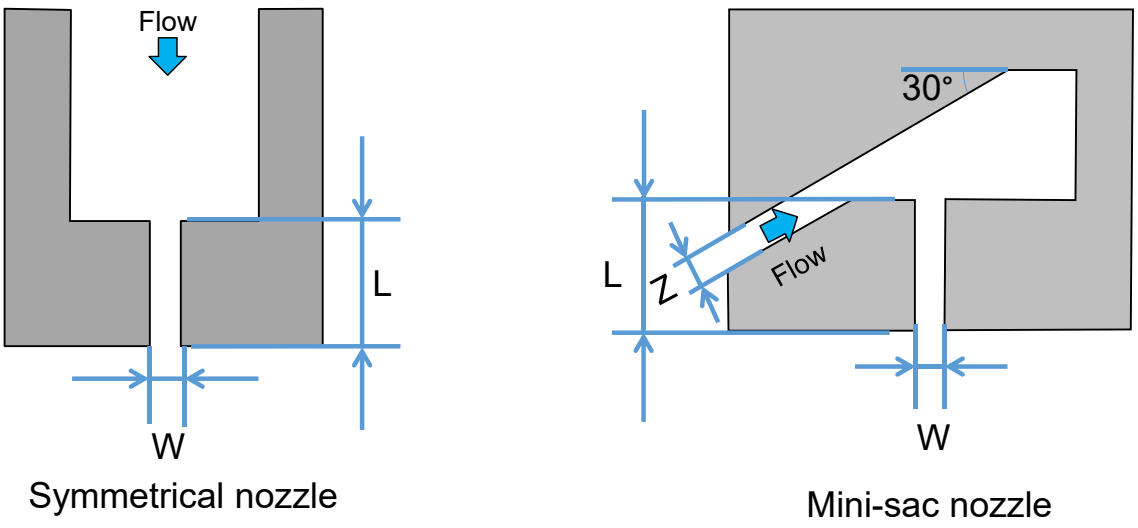

Figure 30 Nozzle schematics

The detailed specifications of the nozzles are shown in Table 2. Although the values of inlet roundness R of all nozzles are similar, the ratio of inlet roundness/width R/W increases as W decreases. In other words, R/W is higher in nozzles with smaller sizes. This is especially apparent for nozzles with W = 0.50 and 0.25 mm, which has a relatively high ratio of inlet roundness/width (R/W) compared to the nozzles with W = 1.0 and 2.0 mm (Table 2). R/W are known to affect boundary layer thickness of nozzle's internal flow, which is closely linked to in-nozzle cavitation profile in the nozzle. However, for an R/W difference of less than 10%, which were the case for the nozzles used in the current study, the change in cavitation profile is less than 4% [33].

Table 2 Detailed specifications of the nozzle

Nozzle Type	Nozzle length L [mm]	Nozzle width W [mm]	L/W [-]	Nozzle inlet roundness R [μm]	R/W [%]	Nozzle thickness T [mm]	Nozzle material
Symmetrical nozzle	8.0	2.0	4	20	1	1.0	Stainless steel
	4.0	1.0		20	2		Acrylic
	2.0	0.50		31.2	6.2	0.50	Aluminum
	1.0	0.25		25.9	10.4		
Mini-sac Nozzle	4.0	1.0		-	-		

2.2.3 Composite image creation

Due to the limitations of the x-ray beam size, the view field of the x-ray images was limited to 1 mm x 1 mm. Because of this, the images were captured at different positions of the nozzle to show the overall conditions of the flow. Twenty images were taken at each position. Since the x-ray images showed a reasonable repeatability for each shot, the images in each position were then selected arbitrarily to create a single composite image by post-processing. From the composite image, a representation of overall cavitation profile and liquid jet structures at different cavitation regimes can

be obtained. An example of a composite image of cavitation in super cavitation regime is shown in Figure 31 for the W = 1.0 mm symmetrical nozzle.

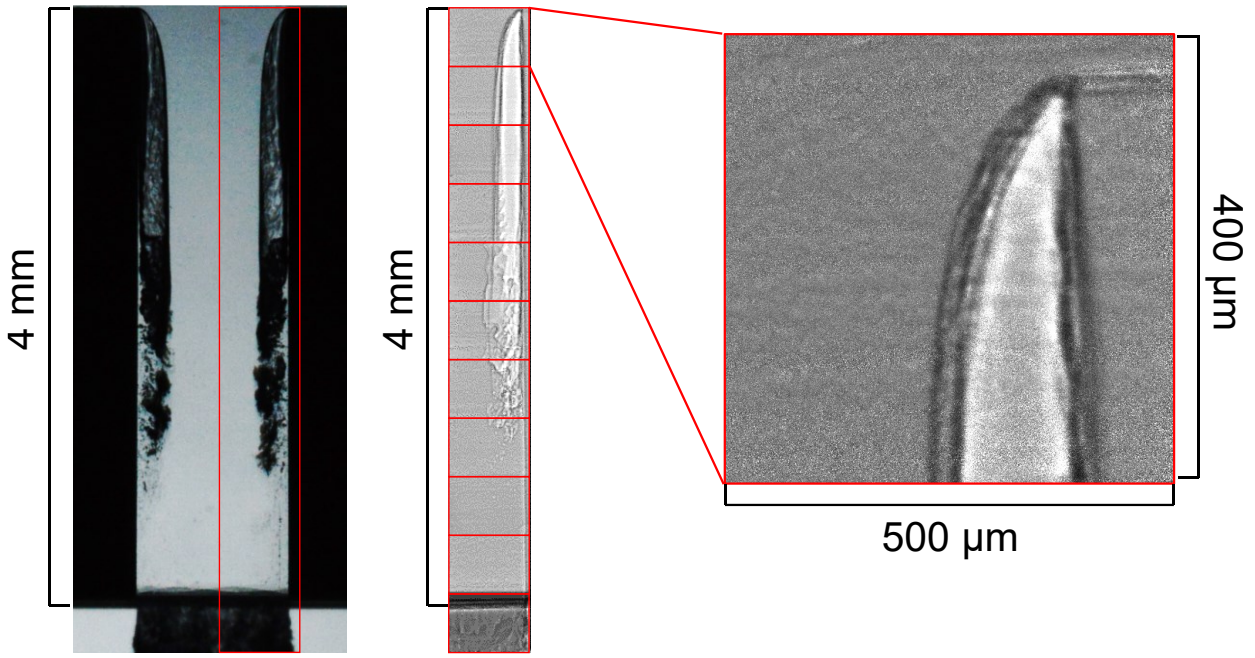

Figure 31 Composite image of cavitation in W = 1.0 mm symmetrical nozzle

2.2.4 Equivalent bubble diameter

To investigate the relationship between nozzle size and cavitation bubble size, measurement of bubble diameter was carried out on cavitation bubbles at incipient cavitation regimes in all nozzles. Figure 32(a) shows an example of incipient cavitation image of the W = 1.0 mm nozzle, with the measured bubbles shown in Figure 32(b). However, it can be seen from Figure 32(b) that the cavitation bubbles have a highly irregular shape, which made a precise measurement of bubble diameter to be difficult. Hence, the equivalent bubble diameter parameter D_e is used to evaluate the bubble sizes. As the nozzles used for the current experiment have rectangular profiles, it can be assumed that if a single big bubble fills a certain section of the nozzle, the diameter of the bubble can be approximated with the hydraulic diameter of a rectangular duct. Hence, Equation (3), which is derived from the hydraulic diameter formula for a partially filled rectangular duct, is used to approximate D_e:

$$D_e = \frac{2X_b Y_b}{X_b + Y_b} \tag{3}$$

where X_b and Y_b are the longest vertical and horizontal chord length of each bubble, respectively. The X_b and Y_b were measured from the projected rectangle around each bubble, as shown in Figure 32(c). Although D_e cannot be used to give an exact diameter of cavitation bubbles, it should reflect the trend of bubble sizes in each nozzle. This will allow some analysis of the relation between the scale of cavitation bubbles and that of the nozzles, which can be useful from a fundamental standpoint.

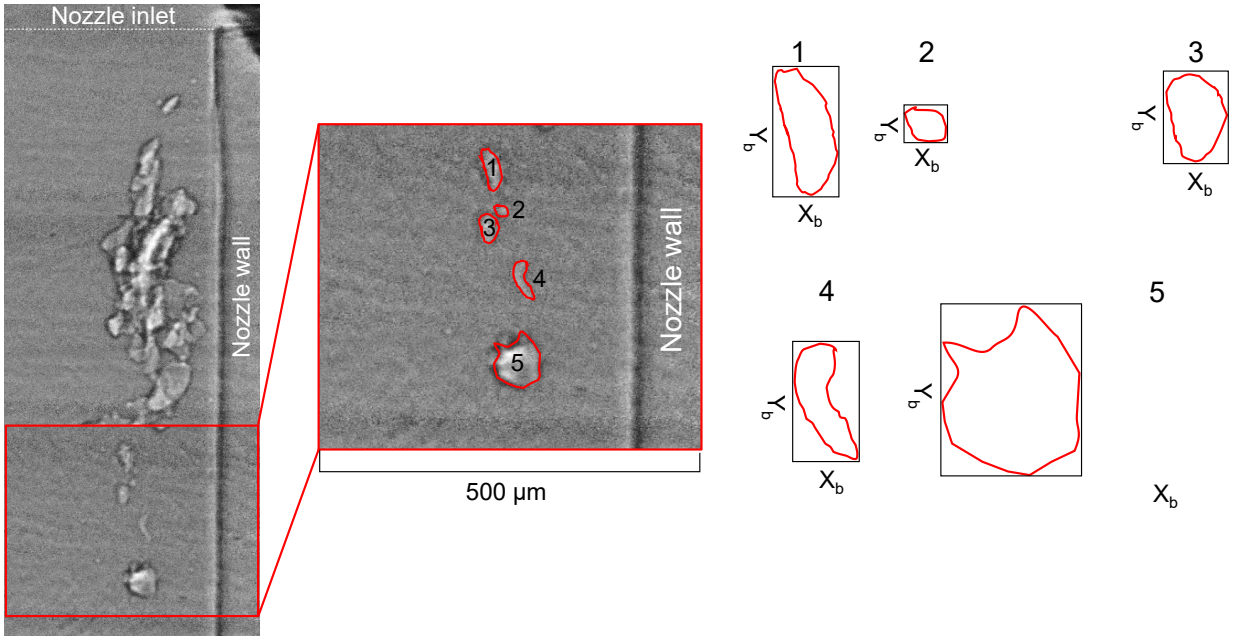

(a) Composite image (b) Original image (c) Measured bubbles

Figure 32 Measurement of equivalent bubble diameter D_e

2.2.5 Definition of perturbation length scale λ

At the interface of a deformed liquid jet, strong scattering and refraction occur when visualization is carried out with visible lights. Because of this, visible light visualization can only be used to observe the outermost profile of the liquid jet. In contrast, with XPCI, it is possible to observe the deformation of the liquid jet core with more details. This is because for XPCI produces image with clearly defined boundary and marked intensity variation between liquid and gas phase, as can be seen in Figure 33. The resulting images have a high contrast that is useful for multiphase flow analysis.

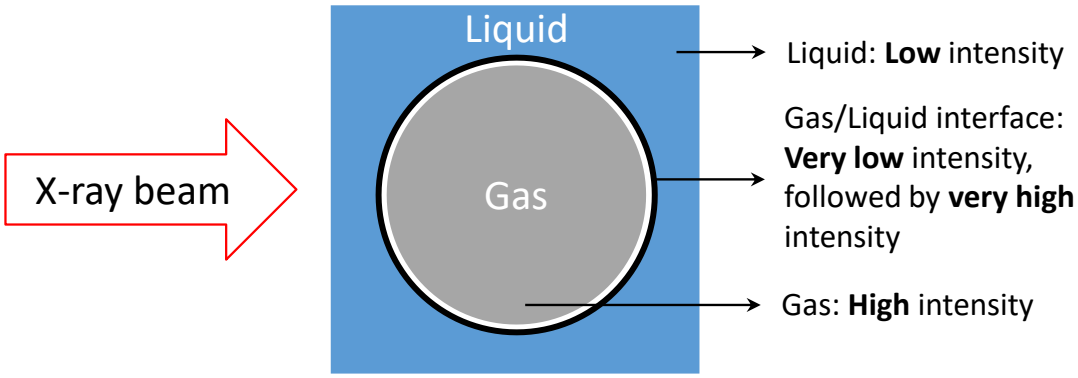

Figure 33 Illustration of contrast enhancement in XPCI images

For a deformed liquid jet where liquid and gas phases are intermingled, XPCI images of the discharged jet produces significant dark fringe lines between the features of the liquid jet. This can be seen in Figure 34(a). In theory, the produced dark fringes will increase as the liquid jet becomes more deformed. However, it is difficult to quantitatively measure the extent of liquid jet deformation using dark fringe lines only. As XPCI images have a path-length integrated nature, it is difficult to

estimate the location between two horizontally adjacent features, as illustrated in Figure 34(b). Two horizontally adjacent features can actually be located out of plane with respect to each other.

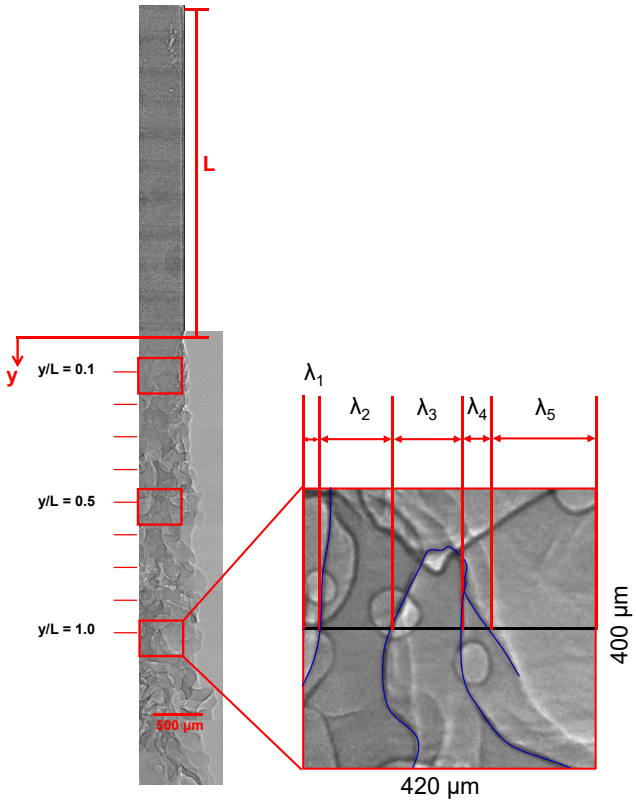

(a) Example of λ measurement

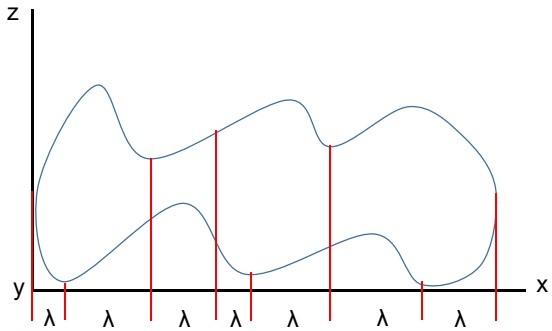

(b) Illustration of a top view of the discharged liquid jet

Figure 34 Perturbation length scale λ

To help quantify the liquid jet deformation on different experimental conditions, a perturbation length scale parameter λ is introduced. λ is defined as the average distance between two dark fringes of the liquid jet's features along the horizontal axis of the measurement point. Measurement of λ was carried out for incipient and super cavitation regimes at y/L = 0.1, 0.5, and 1.0. y is defined as the vertical distance from the nozzle exit (y = 0 at the nozzle exit) and L is the nozzle length. Example of measured features is shown in Figure 34(a). The black line in the middle of the enlarged inset of the sample of the measurement area in Figure 34(a) indicates the area where measurement of λ was carried out. The black line shows the exact position where y/L = 1.0, as can be seen from the zoomed out figure of the discharged liquid jet. For Figure 34(a), measurement of λ at y/L = 1.0 was only carried out for fringes that crossed this line. The fringes that were used for λ measurement were highlighted in blue. It should be noted that bubble features were not included for λ measurement, as the current study is focused on the deformation of the liquid jet core.

2.3 Results and Discussion

2.3.1 Composite images of incipient and super cavitation regimes in symmetrical nozzles

Examples of in-nozzle incipient cavitation images in symmetrical nozzles which were obtained with visible light (left) and XPCI (right) for different nozzle sizes are shown in Figure 35. It can be seen that the velocity at which cavitation inception occurs increases as the nozzle size gets smaller. This is caused by the difference in R/W for each nozzle sizes. Besides affecting the value of R/W, the difference in nozzle size can also cause the difference in the smallest turbulence scale in each nozzle. In turn, this might affect the scale of turbulence eddies and the resulting bubble size. To evaluate the turbulence scale, the Reynolds number Re is calculated, using W as the characteristic length.

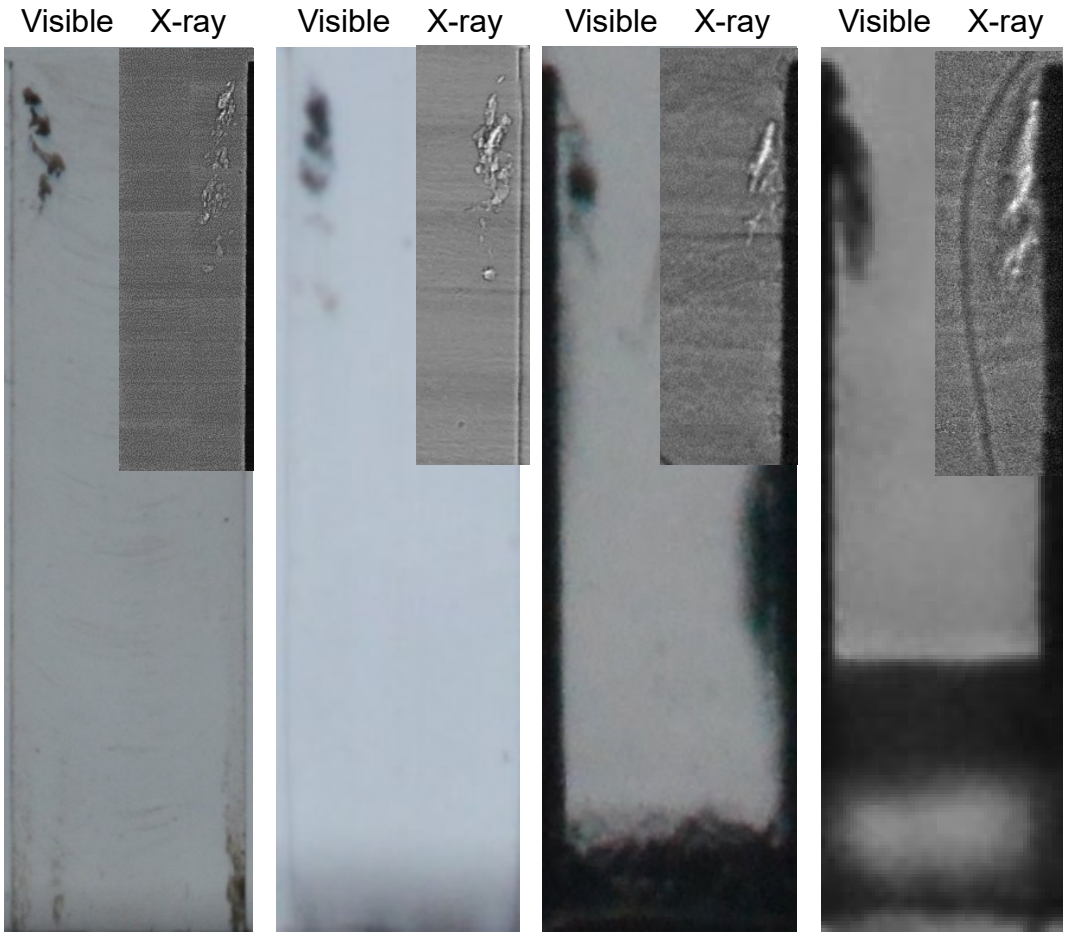

Figure 35 Comparison of in-nozzle incipient cavitation images captured using visible light (left) and XPCI (right)

From Figure 35, we can see that XPCI method made it possible to clearly visualize the structure of cavitation bubbles, especially in with W = 2.0 and 1.0 mm nozzles. The clouds are shown in the x-ray images as the region with higher intensity, as vapor caused less attenuation to the beam

compared to liquid. Besides the boundaries of cavitation cloud, the interface of individual bubbles in a cloud can also be observed in Figure 35. This indicates that a cavitation cloud, which shows up as a dark region in transparent nozzles under visible light experiments, consists of many deformed cavitation bubbles. The observed bubbles are restricted to the recirculation flow area near the nozzle wall, as a result of the velocity profile at the separated boundary layer in the nozzles [97]. The velocity profile also caused the bubbles to have elongated shapes with an irregular circumference. This finding is similar to those reported by Coutier-Delgosha [139] and Vabre [135], who carried out XPCI on internal cavitation flow in a venturi pipe. However, their studies were carried out for a more developed cavitation regime, with the bubble clouds concentrated near the tail end of the cavity. For the region near the inlet, Coutier-Delgosha and Vabre's studies showed features that resembled vapor sheet rather than bubble clouds. A more appropriate comparison with the current study might be obtained from the super cavitation regimes, which are shown in Figure 36.

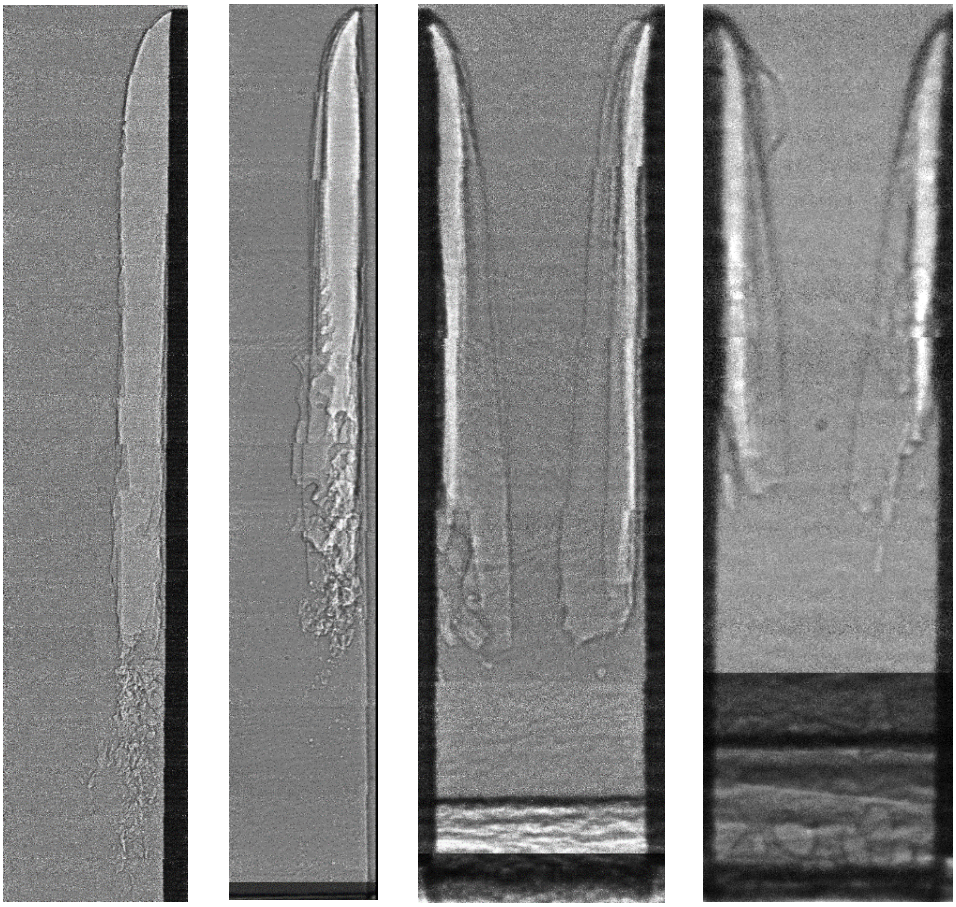

Figure 36 XPCI Images of super cavitation in symmetrical nozzles

For super cavitation regime, a single cavitation film with perturbed features at its tail end is formed along the nozzle walls. The perturbation indicates the transition from laminar flow separation at the nozzle inlet edge to the turbulent boundary layer, where a cloud of cavitation bubble is

continuously shed from the cavitation film tail due to the vortex shedding from the reattachment point. The tail end region of the cavitation film shows up as a foamy feature under visible light, like the one Arcoumanis et al. [49] observed with visible light. The scale of the perturbation is much less than those observed by Coutier-Delgosha and Vabre. It is highly likely that this is caused by the comparatively smaller diameter of the nozzles in the current study, compared to the venturi pipe used in Coutier-Delgosha and Vabre's studies. For internal cavitating flow, it has been shown that smaller sectional area can suppress cloud shedding at the tail end of a sheet cavitation [140], which might lead to weaker turbulence and less cavitation cloud. Figure 36 seemed to show some limited evidence to support this, as it is evident that there is less tail end perturbation for W = 0.50 and 0.25 mm nozzles, compared to those observed on W = 1.0 and 2.0 mm nozzles.

From the present x-ray images, it can be concluded that cavitation first occurs in the nozzle as a cloud of bubbles at low flow velocity, before turning into a single cavitation film as mean flow velocity increases. The features of the cavitation film observed in the current study agrees with those observed by Duke et al. [116] under transient injection condition in a cylindrical nozzle (0.5 mm in diameter D, L/D = 6.1). The injection pressure is higher in their study (0.9 MPa) compared to the injection pressure in the current study (≈0.2 MPa). The study showed a developed film cavitation 0.1 ms after the start of injection. The result suggests that the development of cavitation film from incipient cavitation happens within 0.1 ms under transient injection condition for 0.9 MPa injection pressure. This will be explored further in Chapter 3.

2.3.2 Comparison of X-ray images of symmetrical and mini-sac nozzles

Comparison of XPCI images of mini-sac and symmetrical nozzles with W = 1.0 mm width are shown in Figure 37. Incipient cavitation in both nozzles is observed as a cloud of tiny bubbles, before transforming into large cavitation film at super cavitation. At super cavitation regime, the tail end of the cavitation film near the flow reattachment area of mini-sac nozzle has a visibly greater perturbation compared to the cavitation film in symmetrical nozzle. This might be caused by a stronger turbulence in the mini-sac nozzle. Previous study conducted in 2D nozzles with eccentric sac configuration [93], [141] has shown that asymmetric inflow from the mini-sac nozzle's upstream can result in a stronger turbulence in the nozzle, which can influence the shape of cavitation film and the discharged liquid jet angle.

In both nozzles, it is clear that liquid jet structure becomes more perturbed when cavitation transitions from incipient to super cavitation, which shows the evidence of increasing jet deformation at super cavitation regime. However, the jet structure at hydraulic flip regime in both nozzle is very different. For symmetrical nozzle, the jet structure to become very smooth, as can be seen in Figure 37(a). On the contrary, Figure 37(b) shows that for mini-sac nozzle, the jet structure at the hydraulic flip regime exhibits similar perturbations with the jet structure at the super cavitation regime. This is caused by imperfect hydraulic flip [82] in mini-sac nozzle, in which reattachment of separated flow intermittently occurs. As a result, internal flow is turbulent and liquid break-up characteristic is comparable to that at super cavitation regime. Total hydraulic flip of the symmetrical nozzle can be

seen in Figure 37(a). At thy hydraulic flip regime, the vapor region in the symmetrical nozzle near the wall is completely composed of gas (air), which prevents flow reattachment. This results in aforementioned smooth jet structure, which prevents liquid jet deformation and break-up.

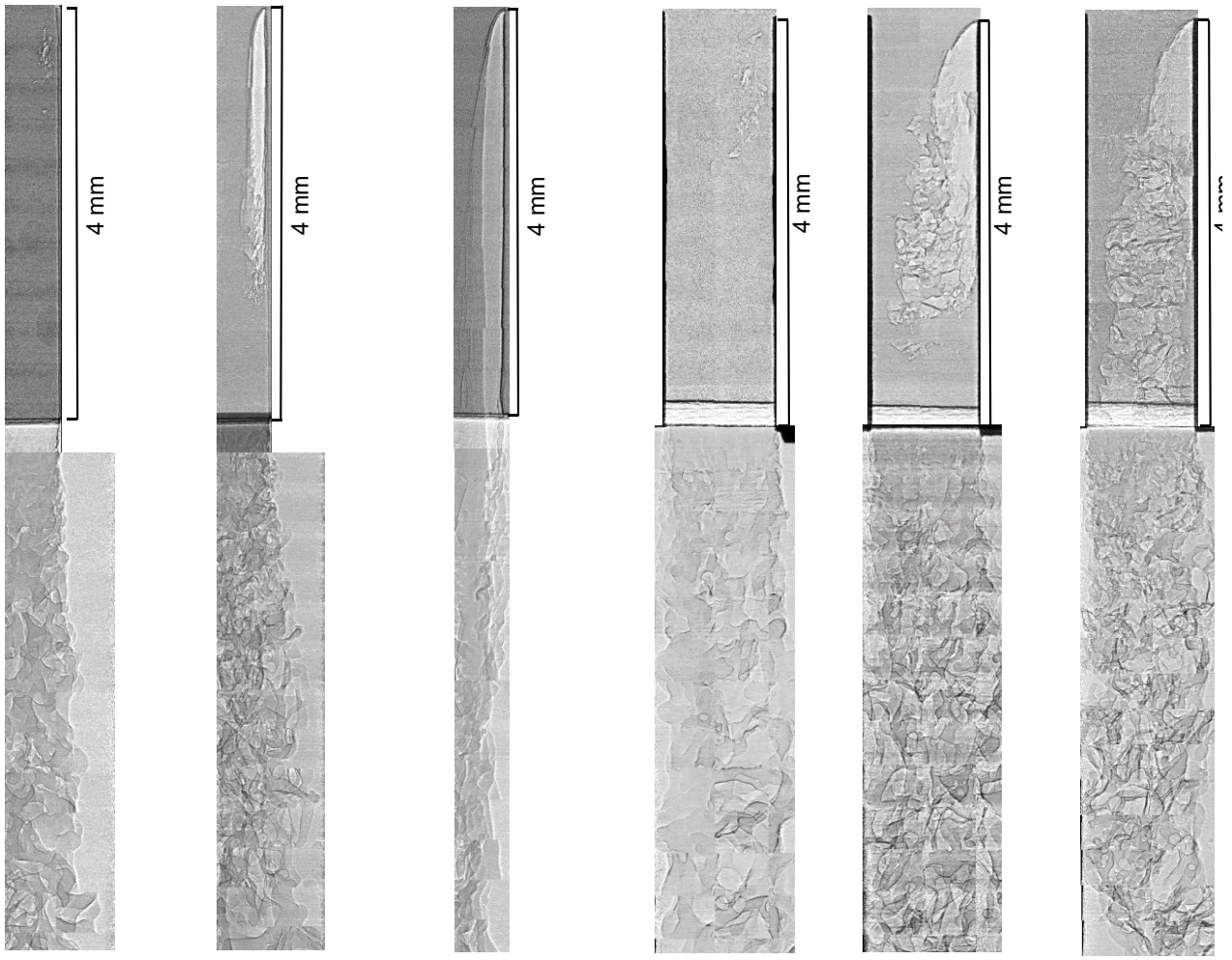

Figure 37 XPCI images of in-nozzle cavitation and discharged liquid jet from symmetrical and mini-sac nozzle (W = 1.0 mm)

2.3.3 Incipient Cavitation Bubble Diameter

Measurement of cavitation bubble diameter in the nozzles can give some clarification about the relationship between nozzle scale and bubble scale. Therefore, the equivalent diameter De of incipient cavitation bubbles in symmetrical nozzles are measured in this study. Results of D_e measurements for all nozzles are shown in Figure 38(a), while the normalized equivalent diameter D_e/W is shown in Figure 38(b). The numbers of measured bubbles in each nozzle are shown in Table 3; with the probability density of measured D_e is shown in Figure 39. It should be noted that as the measurement was only carried out on a limited amount of still images, the number of detected bubbles are quite limited in this study, as evident in Table 3. However, the measurement result shows

some clear trends between the size of cavitation and nozzle size. Figure 38 shows that the scale of the mean bubble diameter is proportional to the nozzle width, with an average D_e/W of 4%. We note that the value of D_e/W slightly decreases with increasing W. There are two possible explanations for the bubble size trend. First, as previously noted in section 2.2.1, the bubbles whose sizes are smaller than 4.0 μm cannot be clearly observed. More small bubbles can be lost in smaller nozzles, which causes the increase in measured D_e/W in smaller nozzles. Another reason for decreasing D_e/W with increasing W is the difference of turbulence scales between the nozzles. As previously seen in Figure 7, at incipient cavitation, Re = 28700 for W = 2.0 nozzle and Re = 4700 for W = 0.25 mm nozzle, respectively. This means that the relative turbulence scale in the large nozzle is six times larger than that in the small nozzle. Because the size of incipient cavitation bubbles is affected by the turbulence eddies, the difference in Re might cause the change in D_e/W.

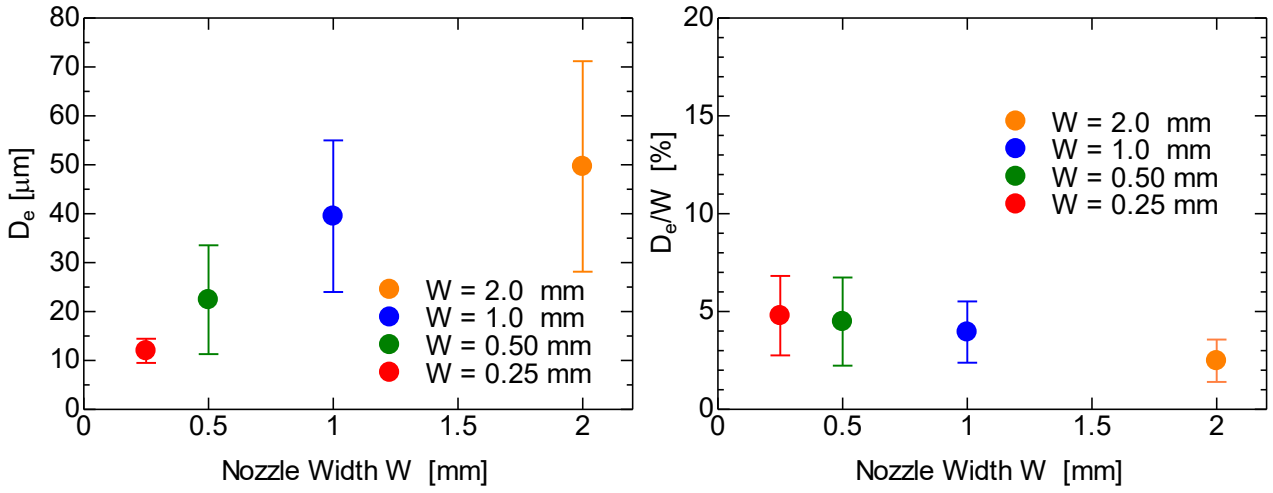

(a) Equivalent bubble diameter D_e vs nozzle width W

(b) Normalized equivalent bubble diameter D_e/W vs nozzle width W

Figure 38 Average diameter of incipient cavitation bubbles in symmetrical nozzles

Table 3 Measured bubble number

Nozzle Width W [mm]	Bubble Sampling Number [-]
2.0	76
1.0	46
0.50	41
0.25	13

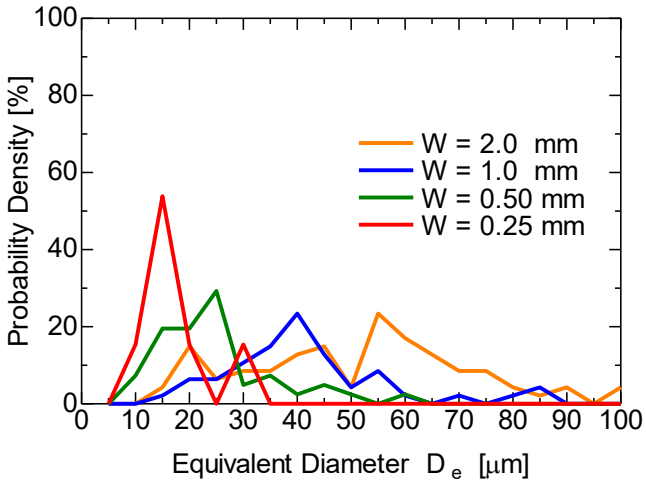

Figure 39 Probability density of incipient bubble size in symmetrical nozzles

In a previous study, Chaves [81] argued that cavitating flows in enlarged and real-size nozzles have different characteristics because the diameter of cavitation bubbles and bubble transit time does not scale with nozzle size. They argued that cavitation is only observable as a film for real-scale nozzles. Although measured D_e/W is not completely similar across all nozzles, the present measurement shows a trend of the relationship between incipient cavitation bubble diameter and nozzle size, in contrary to Chaves' suggestion that bubble diameter does not scale with nozzle size. The trend also means that some similarity exists between cavitating flows in small and large nozzles. As discussed previously, the size of the cavitation bubbles strongly depends on the turbulent eddy scale. As the turbulent eddy scale changes with the nozzle size, some degree of scalability exists between nozzle size and cavitation bubble diameter. This scalability proves the similarity of the behavior of cavitating flows in small and large nozzles. For in-nozzle studies, this result provides some supporting evidence for the applicability of results obtained with enlarged nozzles to small nozzles.

2.3.4 Perturbation on the interface of discharged liquid jet

Lastly, the effect of the difference in nozzle sizes and nozzle upstream geometry are explored here. First, the effect of difference in nozzle size to the discharged liquid jet is discussed. Composite images of in-nozzle cavitation and discharged liquid jet at various cavitation regimes for all symmetrical nozzles are shown in Figure 40. For W = 2.0 mm nozzle, only the images of in-nozzle cavitation are shown. For each nozzle, incipient cavitation, super cavitation, and hydraulic flip (left to right) are shown. Besides in-nozzle cavitation, XPCI has also enabled us to examine the structures of the wavy liquid jet at various cavitation regimes. Wavy patterns of the liquid jets for W = 1.0, 0.50, and 0.25 mm nozzles are shown in Figure 40(a), (b), and (c). At a glance, it is evident that perturbation of wavy jet is finer at super cavitation regime for all nozzles. Finer perturbation can be caused by stronger cavitation-induced turbulence acting on the interface of discharged liquid jets. The turbulence promotes ligament formation and consequently enhances liquid atomization. At hydraulic flip regime, the liquid jet structure is very smooth on the side where flow separation occurs, with minimal perturbations on the areas whose distance are less than 0.5 L from the nozzle exit. Wavy pattern is observed on the jet at the opposing side, although perturbation of wavy jet at hydraulic flip seems similar to those observed at incipient cavitation regime. This trend holds true for all nozzles. It should be noted that the scales of perturbations are visibly finer for W = 1.0 mm nozzle. This will be explained in more detail below.

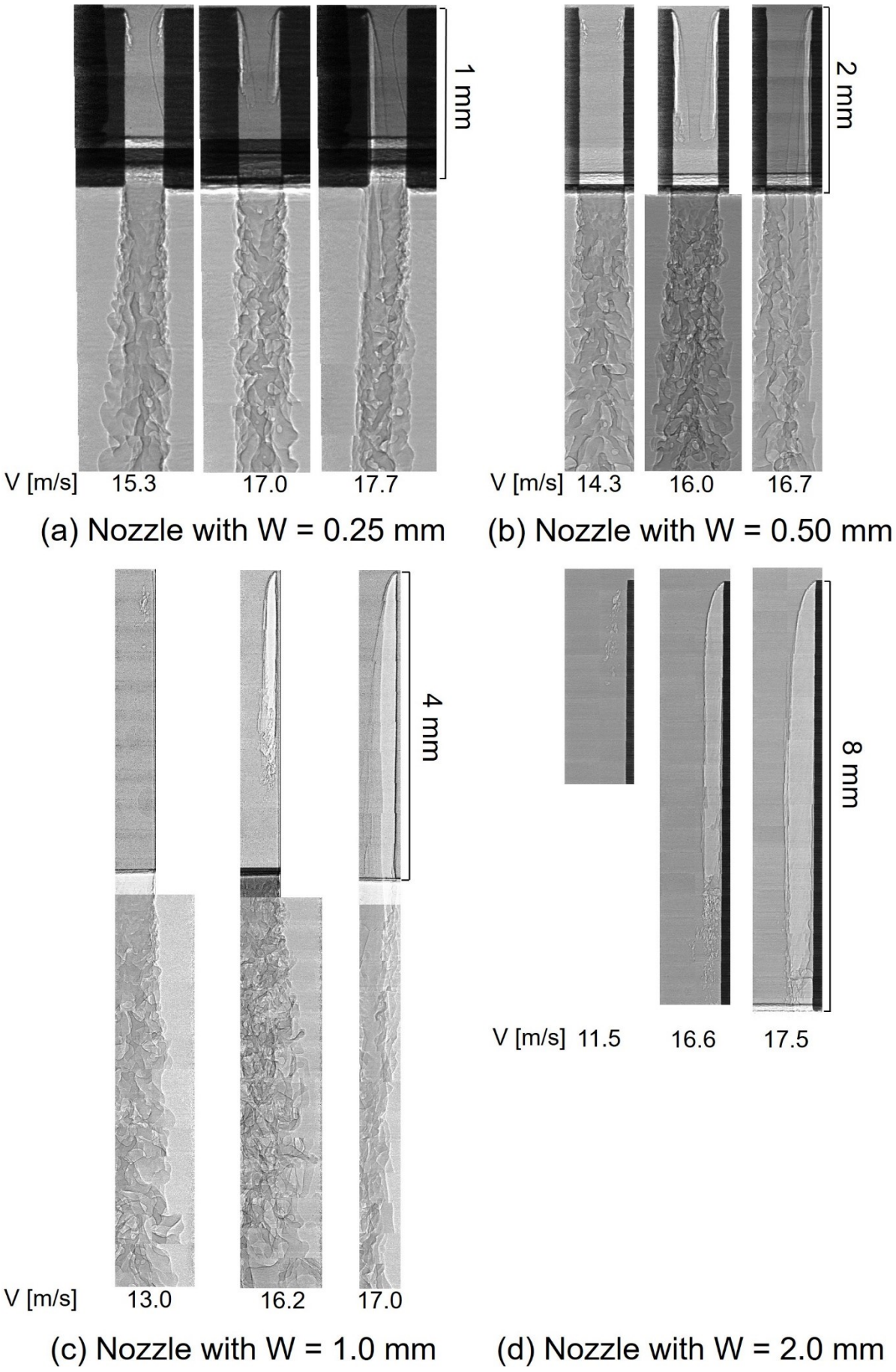

Figure 40 Composite images of in-nozzle cavitation and discharged liquid jet from symmetrical nozzles

Figure 41 shows the enlarged images of the discharged liquid jet for W = 1.0, 0.5, and 0.25 mm symmetrical nozzles at the incipient and super cavitation regimes. The enlarged images indicated by the red square shows the liquid jet cores with trapped gas bubbles. To investigate jet deformation in more detail, a perturbation length scale λ, as defined in Section 2.2.5, was measured for all nozzles. The measurement result is shown in Figure 42. As previously mentioned in Section 2.2.5, it is difficult to determine the exact location of each feature in a given frame using path-length integrated measurement method such as XPCI. However, as there are noticeable changes in the perturbation scale of the wavy jet with the changes in cavitation regime and nozzle size, measurement of perturbation length scale λ should reveal a trend between cavitation regime, nozzle size, and liquid jet deformation.

From Figure 42, the λ at y/L = 0.1 for super cavitation regime is clearly smaller than that for incipient cavitation regime, which signifies the effect of super cavitation on atomization enhancement of liquid jet core. This fact implies that deformation of the discharged liquid jet by super cavitation is not only confined to the outermost interface of the liquid jet but also affects the deformation of the liquid jet core.

For incipient cavitation regime, λ of all nozzles does not change much. Because the flow reattachment point at incipient cavitation is located far from nozzle exit, any turbulence induced by cavitation bubble collapse at this point dissipates far before it reaches the nozzle exit. Thus, the effect of cavitation on the liquid jet at incipient cavitation regime is minimal. However, λ becomes shorter at y/L ≥ 0.5, which might indicate that other factors besides cavitation are affecting the deformation of the liquid jet. Downstream from the nozzle exit, the interaction between the discharged liquid jet and the surrounding gas takes place, and this introduces various disruptions to the liquid jet interface. As a result, although the dominant force on the jet deformation at this area is not in-nozzle cavitation, jet deformation occurs and λ becomes shorter far downstream from the nozzle exit, even at incipient cavitation regime. This result is consistent with the result obtained by Osta et al. (2011), which shows an increased ligament formation in the liquid jet core far downstream from the nozzle outlet, even at non-cavitating conditions.

Finally, it is important to note the fact that λ increases with the decrease in the nozzle size, which is caused by the stronger surface tension force acting on smaller nozzle. To clarify the effect of surface tension, a normalized perturbation parameter λ/W is shown in Figure 43. It can be seen that λ/W in all measurement point becomes larger with the decrease in nozzle size, which shows that jet deformation is suppressed in smaller nozzles.

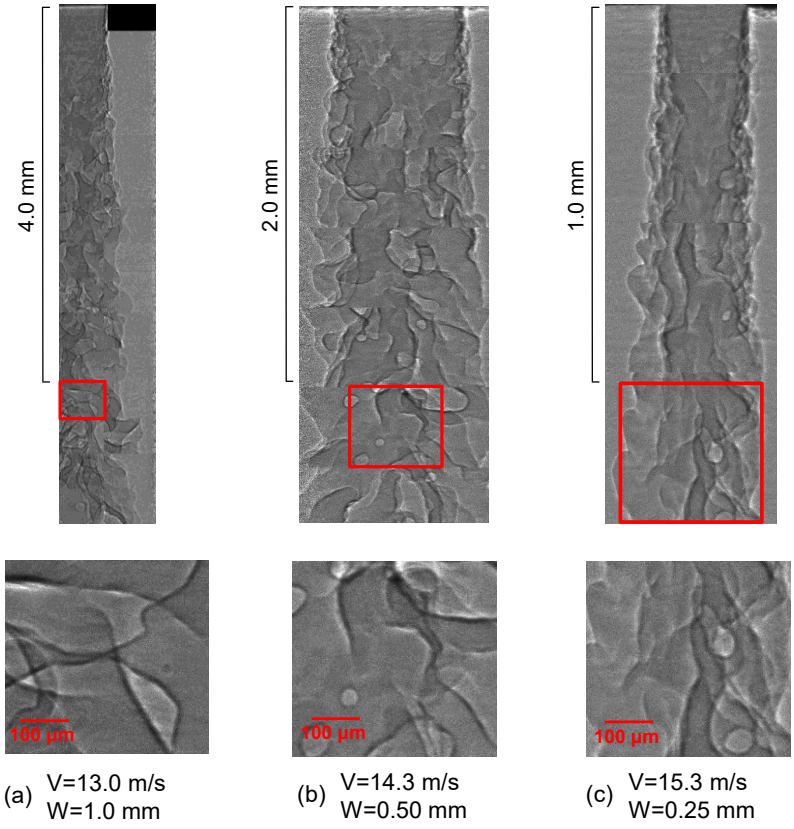

(a) Liquid jet at incipient cavitation

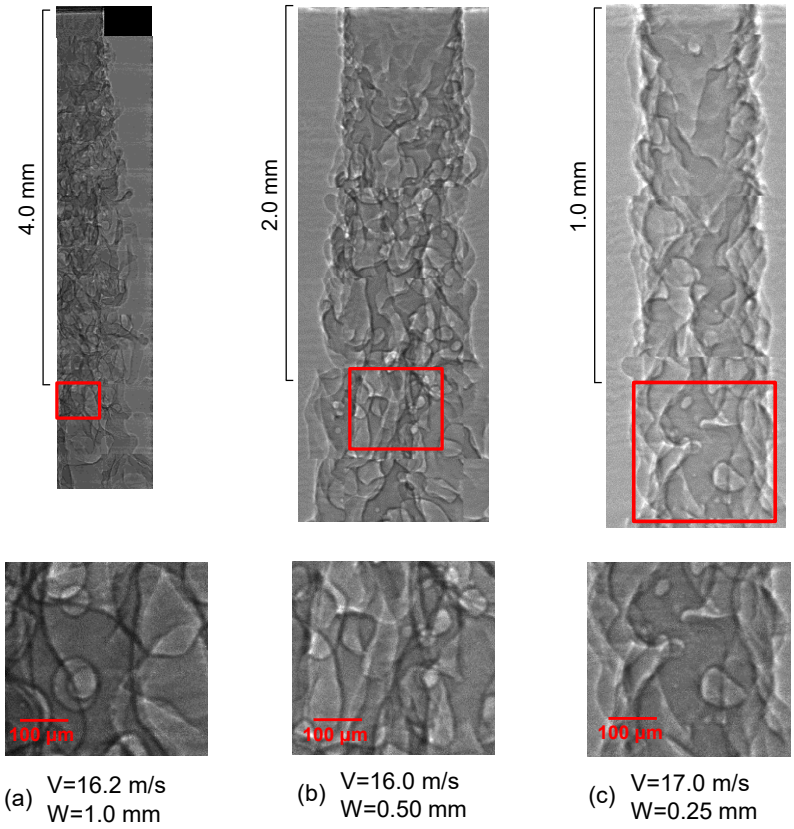

(b) Liquid jet at super cavitation

Figure 41 XPCI images of the discharged liquid jet from symmetrical nozzles at incipient (a) and super cavitation (b) regimes for nozzles with W = 1.0, 0.50, and 0.25 mm

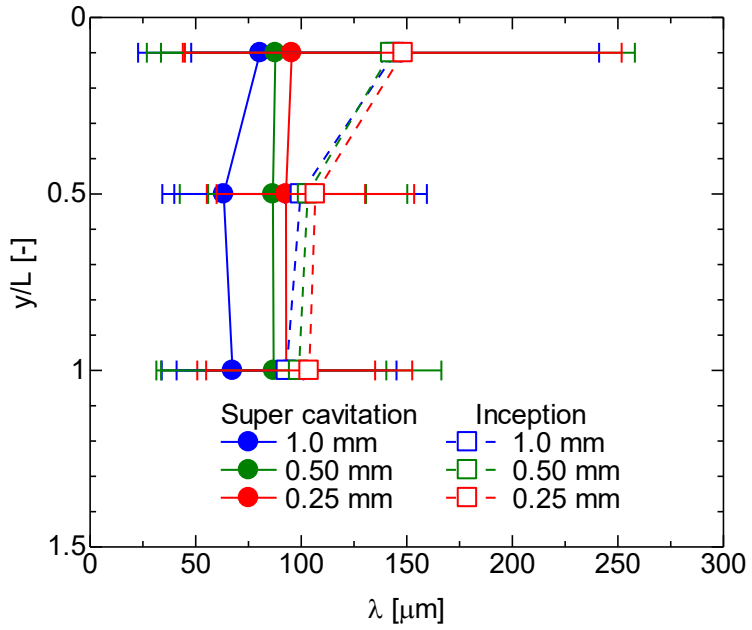

Figure 42 Measured perturbation length scale λ of W = 1.0, 0.50, and 0.25 mm symmetrical nozzles

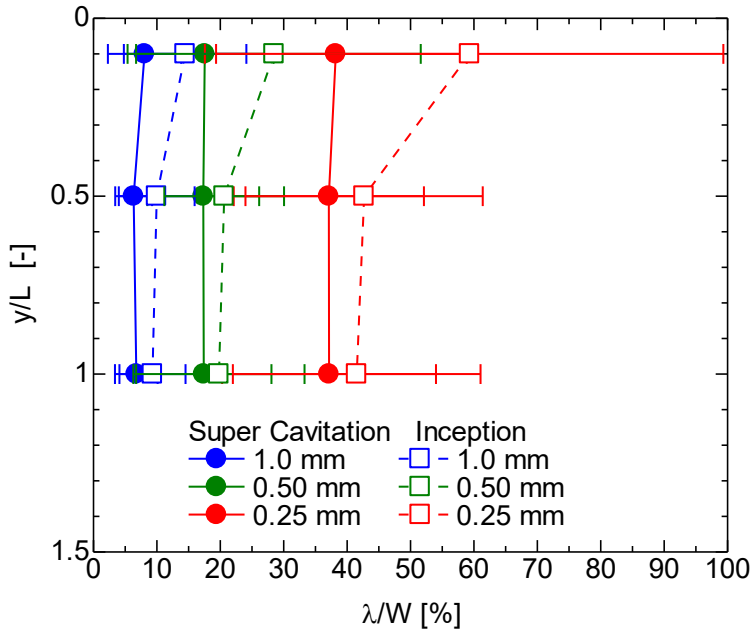

Figure 43 Normalized perturbation length scale λ/W of W = 1.0, 0.50, and 0.25 mm symmetrical nozzles

To investigate the effect of the difference in upstream geometry, λ of the discharged liquid jet from W = 1.0 mm symmetrical and mini-sac nozzles at inception, super cavitation, and hydraulic flip regimes is also compared. The comparison result is shown in Figure 44. For both kind of nozzles, it is clear that λ is shorter on super cavitation than at incipient cavitation, which is similar to the previous measurement result obtained with symmetrical nozzles with various sizes. Ligament formation at the liquid jet interface occurs more frequently and jet deformation is likely to be enhanced. However, as is evident from the liquid jet structure shown previously in Figure 37, at hydraulic flip regime, λ of the

symmetric nozzle is very large. For mini-sac nozzle, λ at hydraulic flip for the mini-sac nozzle is quite small, even comparable to λ at super cavitation regime.

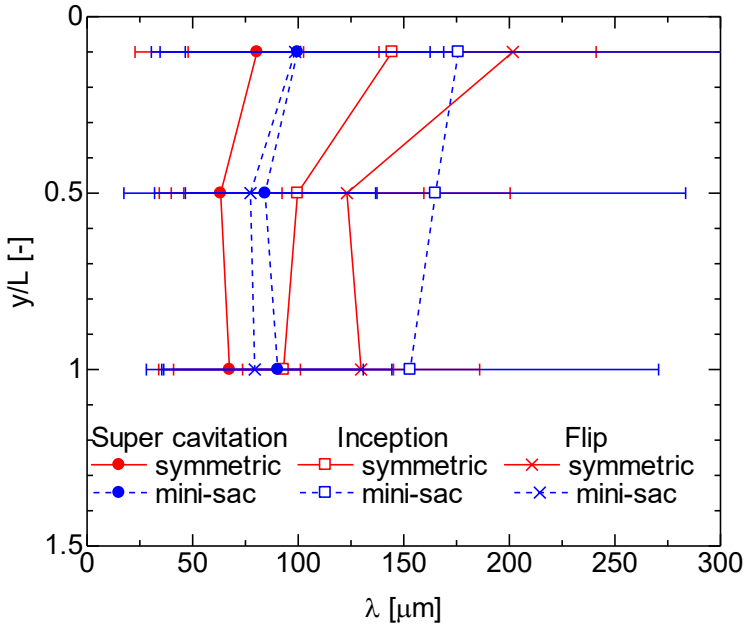

Figure 44 Comparison of measured perturbation length scale λ of symmetrical and mini-sac nozzles (W = 1.0 mm)

2.4 Summary

XPCI experiment of 2D nozzles with various sizes and upstream geometry was carried out to investigate the size similarity law of in-nozzle cavitation, as well as its effect on the discharged liquid jet. XPCI makes it possible to visualize individual bubble in a cavitation cloud and the structure of the wavy liquid jet clearly. From the observation results, the following conclusions were obtained:

1. In-nozzle cavitation first occurs in the nozzle as a cloud of individual cavitation bubbles under low flow velocity. These bubbles are not spherical, with a highly distorted circumference. Most bubbles near the edge of the recirculation flow are slanted, as a result of the recirculation flow in the nozzle. As flow velocity increases, the cavitation cloud bubbles turn into a single cavitation film.
2. Cavitation bubble size tends to change along with the change in nozzle size, as the bubble size strongly depends on turbulent eddy scale in the nozzle.
3. A perturbation length scale λ was introduced to evaluate the structure of the gas-liquid interface of the wavy liquid jet core. It was found that λ is smaller at the super cavitation regime, which is caused by cavitation-induced turbulence near the nozzle exit.
4. The normalized perturbation length scale λ/W shows that jet deformation is suppressed with the decrease in nozzle size
5. Perturbation of cavitation film is greater at mini-sac nozzle compared to symmetric nozzle. This was likely caused by stronger turbulence resulting from the asymmetric inflow from the upstream of the mini-sac nozzle.

6. At the hydraulic flip regime, λ of the mini-sac nozzle is very small, comparable to the λ at super cavitation regime. This is caused by the flow reattachment in the nozzle, which still occurs periodically in the mini-sac nozzle, even at the hydraulic flip regime.

3 X-RAY HIGH-SPEED IMAGING OF CAVITATION IN NOZZLES AND DISCHARGED LIQUID JET

3.1 Applicability of steady state injection data for transient injection process

Studies of internal flow and discharged liquid jet from a nozzle are sometimes carried out under steady injection process. Although steady injection data can be helpful for the study of internal flow in the nozzle, fuel injection is carried out under transient injection scheme, which makes in-nozzle cavitation phenomena to have a transient characteristic. This difference raises some questions regarding the applicability of steady injection data to transient injection process. In this chapter, high-speed visualization of cavitation in a rectangular plain-orifice nozzle and discharged liquid jet was carried out under steady and transient injection condition, in order to examine the applicability of steady injection data to transient injection process. The cavitation length and discharged liquid jet angle data from the transient injection is used to investigate transient cavitation development in the macro scale, while x-ray phase contrast imaging of in-nozzle cavitation was carried out to clarify the morphology of cavitation inception in the micro scale. In addition, to investigate the effect of turbulence in nozzle with different sizes, XPCI was also carried out to in-nozzle cavitation under steady injection condition.

3.2 Methodology

3.2.1 Experimental setup of visible light high-speed imaging

Experimental setup for the visible light experiments of steady and transient injection is shown in Figure 45. A pressure vessel that was filled with filtered tap water was connected through a solenoid valve (CKD, FWB31-6-3-02C) to the nozzle. The pressure of the vessel was kept constant with a regulator-equipped nitrogen tank. When the valve was opened, the water was discharged through the nozzle into ambient air. At the same time, pressure in the vessel P_t and that at the upstream of the nozzle P_i were recorded with pressure sensors (Kyowa, PGMC-A-1MP), while high-speed images of in-nozzle cavitation and the discharged liquid jet were captured with a high-speed camera (Photron, SA-Z; fitted with Nikon, 200mm f/4 AF-D lens) and a metal halide lamp (Kyowa, MID-25FC). To synchronize the timing between the valve opening, the image recording, and the pressure data acquisition, a microcontroller (Arduino, Uno Rev.3) was used. First, the microcontroller sent the signal to open the valve, which caused water to flow through the nozzle. At the same time, trigger signals were sent to the pressure sensors' data logger (Kyowa, EDX-10A, equipped with EDX-11A strain measuring unit and EDX-12A voltage measuring unit) and the high-speed camera to begin pressure data acquisition and image process, respectively. The exact moment when the trigger signals were being sent from the microcontroller is defined as t = 0 ms. As the sudden influx of flow naturally caused an overshoot in P_i, for the steady injection experiment, only the images after P_i stabilized (t > 300 ms) were used for the experiment. Conversely, the images for transient injection analysis were captured for t = 0-300 ms time range. Image processing was carried out on the

captured images to measure the normalized cavitation length L_c/L and average jet angle θ in steady and transient injections. The definitions of L_c, L, and θ are shown in Figure 46.

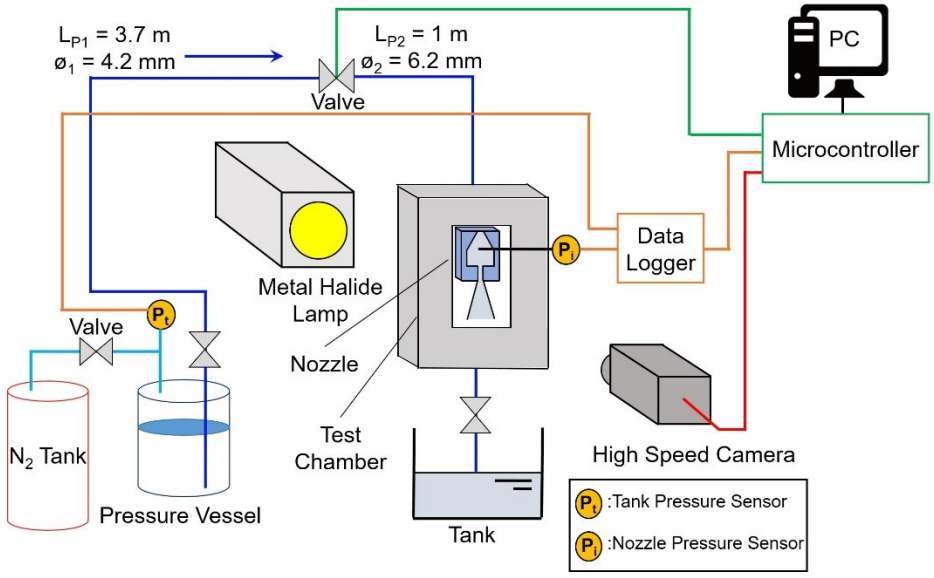

Figure 45 Visible lights experimental setup

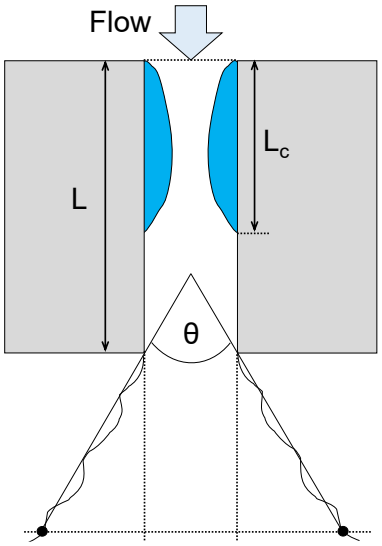

Figure 46 Definitions of L, L_c, and θ

Detailed experimental conditions for the visible light high-speed imaging experiments are shown in Table 4. P_t and P_i were both given as absolute pressure. The steady injection experiment was carried out at various P_t to simulate various cavitation regimes. For transient injection experiment, fluctuation in P_i induces the fluctuation of cavitation length L_c. Should L_c extends past the nozzle exit, the surrounding gas can enter the nozzle, which will cause hydraulic flip to occur. In this case, cavitation regime in the nozzle will not change even when P_i has stabilized. In other words, excessive P_i overshoot will invariably cause an irreversible hydraulic flip in the nozzle. To prevent this, P_i for transient injection experiment was set up so that the P_i at which hydraulic flip occurs was not exceeded. The threshold of this P_i value was determined to be 288 kPa, which corresponds to a

P_t of approximately 340 kPa. Because of this, the P_t for transient injection was set to 330 kPa. The Reynolds numbers of the flows under cavitating conditions are approximately 12000 – 20000.

Table 4 Visible light high-speed imaging experimental setup

	Tank Pressure P_t [kPa]	Injection Pressure P_i [kPa]	Shooting Speed [fps]
Steady Injection	200	168	24
	210	175	
	220	183	
	230	191	
	240	198	
	250	206	
	260	214	
	270	221	
	280	229	
	290	236	
	300	244	
	310	252	
	320	260	
	330	267	
	340	288	
Transient Injection	330	Varies with time	20000

3.2.2 Experimental setup of X-ray high-speed imaging

The experimental setup for the transient injection XPCI experiment is shown in Figure 47. The setup is essentially similar to the visible light experimental setup, with several modifications adapted to suit SPring-8's installation. For the XPCI experiment, the high-speed camera was fitted with an objective lens (Mitutoyo M plan APO 10x, 0.28 NA). The high heat flux of the x-ray beam made it impossible to carry out a continuous image acquisition for an extended period of time, as the heat load at the nozzle and the optics would be too high. To reduce the heat load, the generated x-ray beam was passed to the nozzle only at the instant of the imaging, using a pair of optical choppers. The timing of chopper opening was synchronized with the high-speed camera trigger by a digital pulse generator (SRS, DG535). Thus, for the XPCI experiment, the microcontroller served as the trigger for the digital pulse generator instead of the high-speed camera. The heat load limited a single instance of image acquisition to 3 ms duration. As the P_i took about 108 ms to reach its peak in the XPCI experiment, a different image acquisition scheme (Figure 48) was used for the XPCI to capture the full range of images during the pressure overshoot. High-speed images of 36 individual shots were taken at different times after the start of injection. A delay of 3 ms was added to the timing of valve trigger signal after each injection so that the valve open timing in the 36^{th} injection occurred 105 ms slower than the 1^{st} injection.

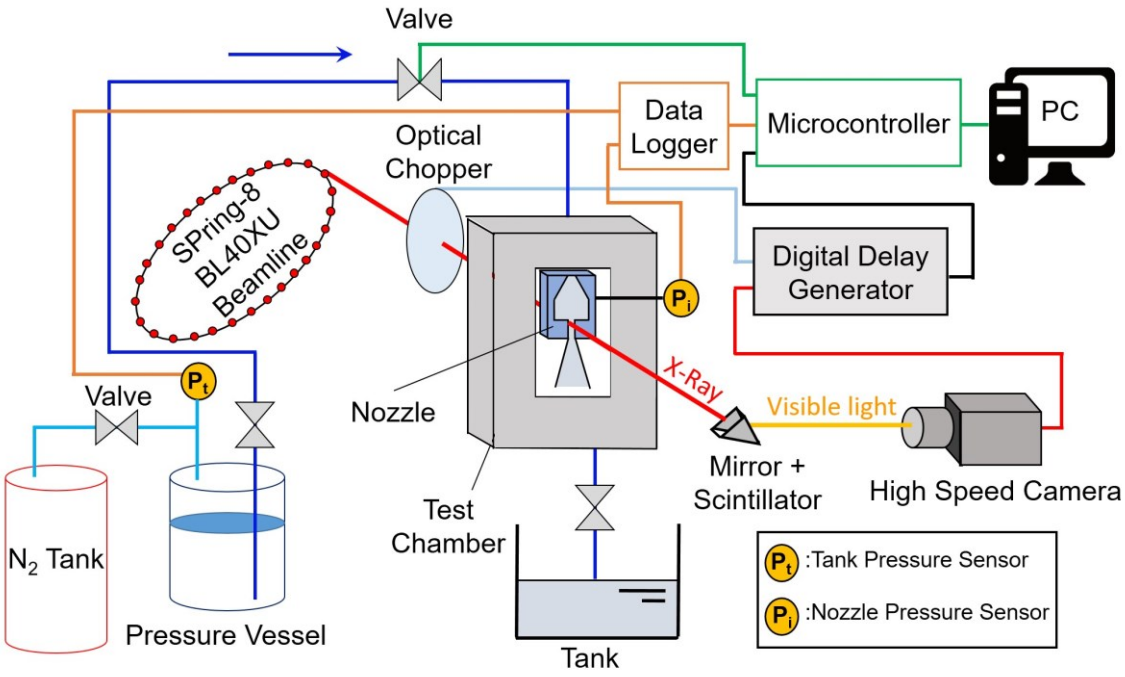

Figure 47 Transient injection XPCI experimental setup

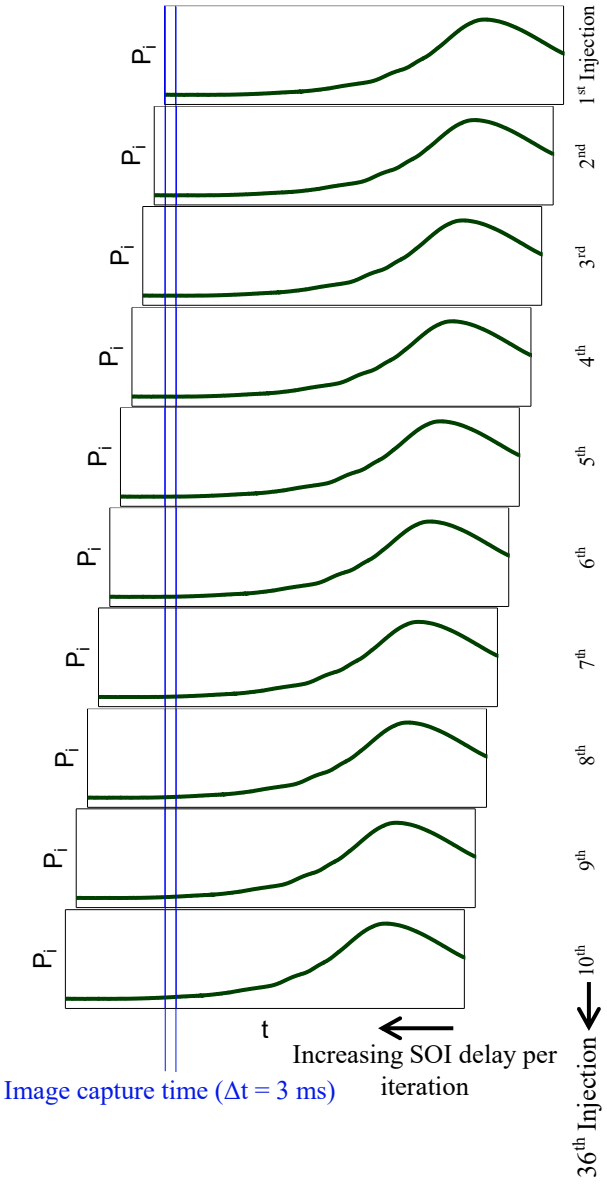

Figure 48 Injection scheme for the transient injection XPCI

The experimental setup of steady injection XPCI is shown in Figure 49. As the injection was conducted under steady injection condition, a complicated injection scheme was not needed. This setup is similar to the XPCI still-imaging setup shown in the previous chapter (Figure 29), with a high-speed camera in place of the CCD camera, as well as different scintillator to suit the high-speed camera sensor and the C-mode filling pattern of the SPring-8 used for the high speed imaging.

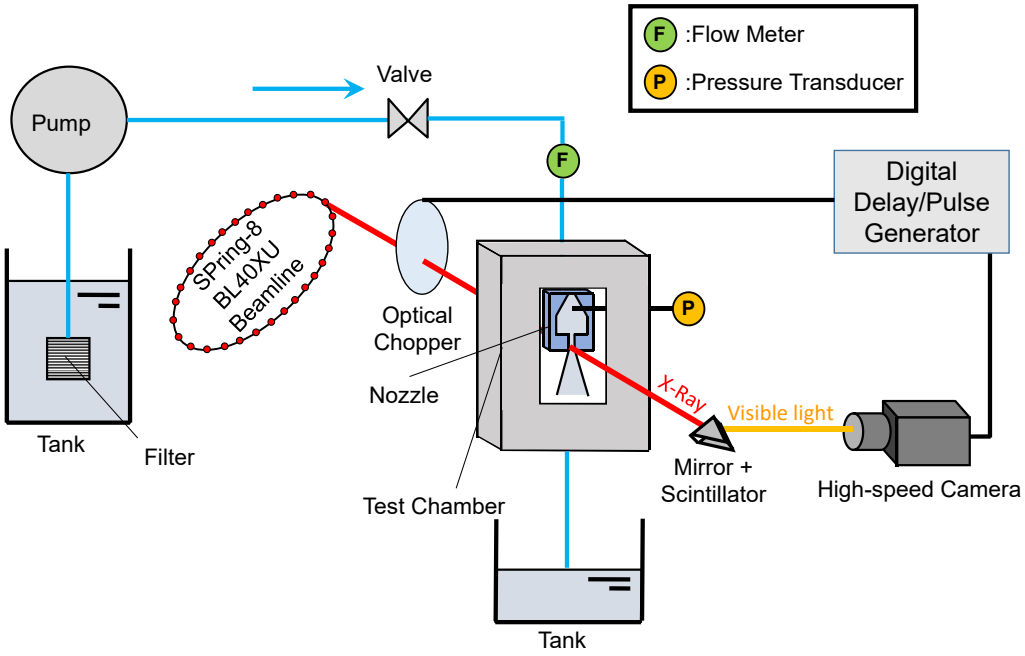

Figure 49 Steady injection XPCI experimental setup

Imaging was carried out with a beam energy of 12 keV, with a photon flux of 1 x 10^{15} photons/sec downstream of the focusing mirrors. To minimize photon flux loss, vacuum or helium path was used to guide the beam to the experimental hutch. The beam was exposed to the air in the test chamber and the space between the test chamber and the scintillator, whose total path was about 0.5 m. Based on a simple absorption analysis, the photon flux loss by the nozzle and the air was ca. 8%. Imaging area size was about 0.49 mm x 0.54 mm, with a spatial resolution of 2.1 μm / pixel and an exposure time of 0.347 μs. Two bunches from the SPring-8's C-mode filling pattern (29 bunches x 11 train pulse, 165.2 ns period, refer to Figure 50) were used in this study. A LuAg:Ce scintillator crystal (100 μm in thickness) was used to convert x-ray beam into visible light (wavelength peak = 535 nm), which was then reflected by 45° mirror and captured by the high-speed camera. Although LuAg:Ce scintillator has a drawback for time-resolved studies as a result of its long emission decay time, its emission spectrum was the most closely matched with the high-speed camera used in the current study [142]. This made it possible to capture images with better intensity compared to images captured using other commercially available scintillators. Additionally, the emission decay of LuAg:Ce occurs in the sub-μs time order [143], while cavitation bubble develops in the order of μm/μs. Therefore, the long emission decay is negligible in the current study.

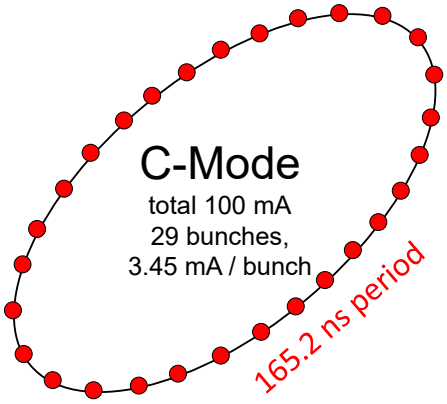

Figure 50 C-Mode filling pattern of SPring-8

Filtered tap water was used as the working liquid for the experiments. Nitrogen was used to elevate the pressure vessel, which makes it possible for dissolved gas to be distributed homogeneously in the water. Because of this, the timing of cavitation inception might be affected by the dissolved gas, in accordance with the Henry's law of dissolved gas in liquid. Under cavitating condition in the nozzle, it is possible for the non-condensable gas molecules to expand and come out from the liquid as bubbles. Although it is hard to differentiate cavitation vapor from expanded non-condensable gas, an XPCI study by Duke et al. [116] found that bubbles resulting from the expansion of non-condensable gas have disproportionately large sizes. This is likely caused by the fact that the internal pressure of non-condensable gas bubble is higher than the vapor pressure of the liquid. The high internal pressure also made it possible for the bubbles to travel outside the recirculation flow area, where the liquid pressure is high, and maintained their shape. In addition, a recent x-ray radiography study [115] and x-ray fluorescence spectroscopy [118] found that one of the key difference between cavitation in degassed and non-degassed fluid is the resulting distribution of vapor region in the nozzle. With non-degassed fluid, vapor region is not only confined to the recirculation area near the wall but also found in the middle of the nozzle. As both phenomena were not observed, cavitation inception in the current study is more likely to be triggered by trapped bubble nuclei in the nozzle wall or by a microbubble that traveled to the recirculation area near the wall.

3.2.3 Nozzle schematics

All experiments were carried out with 2D nozzles. Schematics the nozzles are shown in Figure 51. For the visible light experiment, the nozzle was created from acrylic plates that were molded into a nozzle-shaped recess. For the XPCI experiment, the nozzle was created from an aluminum plate, which was tightened between two acrylic plates. The surface roughness of the nozzles were controlled within 0.8–1.6 Ra. Detailed nozzle specifications are available in Table 5.

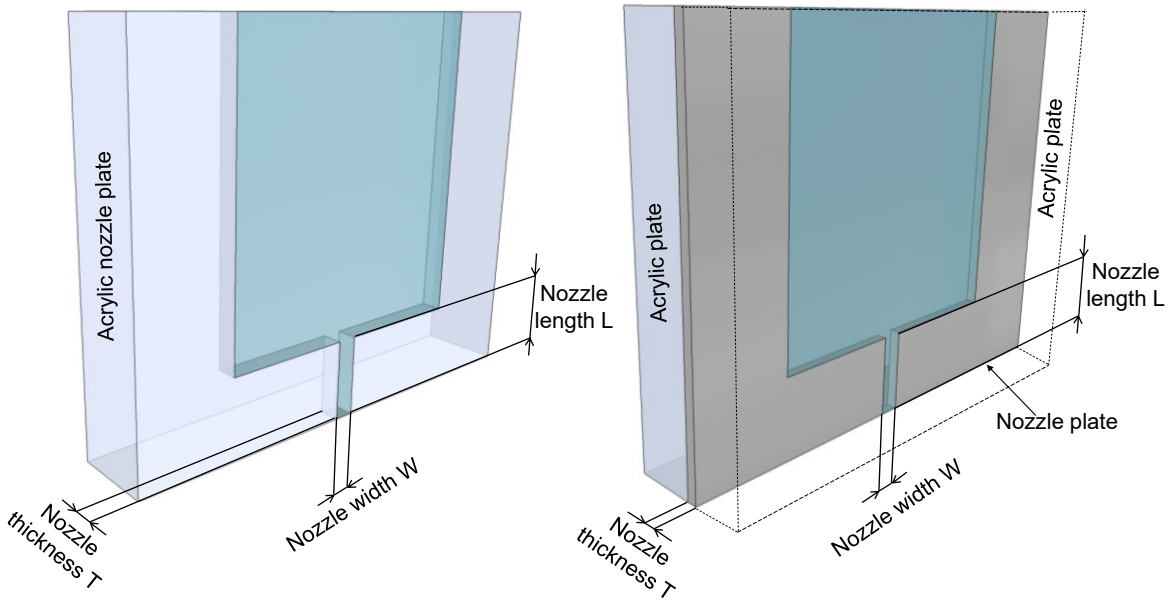

(a) Nozzle for visible light experiments (b) Nozzle for XPCI experiments

Figure 51 Nozzle schematics for the high-speed imaging

Table 5 Detailed nozzle specifications

Light source	Injection condition	Nozzle length L	Nozzle width W [mm]	L/W [-]	Nozzle inlet roundness R [μm]	R/W [%]	Nozzle thickness T [mm]	Nozzle material
visible light	transient	4.0	1.0	4	20.0	2.0	1.0	Acrylic
	steady							
x-ray	transient	4.0	1.0		22.6	2.3	0.5	Aluminum
	steady	8.0	2.0		20.0	1.0	1.0	Stainless steel
		4.0	1.0		22.6	2.3	0.5	Aluminum
		2.0	0.50		31.2	6.2	0.5	

3.3 Results and Discussion

3.3.1 Visible light experiment under steady injection condition

Representative images of in-nozzle cavitation and the discharged liquid jet from the steady injection experiment are shown in Figure 52. Mean flow velocity in the nozzle V increases along with the increase in P_i. In turn, L_c also increases following the in-nozzle cavitation regime characterization as defined by Sou et al. [97]. Besides the increase in L_c, increasing θ can also be observed in Figure 52. Reattachment point of the separated flow to the wall, which is located at the tail end of cavitation film, will get closer to the nozzle exit as L_c increases. Liquid jet deformation by cavitation mainly occurs as the result of the radial flow reattachment of the separated flow as well as the vortex flow structure shed from the reattachment point. When the reattachment point is very close to the nozzle exit (i.e. at the super cavitation regime), the increase in θ is also very large. This enhancement of liquid jet deformation by cavitation occurrence in the nozzle is well-documented in various studies [81], [82], [97], [99].

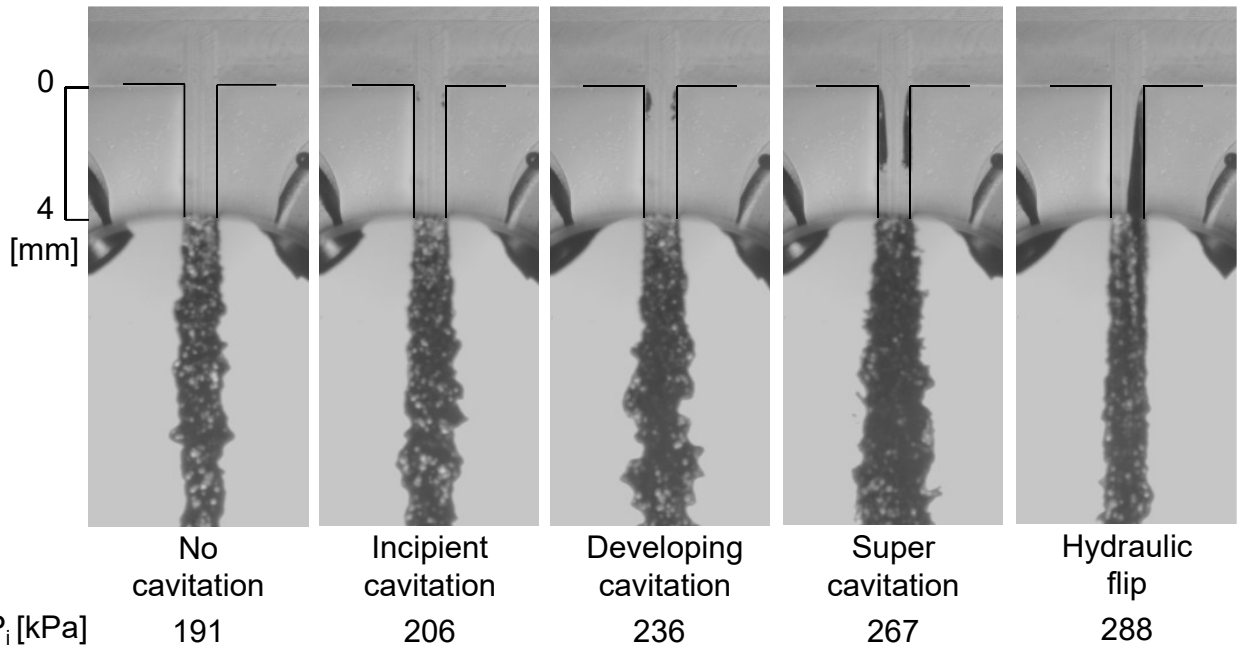

Figure 52 Representative images of in-nozzle cavitation and liquid jet under visible light (steady injection)

As P_i is increased further, eventually hydraulic flip occurs. At this regime, the cavitation film extends past the nozzle exit, which made it possible for surrounding gas to enter the nozzle. Because of this, there is no reattachment to the nozzle wall, and the liquid jet enhancement mechanism explained previously cannot occur. As a result, θ is decreased at the hydraulic flip regime.

Measurements of L_c and θ were carried out using image analysis on the captured steady injection images. To do this, the captured greyscale images were first binarized using Otsu's method [144] to determine the binarization threshold. The resulting images will have black pixels for cavitation and liquid jet region. To measure L_c, the resulting black pixel inside the nozzle is then counted and divided by the pixel count of the nozzle length L, which gives the value of normalized cavitation length L_c/L. The jet angle θ was measured at the distance of 1L from the nozzle exit. θ was calculated from the inverse tangent of the horizontal pixel count of the jet at 1L, divided by the pixel count of the nozzle length. The measurement results are shown in Figure 53 and 54.

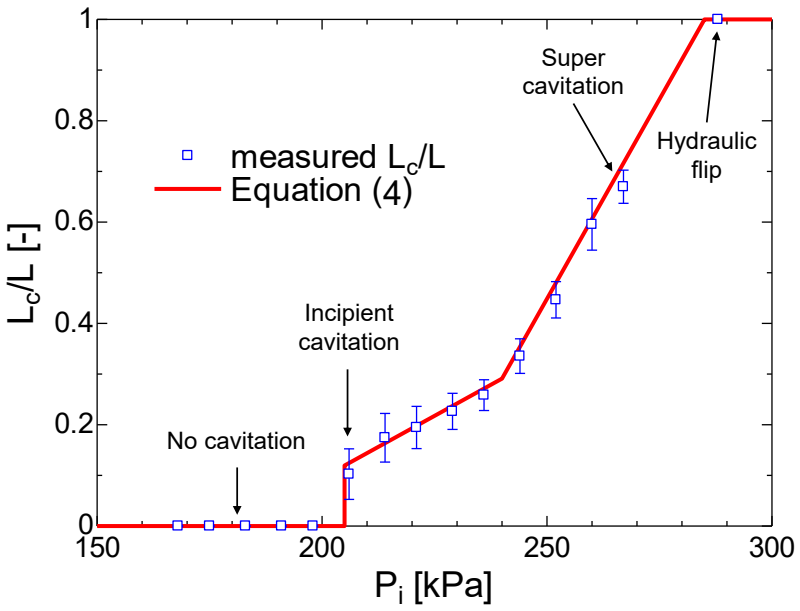

Figure 53 Comparison between measured L_c/L from steady injection and predicted L_c/L from Equation (4)

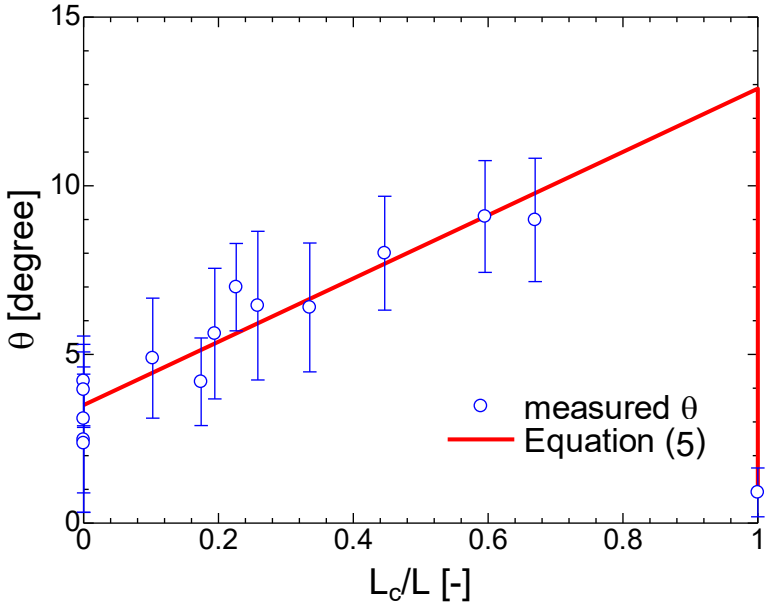

Figure 54 Comparison between measured θ from steady injection and predicted θ from Equation (5)

From the measurement result, two correlation equations were created. The first equation predicts L_c/L as a function of P_i, while the second equation predicts θ as a function of L_c/L. The equations are given as follows:

$$\frac{L_c}{L}(P_i) = \begin{cases} 0, & P_i < 205\text{kPa} \\ 0.0049P_i - 0.885, & 205\text{kPa} \le P_i < 240\text{kPa} \\ 0.0145P_i - 3.195, & 240\text{kPa} \le P_i < 285\text{kPa} \\ 1, & 285\text{kPa} \le P_i \end{cases} \tag{4}$$

$$\text{For } \frac{L_c}{L} > 0,\ \theta\left(\frac{L_c}{L}\right) = \begin{cases} 9.38\frac{L_c}{L} + 3.5, & \frac{L_c}{L} < 1 \\ 0.9, & \frac{L_c}{L} = 1 \end{cases} \tag{5}$$

Although deformation of discharged liquid jet and the resulting jet angle can be affected by several factors, the current study focuses only on the effect of cavitation on the discharged liquid jet. Thus, Equation (5) can only reveal the changes brought by cavitation in the nozzle to the resulting θ. Similarly, although we acknowledge that cavitation occurrence in the nozzle is affected by various factors, only the effect of pressure drop was taken into account for the current study. This is also reflected in Equation (4). Note that both Equations (4) and (5) can only be applied for enlarged, rectangular plain-orifice nozzles. The comparison between both correlation equations and the measured experimental results are shown in Figure 53 and 53 for L_c/L and θ, respectively. It is evident that both correlation equations agree fairly well with the experimental results. In the next section, both equations' applicability to transient injection process will be examined.

3.3.2 Visible light experiment under transient injection condition

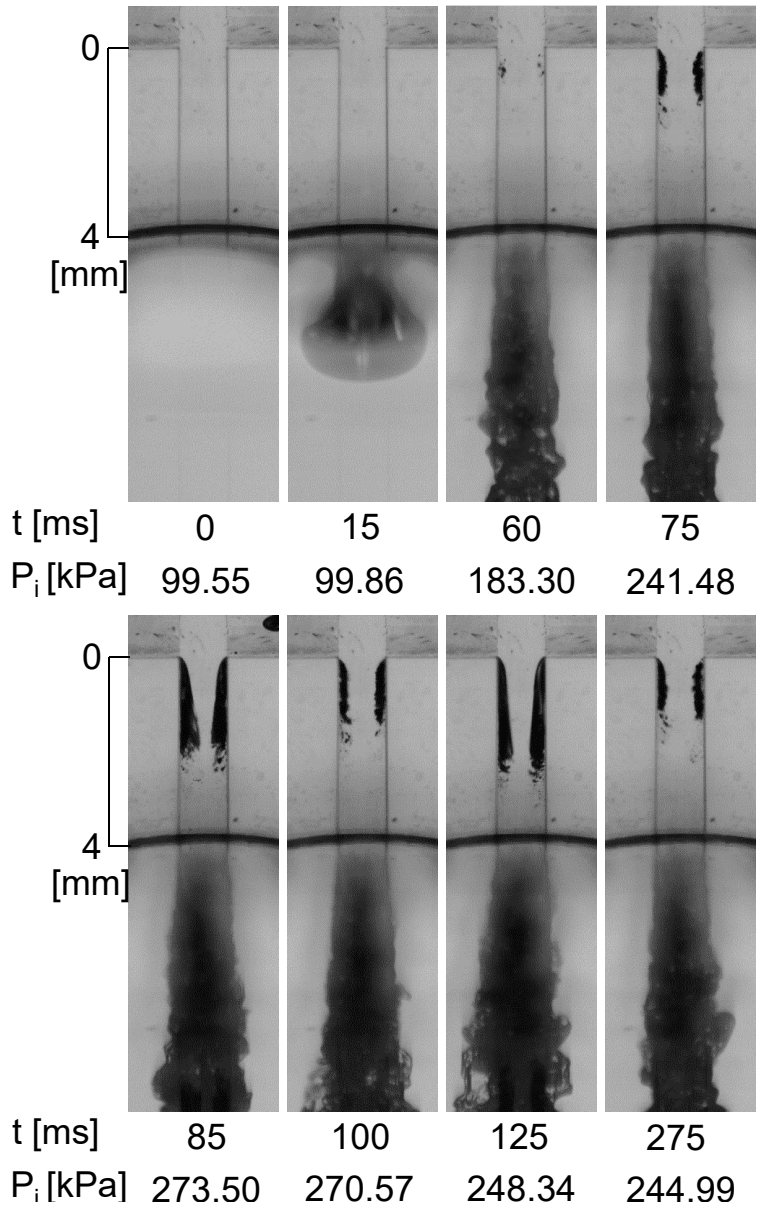

Figure 55 Representative images of in-nozzle cavitation and liquid jet under visible light (transient injection)

Representative images of in-nozzle cavitation and discharged liquid jet from the transient injection experiment are shown in Figure 55. It can be seen that L_c and θ varies in accordance with the changes in P_i. When the signal to open the valve is being sent (t = 0 ms), liquid will rush in through the nozzle. This sudden rush caused an overshoot in P_i, followed by a drop before after which a stable P_i is reached. This is also reflected in Figure 55, which shows a momentary growth in L_c and θ before a stable value is observed. For the transient experiment, the peak of P_i appears at t ≈ 100 ms, with P_i completely stabilizes at t > 300 ms. Therefore, it can be concluded that the time to reach peak flow rate T_Q ≈ 100 ms in the current study, which is longer than the T_Q commonly found in real injectors. This is caused by both the low P_t and the large scale of the nozzle used in this study. For the current study, the data from t ≤ 300 ms is used for the transient injection analysis.

Similar to the steady injection analysis, measurements of L_c/L, and θ were carried out on the captured high-speed images, as well as P_i over time. Measured P_i, which are shown in Figure 56(a), reached its peak at ~270 kPa and stabilized after approximately 200 ms at Pi ≈ 250 kPa. The measured P_i are used in conjunction with Equation (4) to obtain the predicted L_c/L value. The predicted L_c/L value from Equation (4) is then used with Equation (5) to obtain predicted θ value. Lastly, the predicted L_c/L and θ values are then compared with the measurement results to compare the validity of the steady-state correlation equations against transient injection data. The results are shown in Figure 56(b) and (c). Because of the inherently long T_Q of the current nozzle, the observation result might only be valid for slow injection process, where the duration of the flow rate increase is much longer than the time scale of flow development in the nozzle. This is evaluated by the injection time scale parameter τ, which is defined as:

$$\tau = \frac{T_Q}{T_F} \tag{6}$$

where T_F is the time needed for the separated boundary layer to be formed in the nozzle, which is approximated by the nozzle length divided by the mean flow velocity through the nozzle. Slow injection is defined as the injection where τ > 300. T_F = 0.3 ms for the nozzles used in this study, which gives the τ value of 375.

As evident from Figure 56(b), for slow injection, the measured L_c/L agrees fairly well with predicted L_c/L from Equation (4), which gives validity to the applicability of steady injection data of in-nozzle cavitation to transient injection process. At least, it can be expected that similar P_i will result in a similar growth of in-nozzle cavitation, whether the injection process is steady or transient. From Figure 56(c), it is also evident that the estimated θ from Equation (5) agrees well with measured θ, with a standard deviation of 20-30%, which is similar to the standard deviation of the measured θ of the steady injection experiment. This result shows that Equation (5) can fairly reflect how in-nozzle cavitation affects liquid jet deformation. From the comparison result of both equations, it is proved that the data obtained from the steady injection experiment are applicable to transient injection process. Again, it should be noted that this observation is only valid for the case where flow development in the nozzle is slow.

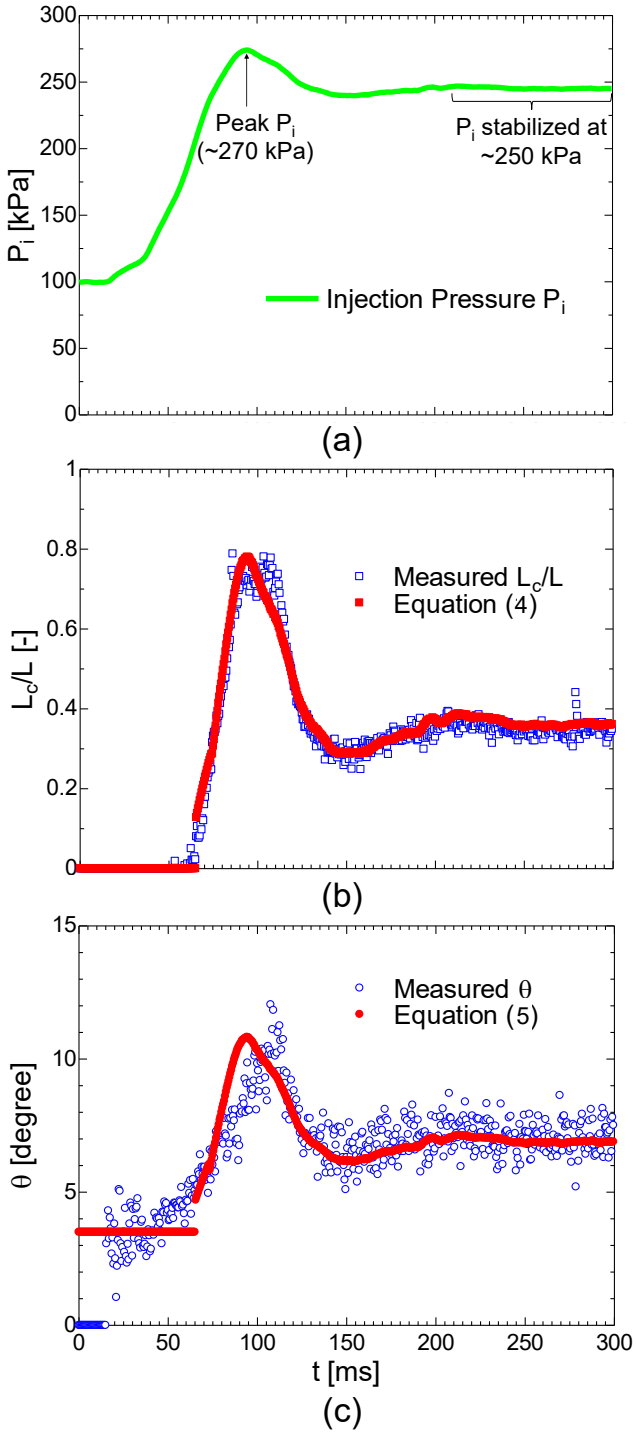

Figure 56 Comparison between measured L_c/L and θ from transient injection with Equation 4 and Equation 5

To examine the applicability of the current observation to real injectors, we also compared the experiment result with discharge rate data from a real solenoid injector of a low-duty passenger car diesel engine, whose rail pressure is 180 MPa [145]. Because discharge rate was not measured in the current experiment, time to reach peak P_i is used in place of T_Q, as explained previously. The T_Q of the real solenoid injector is ≈ 700 μs. The parameter T_{cav} (refer to Figure 57) is also introduced to approximate the transient cavitation development in enlarged and real nozzles. T_{cav}, which is derived from a simplified Rayleigh-Plesset Equation [37], is defined as the time required for a bubble nucleus

to reach its maximum radius, which is as large as the thickness of the boundary layer along the nozzle's side wall. Because the value of L and V of the solenoid injector is unknown, we approximate the value of L ≈ 0.5 mm and V ≈ 500 m/s. Using these approximated values, we can estimate the T_F and T_{cav} of the solenoid injector, which falls in the order of ~1 μs and ~0.01 μs, respectively. Similarly, the value of T_F and T_{cav}, which is calculated from the experimental data of the enlarged nozzle, falls in the range of ~300 μs and ~6 μs. This shows that the approximated values of T_Q, T_F, and T_{cav} scales in a similar order between real nozzles and the enlarged nozzle. This estimation might indicate that the internal flow condition scales between nozzle with different sizes. By extension, it could also indicate some similarity in cavitation development on nozzles with different sizes, although the lack of cavitation development data for the solenoid injector rules out a more detailed comparison between both nozzles. Even so, the similar time order might imply that the current approach of using steady injection data to predict transient cavitation development might also be applicable to real-scale fuel injectors in the case of high τ.

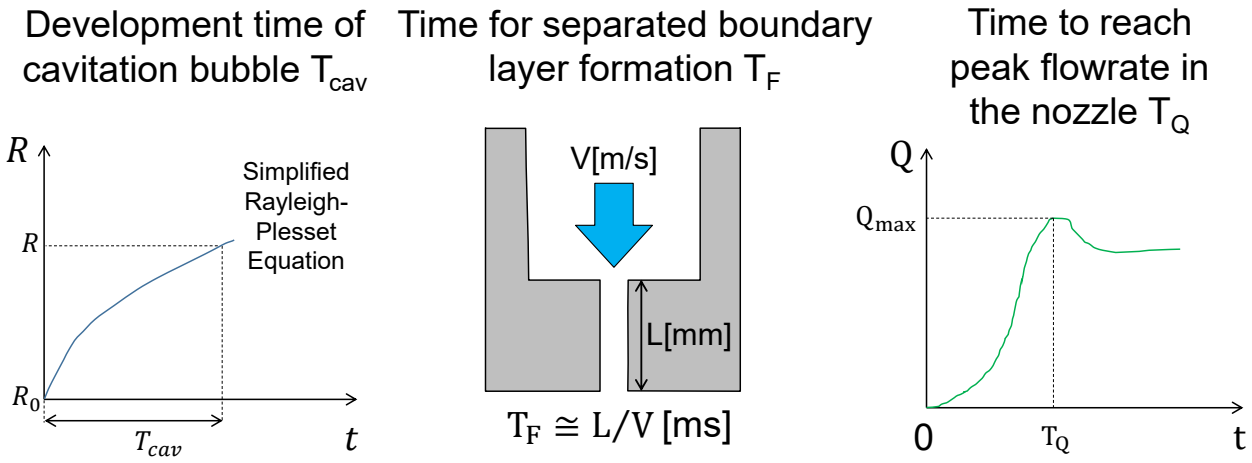

Figure 57 Definitions of T_Q, T_F, and T_{cav}

3.3.3 XPCI experiments under transient injection condition

This section explains the morphology of transient cavitation development, from a single bubble to the formation of cavitation film. Because of the limitation of chopper opening time, higher P_t is used to shorten the time needed until cavitation film develops in the nozzle, so that a complete cavitation development from a single bubble to a continuous film can be captured. Therefore, for the XPCI experiment, P_t is set to 500 kPa, which is higher than the P_t of visible light experiments. Measured P_i for transient injection XPCI experiment is shown in Figure 58, which shows that P_i starts to stabilize at $P_i \approx 500$ kPa, compared to P_i of visible light experiments during transient injection condition, which stabilized at $P_i \approx 300$ kPa.

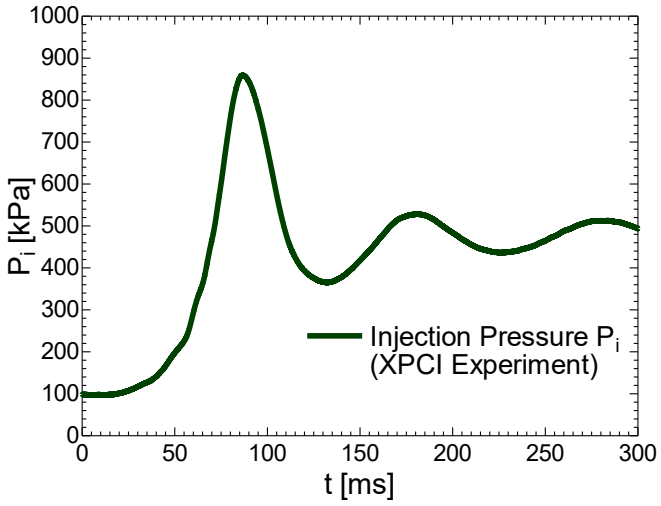

Figure 58 Injection pressure of the transient injection XPCI experiment

The overview of cavitation inception from a single bubble to cavitation film is shown in Figure 59. Imaging was carried out at the area near the nozzle inlet, as shown in the inset. A single cavitation bubble, which seems to result from heterogeneous nucleation from the wall, is first observed to come out from the nozzle wall at t = 57.575 ms, with P_i = 191 kPa. A fully-developed film seems to have developed at roughly t + 2.4 ms since the first cavitation bubble was observed, although the limitation of the imaging area made it difficult to understand the extent of cavitation growth downstream of the nozzle inlet. $P_i \approx 291$ kPa at t = 59.995 ms, which suggests that the cavitation has reached super cavitation or hydraulic flip regime. However, existing liquid/gas boundary near the nozzle wall at t = 59.995 ms likely means that hydraulic flip has not occurred yet.

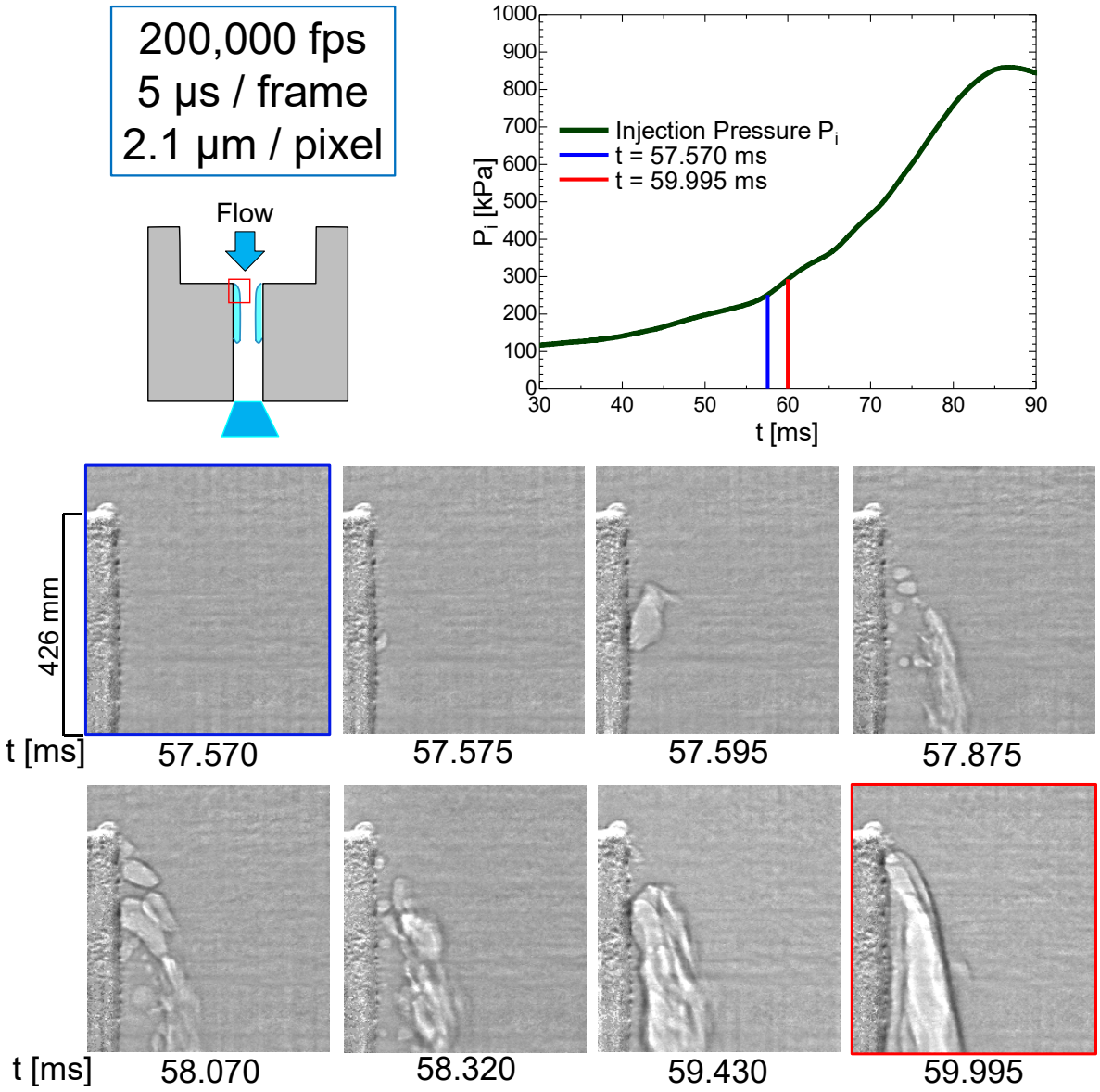

Figure 59 Representative images of cavitation development from single bubble to cavitation film under transient injection condition

The shape of the observed cavitation film somewhat agrees with the one observed by Duke et al [116] in a cylindrical nozzle with comparable geometry with the one used in this study (0.5 mm in diameter, 3.05 mm in length). However, their study showed a fully developed cavitation film 0.1 ms after the start of injection, which is much faster than the development time of cavitation film observed in the current study. This can be caused by the higher injection pressure (0.9 MPa) in Duke et al.'s study, which result in a higher pressure gradient in the nozzle and shorter cavitation development time. Another reason for longer cavitation development time might be the dissolved gas and the surface roughness of the nozzle which were controlled more carefully in the Duke et al.'s study. Because of this, heterogeneous nucleation is inhibited, even on conditions that allow for cavitation inception, i.e. high pressure drop in the nozzle. Thus, when cavitation inception starts to take place, it will instantly reach a more developed regime. Conversely, cavitation development in the current study occurs in a more gradual manner. A more detailed breakdown of in-nozzle cavitation

morphology starting from the nucleation of a single bubble to a large cavitation film formation is shown in Figure 60 below.

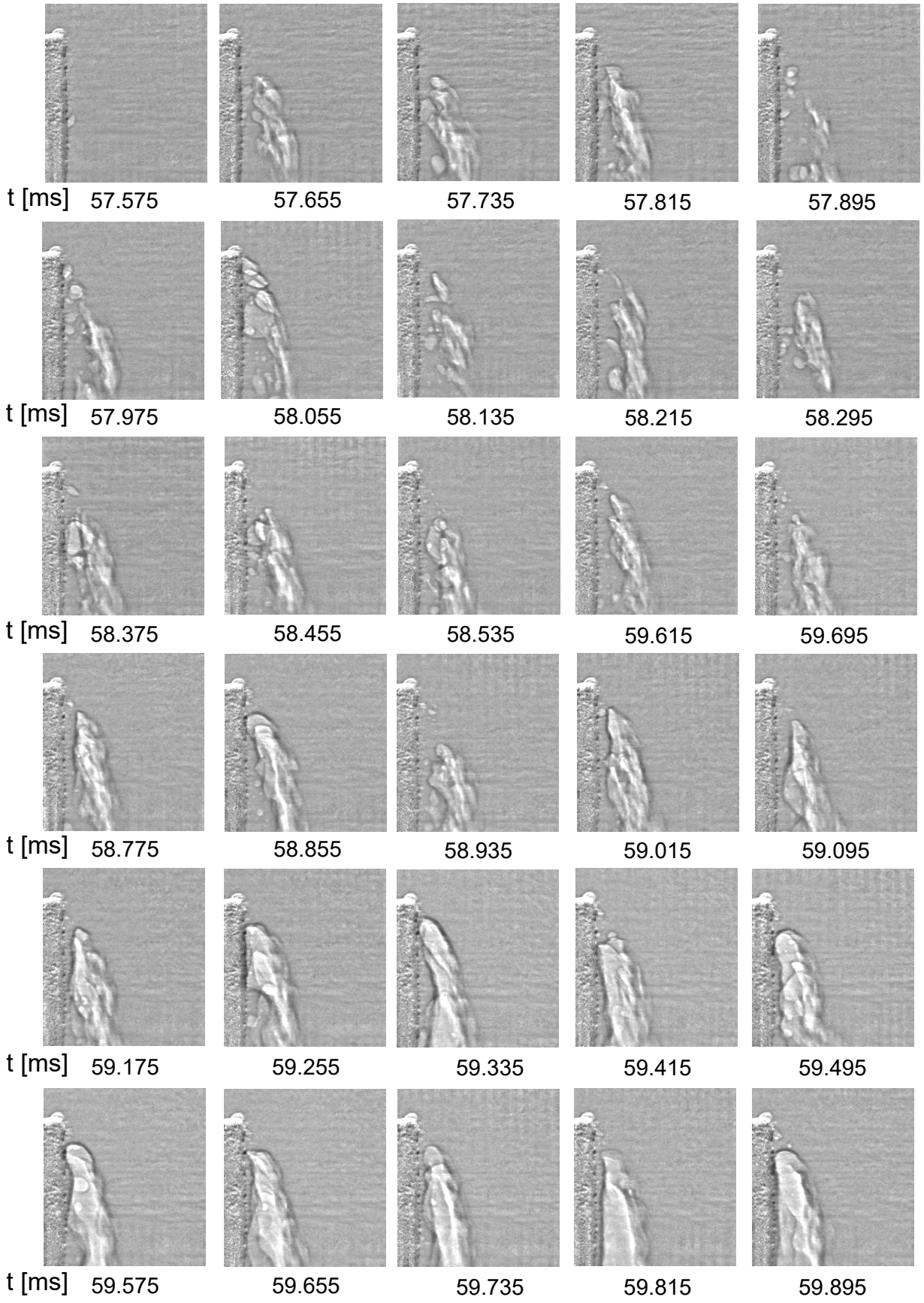

Figure 60 Detailed breakdown of cavitation development from single bubble to film formation

Several different events can be observed during the course of cavitation development. The first event is the heterogeneous nucleation of the initial bubble nucleus, which caused the bubble to grow. This initial bubble can be seen in Figure 61. As mentioned previously, this initial nucleus seems to be trapped in the nozzle wall, as a result of the rough surface area of the nozzle. Following the pressure drop in the vena contracta area, the nucleus expand and grows into a bubble. Additionally, because of the streamwise velocity profile of a nozzle illustrated in Figure 62 [97], the bubble begins to deform and collapses near the boundary, where the velocity is the largest in the nozzle and the pressure is higher compared to the area near the nozzle wall.

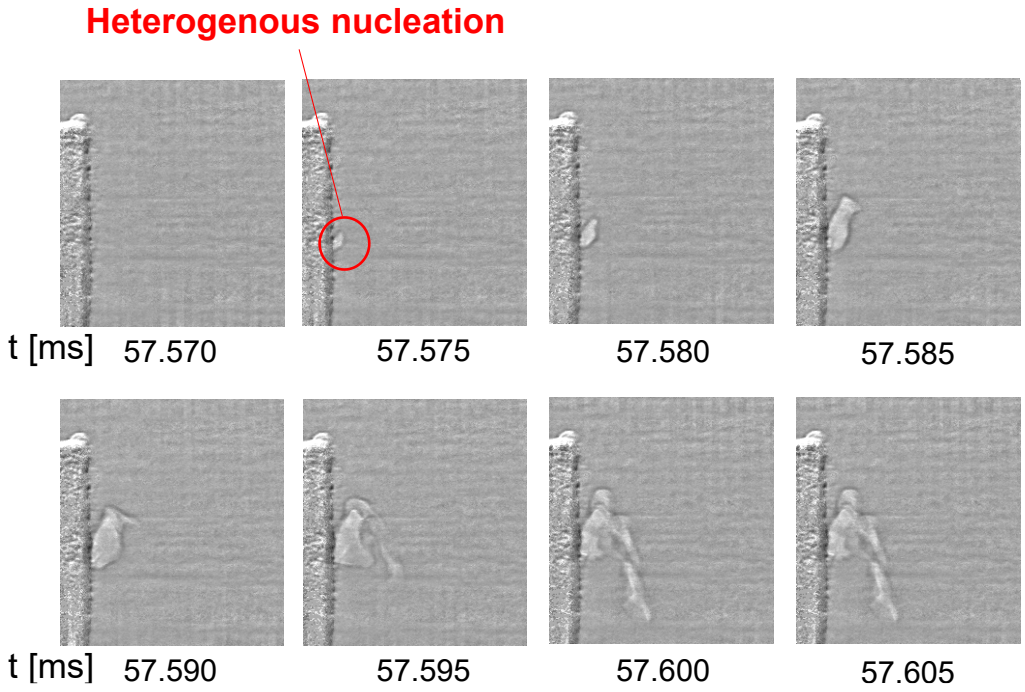

Figure 61 Nucleation process of the initial bubble nucleus

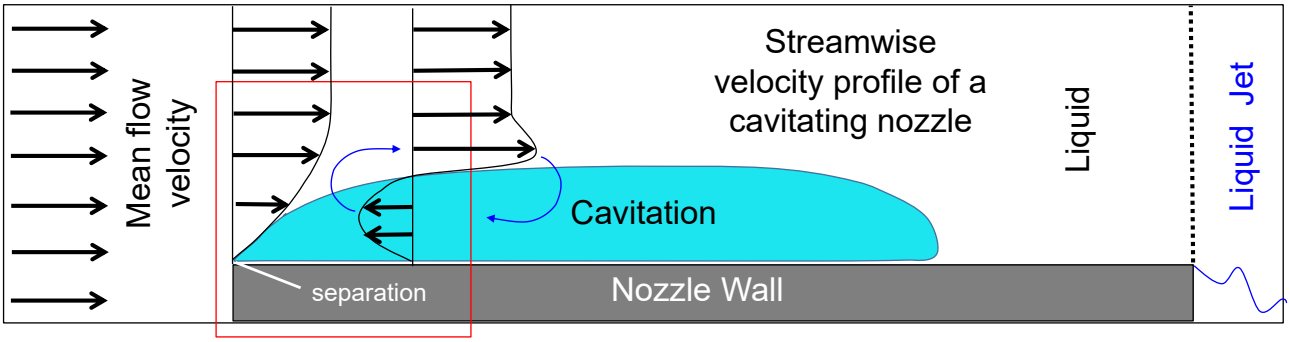

Figure 62 Streamwise velocity profile of a cavitating nozzle

The second event is the additional nucleation of other bubbles, as can be seen in Figure 63. These bubbles appear about 0.3 ms since the initial bubble was observed. All of the bubbles which appear later begins to deform and collapses near the boundary, where the velocity is the largest in the nozzle and the pressure is higher compared to the area near the nozzle wall. All of these bubbles follow a similar pattern of growth and collapse like the initial bubble, as can be seen in Figure 64. In

addition, Because of the turbulent flow structure in the nozzle, the bubbles' growth and collapse occur in a rotating motion, as can be seen in Figure 65.

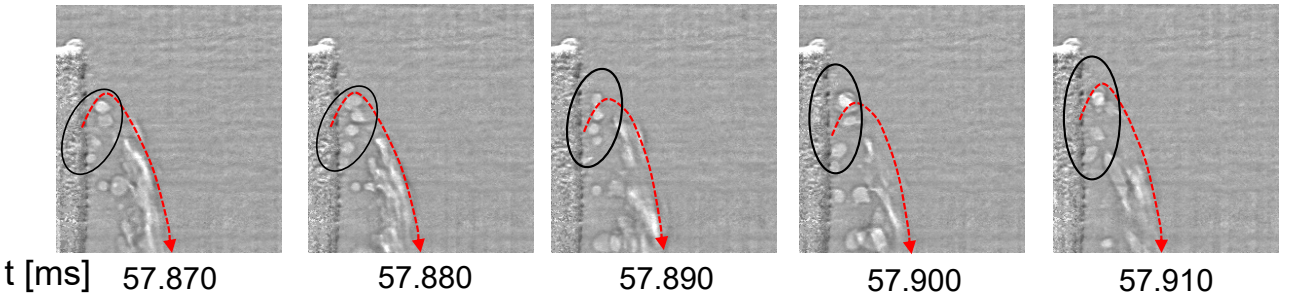

Figure 63 Additional bubble growth from the same nucleation site as the first bubble

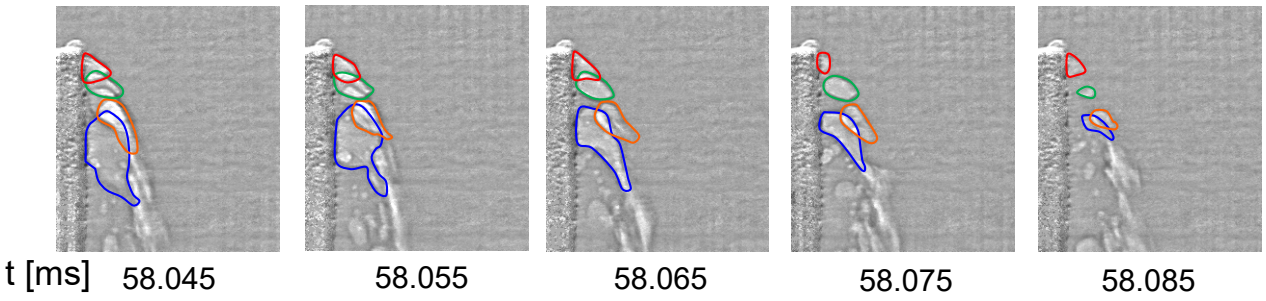

Figure 64 Bubbles collapsing over time

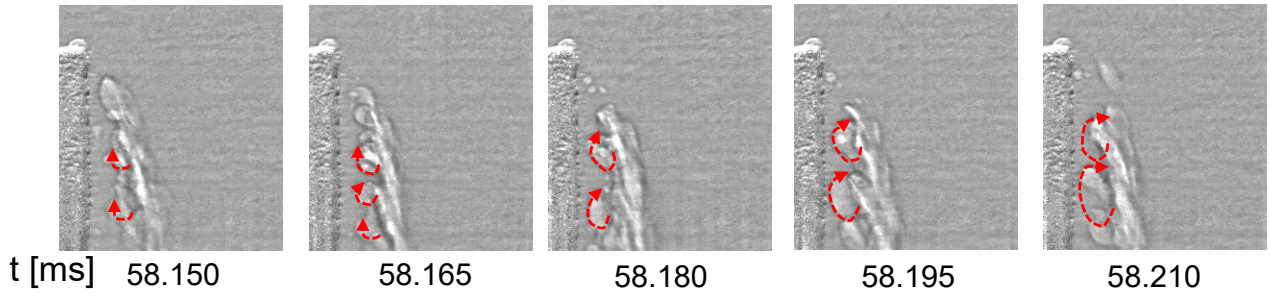

Figure 65 Rotating movement of the bubbles

As the mean pressure in the vena contract continues to drop, the achievable maximum radius of a bubble continues to increase. As a result, the bubbles will grow into several large-sized cavitation films. Eventually these films will combine and turn to a single cavitation film, as can be observed in Figure 66.

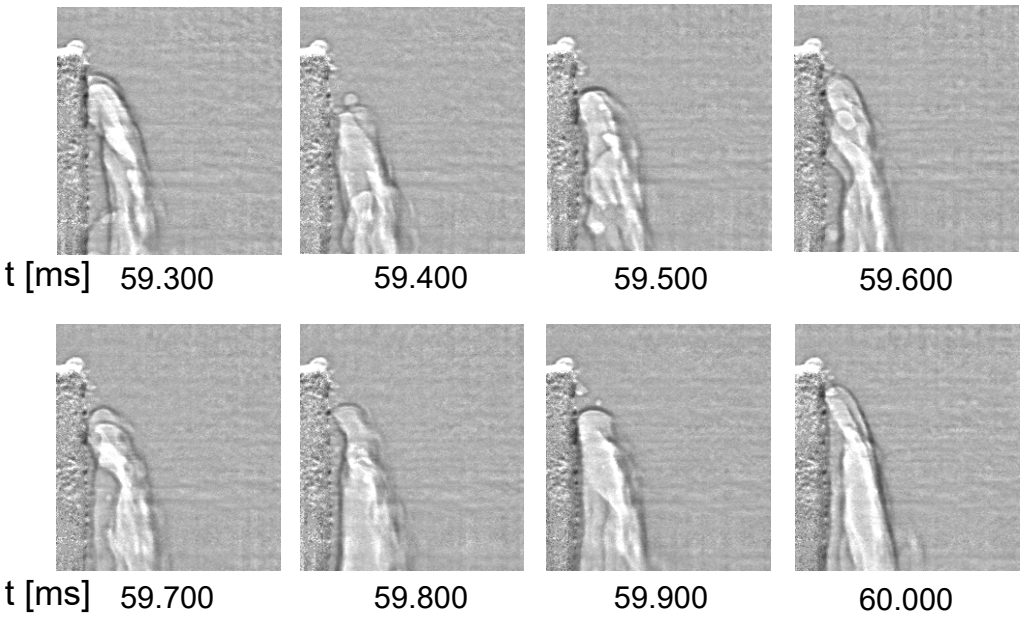

Figure 66 Formation of a single large cavitation film

Besides heterogeneous nucleation of a trapped microbubble from the nozzle surface, another pattern of cavitation inception in the nozzle was also observed during the XPCI experiment. Figure 67 shows cavitation inception induced by a bubble from upstream of the nozzle, which occurred in a different injection. The bubble initially appears at t = 54. 965 ms (P_i = 225.111 kPa). As it reaches the boundary of the velocity profile at t = 55.015 ms, the bubble begins to show a growth pattern similar to the one shown in Error! Reference source not found.. Although the limited imaging area p revented the observation of the exact moment of the initial bubble's breakdown, it is highly possible that several microbubbles whose size are smaller than the initial bubble are left over after the breakdown. These microbubbles serve as the nuclei for the next bubble growth reaction, which causes a chain reaction that leads to the development of incipient cavitation cloud, as shown in t = 55.040 – 55.190 ms. After the inception process has occurred, a similar pattern of cavitation development with the one triggered by heterogeneous nucleation of a bubble nucleus from the nozzle wall is observed. A fully developed cavitation film appears at approximately t + 1.8 ms since the initial upstream bubble was first observed.

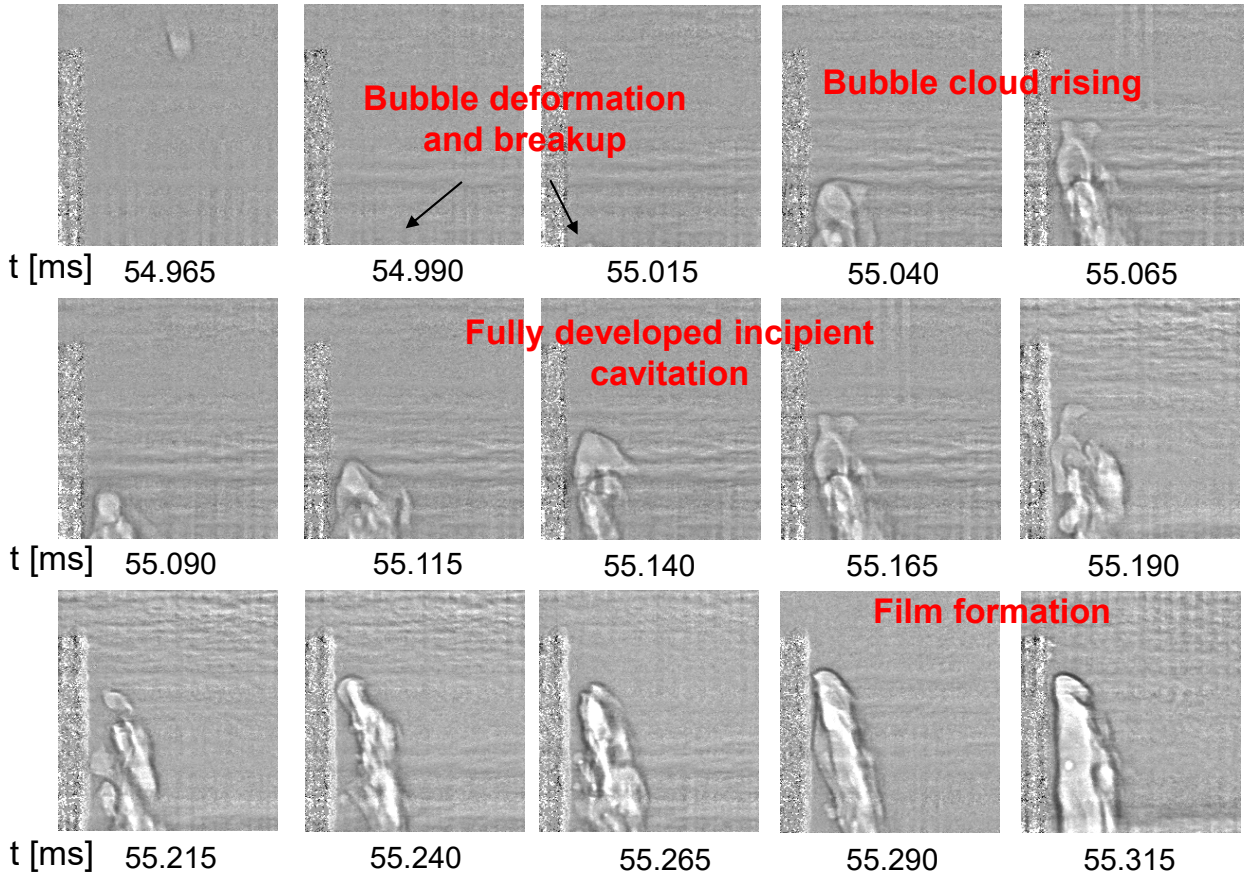

Figure 67 Cavitation inception by upstream bubble

3.3.4 XPCI experiments under steady injection condition

To investigate the effects of turbulence in nozzle to the development of cavitation bubbles, high-speed XPCI was also conducted in 2D nozzle with various sizes. Representative images of incipient cavitation under steady injection condition are shown in Figure 68. All images were taken near the nozzle inlet, with the position shown by a red rectangle in Figure 68. It was confirmed that almost all incipient cavitation bubbles have non-spherical shapes, as previously shown in Section 2.3.1. The bubbles tend to slant and elongate in the streamwise direction before they shrink and collapse. The slant and elongated shape of the bubbles is caused by the velocity profile of the recirculation flow, where the highest downward velocity appears near the outer edge of the boundary layer and an upward flow along the side wall. Counter-clockwise rotational motion of bubbles near the side wall of the nozzle can also be observed in Figure 68. The rotational motion is caused by the anti-clockwise eddies appearing along the outer edge of the boundary layer, near the reattachment point, and vortex shed from the point. These observations confirm that there is a strong relation between turbulent flow and cavitation in the nozzle.

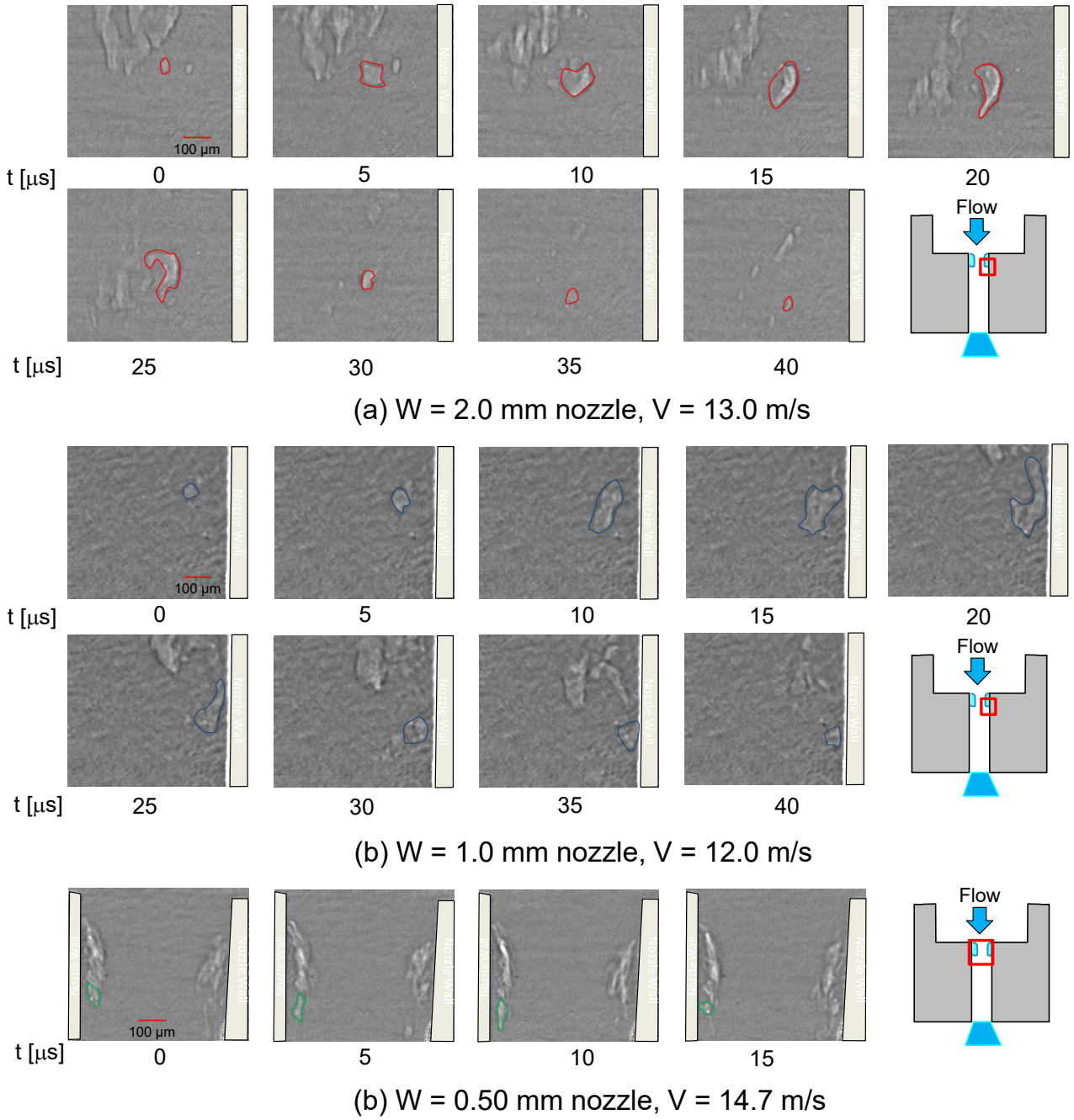

Figure 68 High-speed images of incipient cavitation under steady injection condition

To investigate the bubble growth and shrink process, equivalent diameter D_e of each cavitation bubble that was highlighted in Figure 68(a-c) was measured for each nozzle. D_e is given by Equation (3). The measurement result is shown in Figure 69.

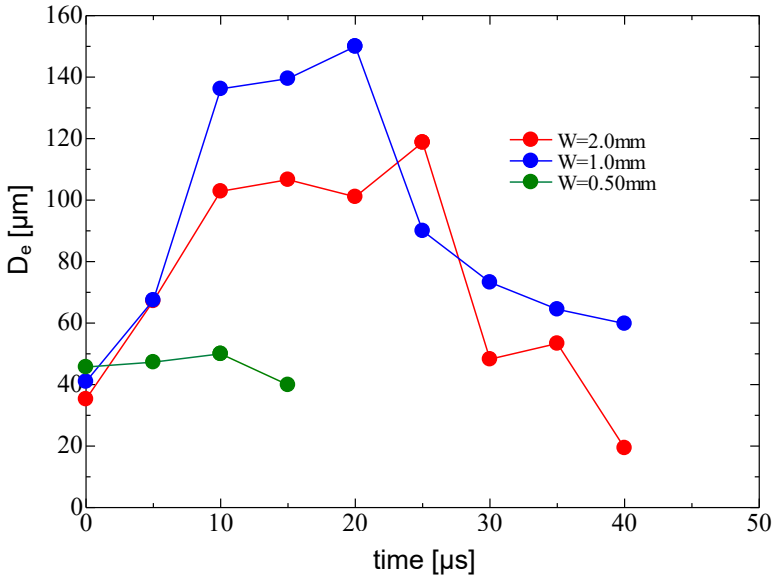

Figure 69 Time histories of equivalent bubble diameter D_e during growth and shrink process (steady injection condition)

Figure 69 shows the changes in incipient cavitation bubble size for each nozzles. The difference in bubble size for each nozzles are caused by the similarity law, that is, the diameters of incipient cavitation bubbles scales proportionally to the nozzle size. It should be noted that Figure 69 only serves to illustrate the growth and shrink process of a typical cavitation bubble in nozzles with different sizes. The maximum size of each bubbles shown in Figure 69 should not be taken as a representative bubble size. From Figure 69, it can be seen that while it takes about 10-20 μs for a bubble to grow, the shrink of a bubble happens within much shorter period, about 5μs. The time scale of the bubble growth and shrink process simply estimated by the Rayleigh-Plesset equation is much shorter from those observed in the present study, which suggests the fact that the process is governed by turbulent flow in the nozzle.

3.4 Summary

Visualization experiments of a rectangular plain-orifice nozzle under steady and transient injection condition were carried out to examine the applicability of steady injection data of in-nozzle cavitation and discharged liquid jet to the transient injection processes. Furthermore, XPCI was carried out to investigate the morphology of cavitation development in the nozzle. From the study, the following conclusions were obtained:

1. Correlations obtained from steady injection data can be used to predict the growth of in-nozzle cavitation and the discharged liquid jet angle during transient injection process where the duration of the flow rate increase is much longer than the time scale of flow development in the nozzle.
2. Cavitation inception process in the nozzle is caused by two kinds of heterogeneous nucleation, both of which governed by the turbulent flow structure in the nozzle. The first one results from an expansion of a microbubble that is trapped in the nozzle surface, while the second one

results from the breakup of a bubble that enters from upstream of the nozzle and breaks up near velocity boundary layer.

3. Cavitation bubble dynamics in the nozzle is not governed by Rayleigh-Plesset equation. It is likely governed by turbulent flow in the nozzle, although further investigation is needed to confirm this.

4 HIGH-SPEED IMAGING AND TSPIV OF A 3-HOLE MINI-SAC NOZZLE SCALE MODEL

4.1 Relationship between string cavitation, geometrical cavitation, and jet angle

Two kinds of cavitation may occur in mini-sac type diesel injectors. The first is geometrical cavitation, which can usually be seen as a film-like structure in the nozzle. The second is the filament-like string cavitation. Both types of cavitation are known to affect fuel spray characteristics, although the effects of geometrical cavitation and that of string cavitation have not been individually clarified. Moreover, the mechanism behind string cavitation occurrence is still unclear. String cavitation usually occurs at low needle lift, which might be indicative of a vortex ring flow in the sac. However, because of the difficulty in precise flow measurement of the three-dimensional flow structure in the sac, the link between vortex ring flow and string cavitation occurrence in the sac has not been proven. In the current section, results obtained from the high-speed imaging of string cavitation, geometrical cavitation, and discharged liquid jet of an enlarged three-hole mini-sac diesel fuel injector was discussed to clarify the effects of string cavitation and geometrical cavitation on the discharged liquid jet angle. Furthermore, Tomographic Stereo Particle Image Velocimetry (TSPIV) was carried out on the sac. The experiments were conducted at two different needle lifts, to clarify the link between needle lifts and flow structure in the sac, as well as how it affects string cavitation occurrence and liquid jet angle.

4.2 Methodology

4.2.1 High-speed imaging experimental setup

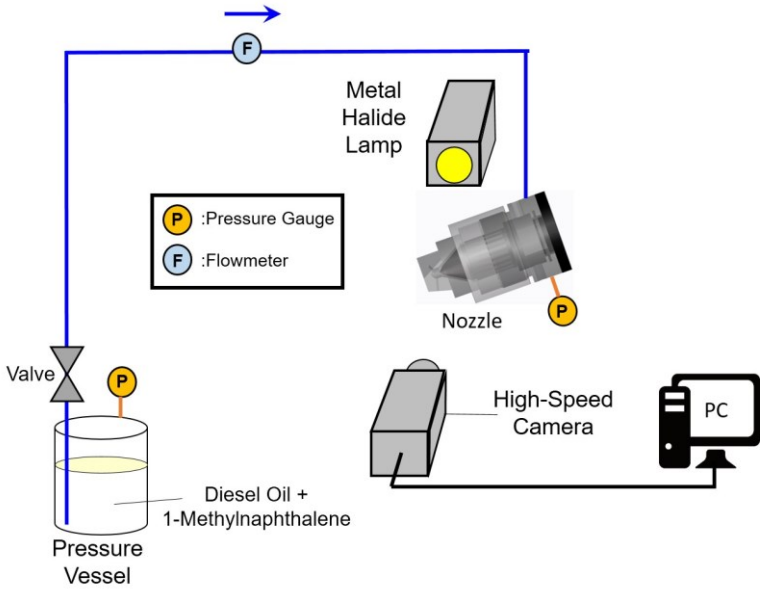

Figure 70 High-speed imaging experimental setup

The experimental setup for high-speed imaging experiment is shown in Figure 70. For the high-speed imaging, the working liquid was discharged from a pressure vessel through the injector into the ambient air at room temperature under steady injection condition, with a liquid temperature of 25°C. Injection pressure was varied from 0.14 to 0.46 MPa. The injector used in the experiments was an acrylic scale model of a three-hole cylindrical mini-sac diesel injector, with a sac diameter of 10 mm, nozzle length L = 8 mm, and nozzle diameter D = 2 mm. Schematic of the injector is shown in Figure 71.

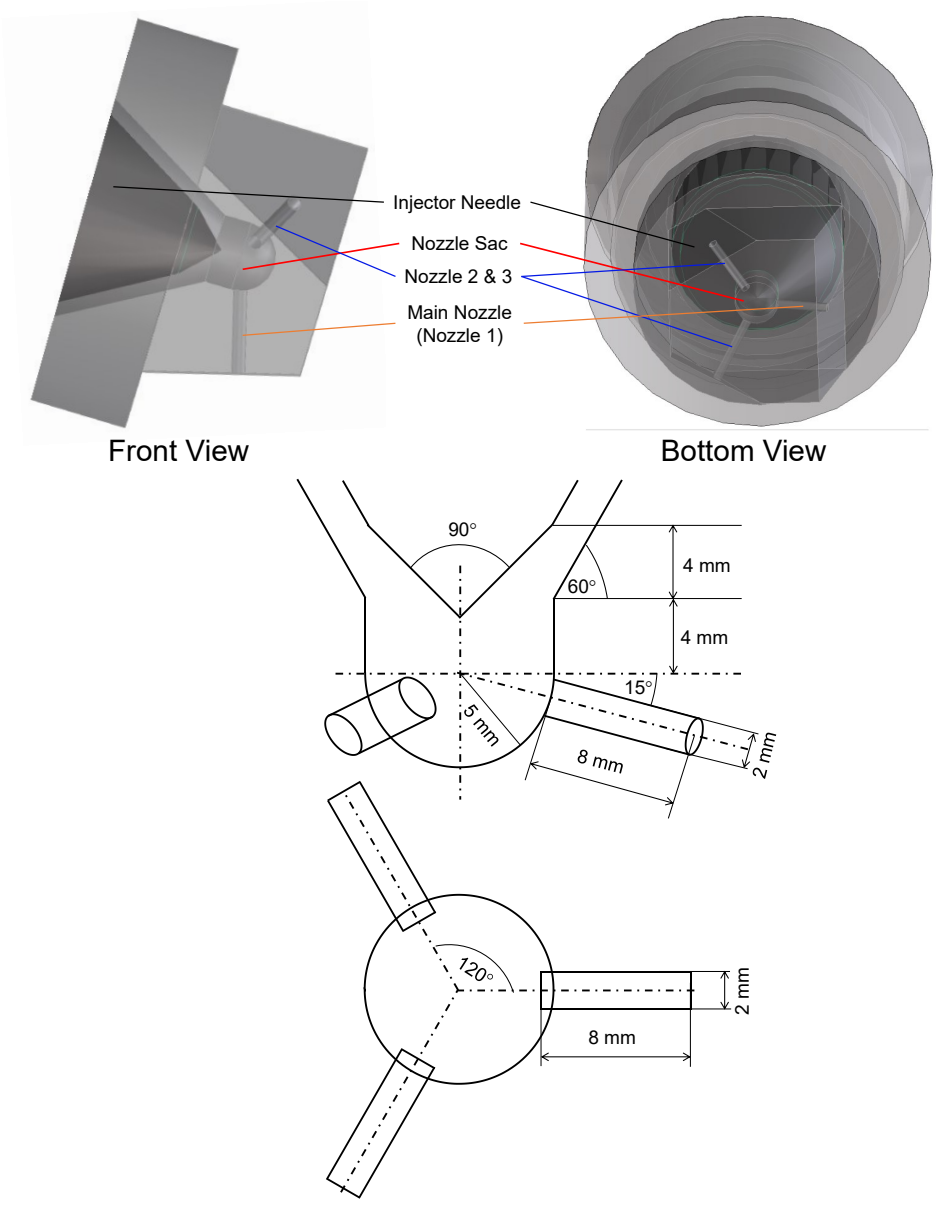

Figure 71 Injector schematic

Experiments were conducted under two needle lift conditions, which are low needle lift (Z/D = 0.5) and high needle lift (Z/D = 3), where Z is the needle seat gap and D is the nozzle diameter. Definitions of Z and D are shown in Figure 72. The flow rate was controlled by vessel pressure and measured with a flowmeter (Keyence FD-SS20A). The measured flow rate was used to derive the mean flow velocity V in the nozzle, using the mass continuity equation. The Reynolds number of the

current experiments are in the same range with those found on real-size injector under normal operating conditions [53], [90]. A high-speed camera (Phantom v211) was used to take images of the sac, geometrical cavitation in the nozzle, and discharged liquid jet at different needle lifts for various liquid flow rates. The images were taken with 3500 fps frame rate, with 8.5 µm / pixel spatial resolution and 10 µs exposure time. Image processing was conducted on the captured images to measure geometrical cavitation length L_c and discharged liquid jet angle θ. The image processing method was similar to the one described previously in Section 3.3.1. For string cavitation occurences, manual counting was carried out on all captured images to determine the images with string cavitation occurrences. Detailed experimental conditions are available in Table 6.

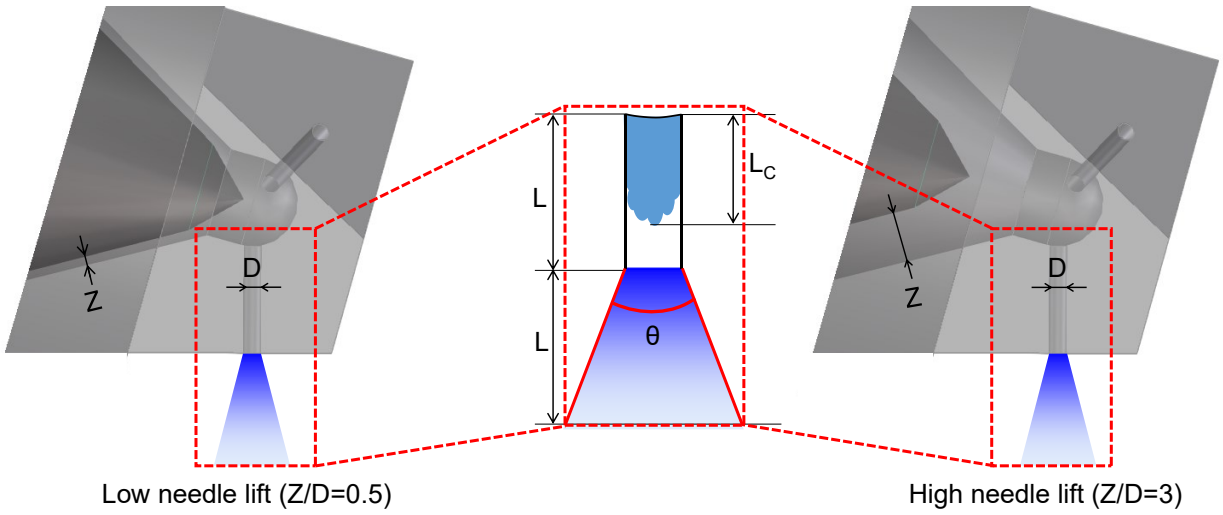

Figure 72 Definitions of L, D, L_c, θ, and Z

Table 6 Experimental conditions for 3-hole injector high-speed imaging and TSPIV

Needle Lift	Geometrical cavitation regime	Back pressure [MPa]	Injection pressure [MPa]	V [m/s]	Re [-]
Z/D = 0.5	No cavitation	0.1	0.32	9.0	5289
	Incipient Cavitation		0.35	13.0	7640
	Developing Cavitation		0.40	15.7	9227
	Super Cavitation		0.42	16.0	9403
	IHF		0.46	17.0	9991
Z/D = 3	No cavitation		0.14	5.0	2939
	Incipient Cavitation		0.23	12.5	7346
	Developing Cavitation		0.27	13.8	8110
	Super Cavitation		0.35	14.1	8287
	THF		0.43	14.3	8404

To obtain a clear, non-refracted image, a solution of diesel fuel and 1-methylnaphtalene [109], [110] was used as the working liquid. The resulting solution have a density of 864 kg/m^3 and a dynamic viscosity of 2.94 mPa·s. The density and the dynamic viscosity was measured with an electric scale (A&D FZ-1200iWP) and a viscometer (A&D SV-10). The addition of 1-methylnaphtalene might alter the property of the diesel fuel, especially in regards to cavitation. However, as 1-methylnaphtalene has a very low vapor pressure compared to the injection pressure in the current study, the overall effect is expected to be negligible. Comparison between the images obtained with normal diesel fuel and index-matched diesel fuel are shown in Figure 73.

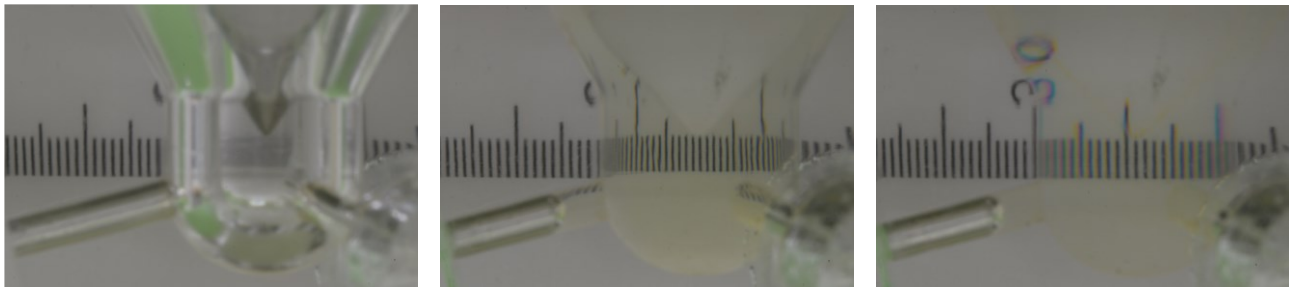

Empty injector | Diesel fuel | Diesel fuel + 1-methylnapthalene

Figure 73 Comparison of normal diesel oil and index-matched diesel oil solution

4.2.2 TSPIV Experimental setup

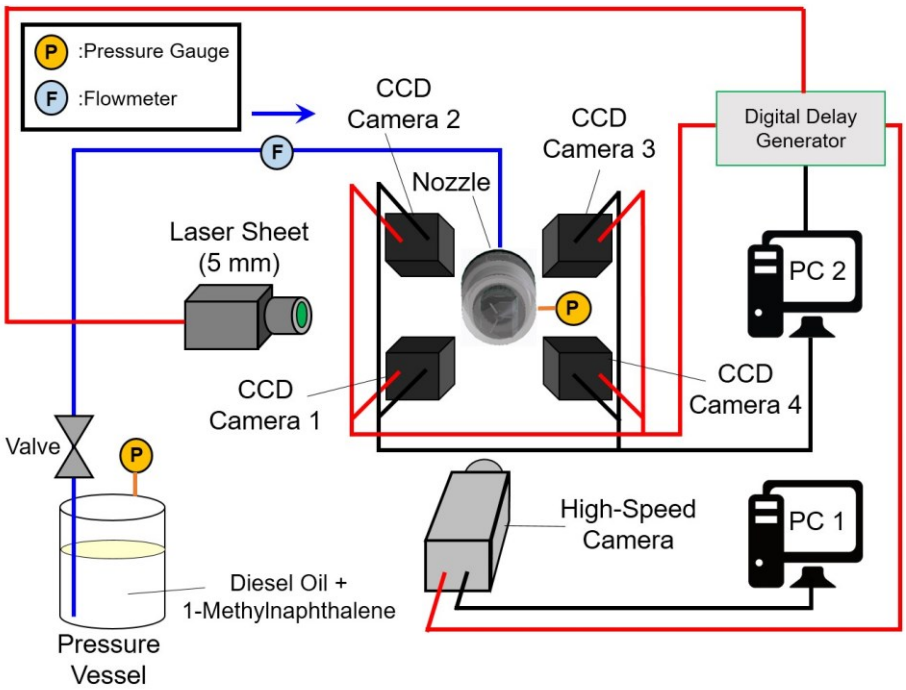

Figure 74 TSPIV experimental setup

The TSPIV experimental setup is shown in Figure 74. The TSPIV experiment was carried out at five horizontal planes at z = -2, -1, 0, 1, and 2 mm, as shown in Figure 75, under similar injection conditions to that of the high-speed imaging. The TSPIV system consisted of a double-pulsed Nd:YAG laser sheet (60 μs in duration, 5 mm in sheet thickness) which was synchronized to four

linked CCD cameras (JAI AM-200GE). As occurrences of string cavitation happened in a very short time frame (~10 ms) and the CCD cameras have a very slow frame rate (10 fps), a high-speed visualization (Photron SA-Z) with 3000 fps frame rate was conducted simultaneously in order to clarify the link between the flow structure of the sac and the transient behaviour of string cavitation. A digital pulse generator (SRS DG645) was used to synchronize the start time of the CCD cameras, laser sheet, and the high-speed camera. A calibration plate shown in Figure 76 was used to calibrate the particle position and intensity of each camera. The calibration plate consisted of 49 dots with 0.423 mm in diameter. The outer diameter of the calibration plate was 8 mm. Calibration was carried out by moving the calibration plate every 0.25 mm in the range of laser sheet thickness, to determine the positional relationship amongst the CCD cameras. Fluorescent particles (Fluostar 0459, 15 μm in diameter, 1.1 in specific weight) were used as the seeding particle for the TSPIV.

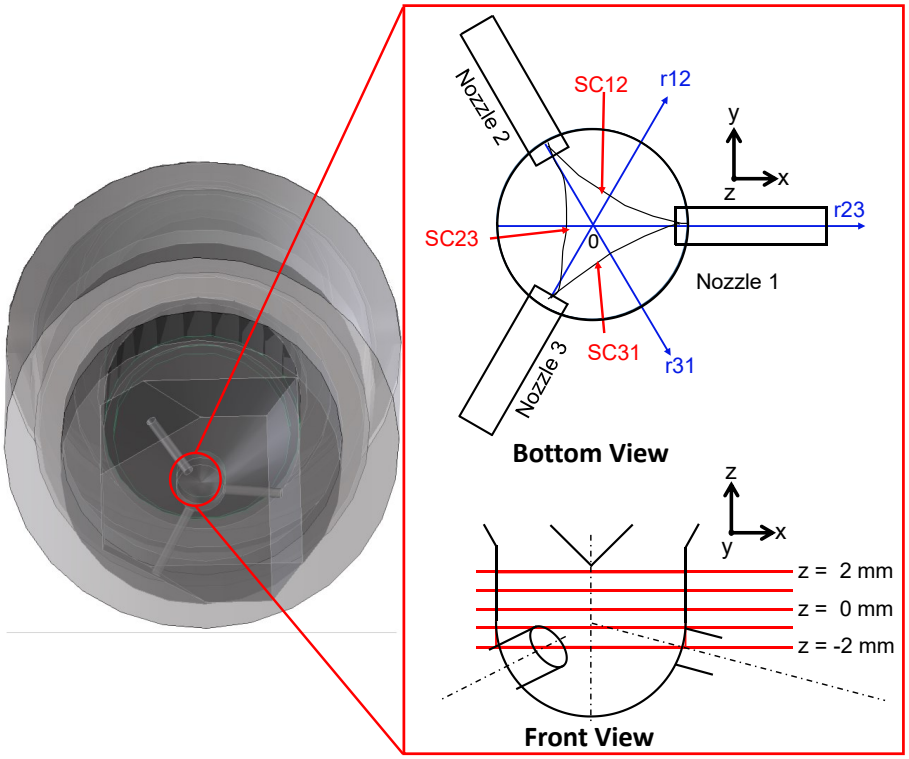

Figure 75 Definitions of z, r, and SC

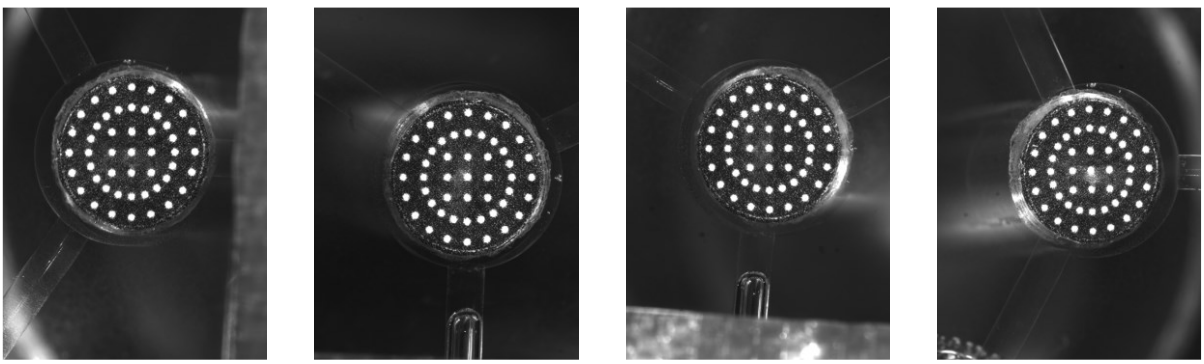

Figure 76 TSPIV calibration plate

200 pairs of images were taken for the TSPIV measurement, with the internal Δt of 60 μs between the first and the second frames. Raw images sample are shown in Figure 77. After the imaging process of the flow with the tracer particles in the sac has been carried out, a combined image shown in Figure 78 was created from four frames of raw images, to serve as a benchmark to determine the absolute positions of the particles that will be reconstructed in 3D space. Correlating this image with the position and intensity data recorded previously during the calibration process, adjustment can be made to the position and of particles in the raw images. Sample of adjusted images are shown in Figure 79. The adjusted images will be used to create 3D images with a resolution of 0.0125 mm / voxel, with x_v = 1440, y_v = 1440, z_v = 440. Using the 3D images, a PIV analysis can then be conducted. The PIV analysis was conducted with an interrogation window of 33 x 33 pixel and search window of 53 x 53 pixel, with 50% overlap between adjacent interrogation windows.

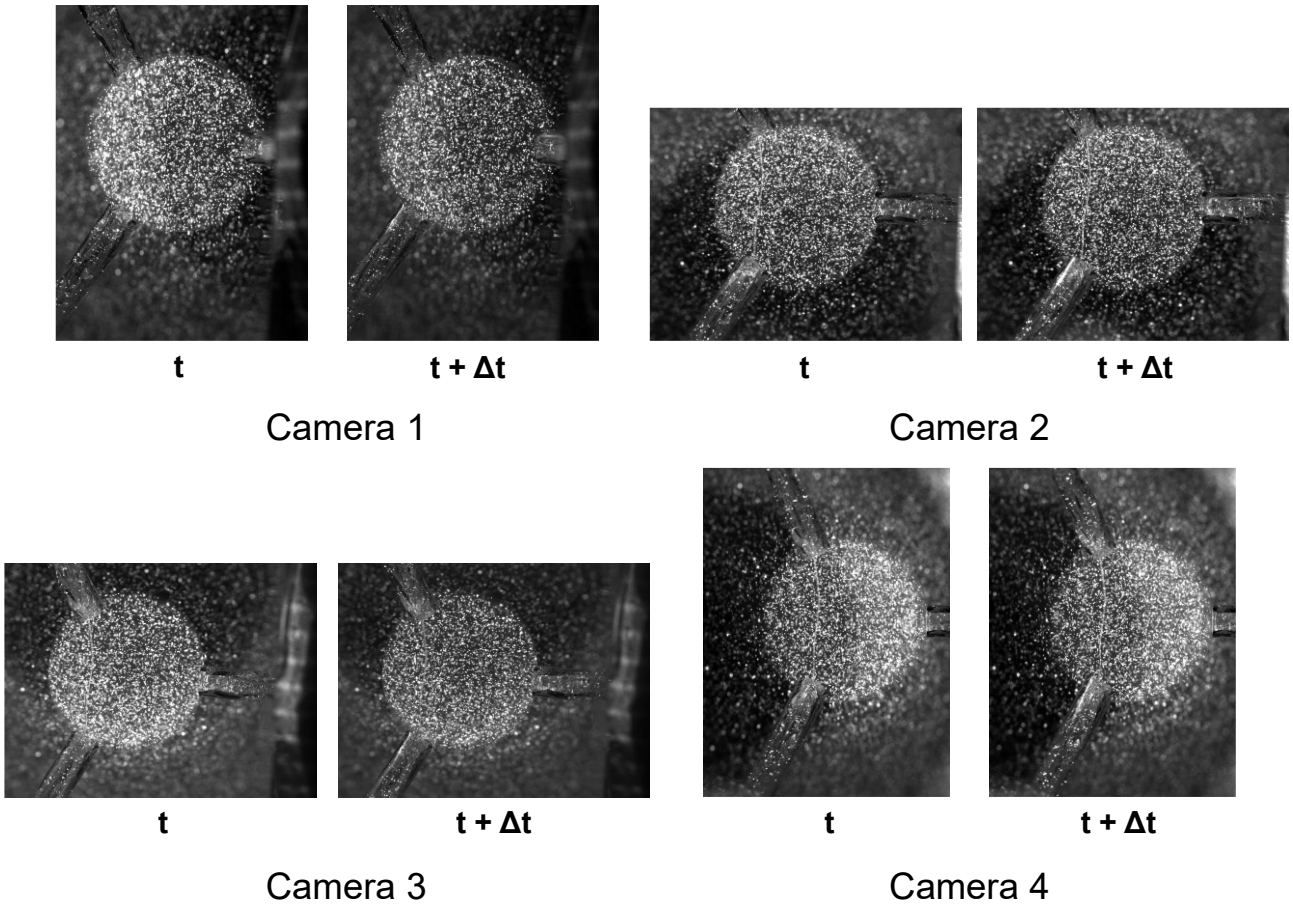

Figure 77 RAW TSPIV images

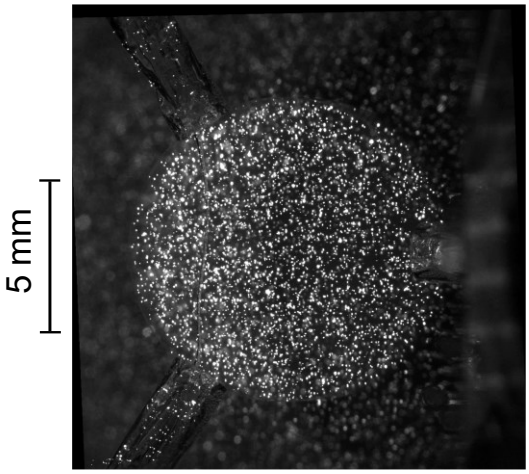

Figure 78 Benchmark image to determine absolute position of the particles

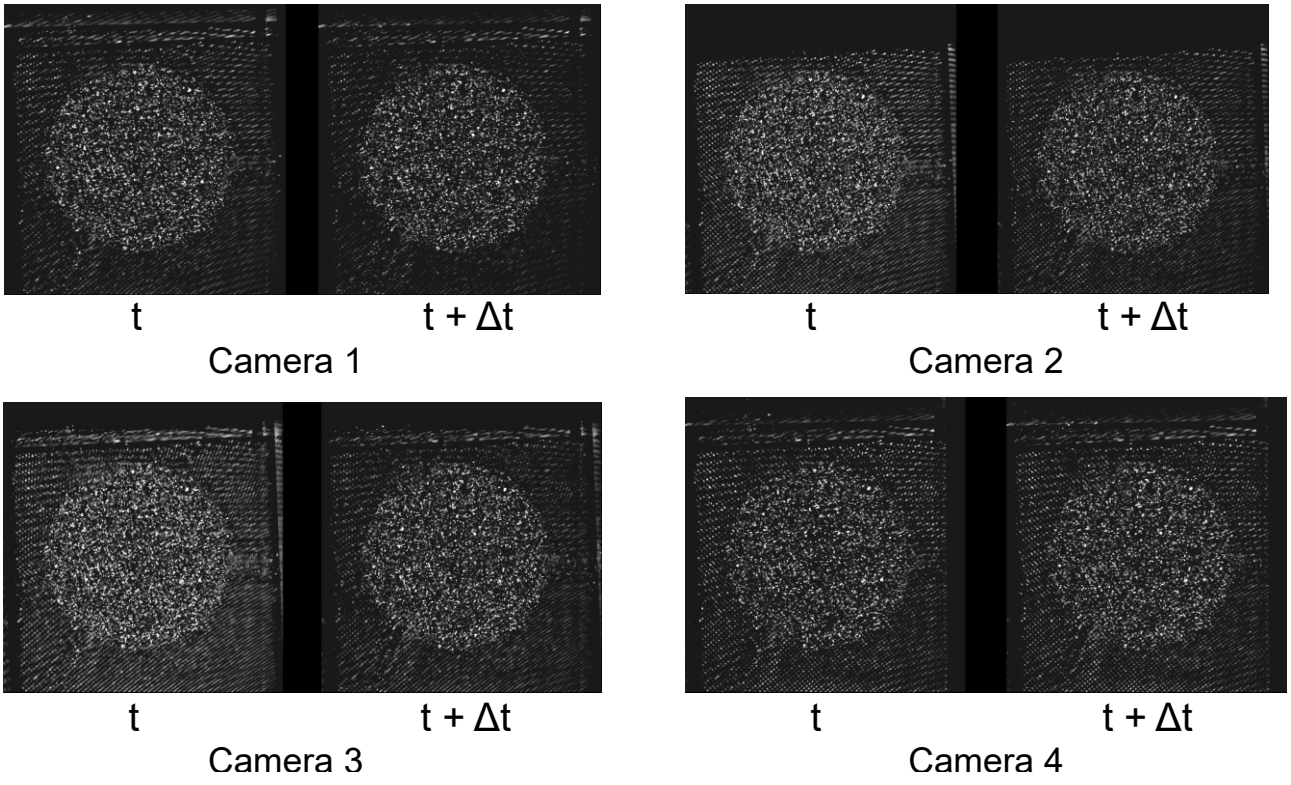

Figure 79 Image pairs with adjusted particles position

4.3 Results and Discussion

4.3.1 Individual effects of geometrical cavitation on discharged liquid jet

Representative images of geometrical cavitation in the main nozzle for both low and high needle lifts (Z/D = 0.5 and Z/D = 3, respectively) are shown in Figure 80. As mean flow velocity V in the nozzle increases, cavitation in the nozzle grows in accordance with the in-nozzle cavitation regime characterization defined by Sou et al. [97]. Liquid jet deformation by cavitation mainly occurs as the result of the radial flow reattachment of the separated flow to the wall and the vortex flow structure shed from the reattachment point, appearing as a cavitation cloud. Because of this, jet

deformation is especially large at super cavitation regime, as the flow reattachment point, which is located at the tail end of the cavitation film, is very close to the nozzle exit.

As V continues to increase, eventually the cavitation will reach hydraulic flip regime, where the film extends to the nozzle exit, resulting in the entry of surrounding gas into the nozzle. From the liquid jet deformation standpoint, hydraulic flip is often considered unfavorable. Because there is no reattachment to the wall within the nozzle at this regime, the aforementioned enhancement mechanism of jet deformation cannot occur. As a result, the resulting liquid jet will have a very smooth structure, with minimal deformation at the liquid jet surface.

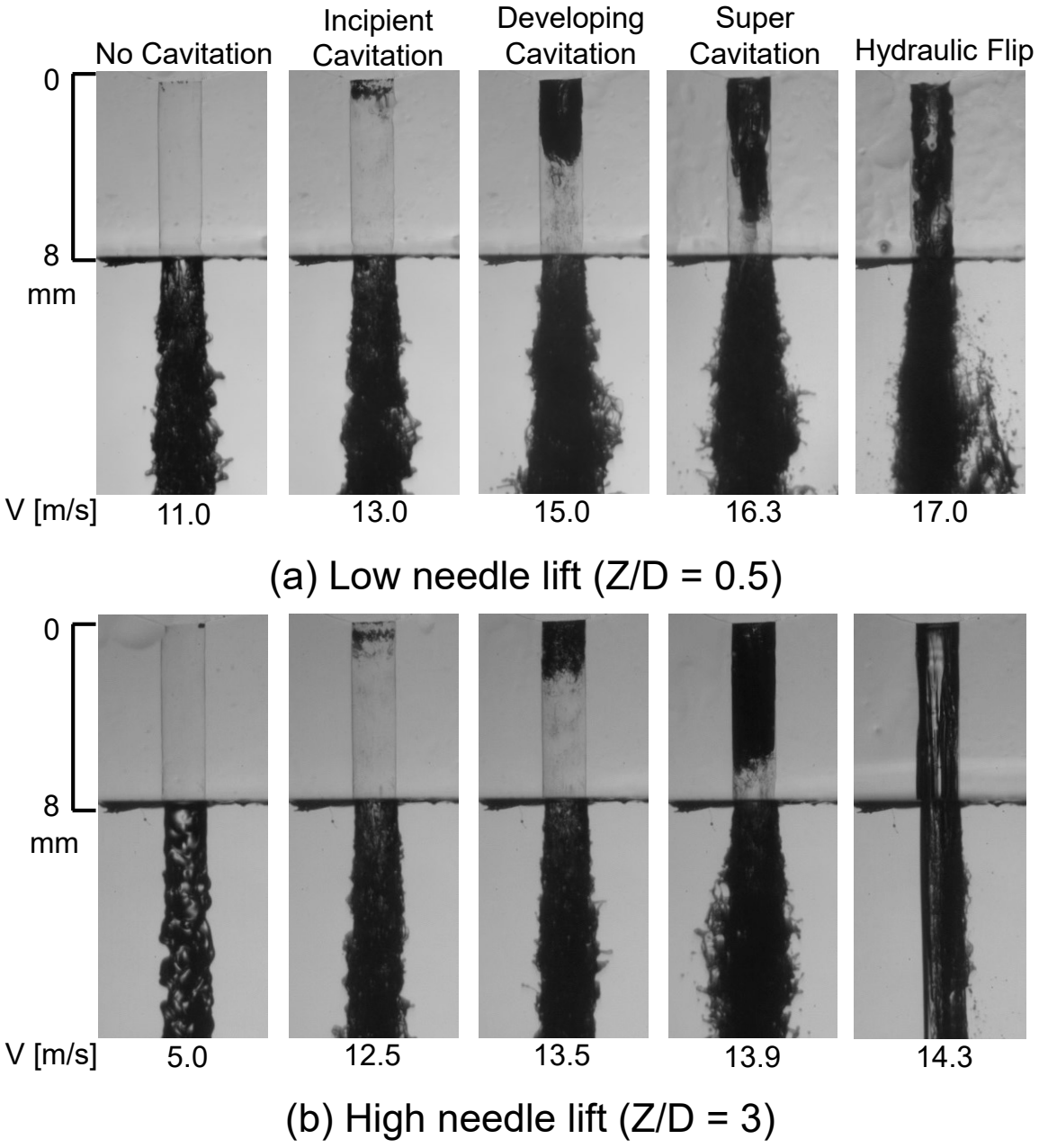

Figure 80 Geometrical cavitation regimes in the nozzle

Although hydraulic flip commonly results in a smooth liquid jet, it is noticeable from Figure 80 that for low needle lift, liquid jet behavior under hydraulic flip regime is rather different. For low needle lift, jet deformation still occurs at hydraulic flip, which essentially results in a liquid jet whose behavior

is similar to liquid jet at super cavitation regime. This is caused by another mode of hydraulic flip, which is commonly called Imperfect Hydraulic Flip (IHF), in contrast to the Total Hydraulic Flip (THF) [82]. At IHF, reattachment of the flow to the wall frequently occurs, which results in the jet deformation enhancement. Recent x-ray investigations of liquid jet at IHF has shown that the structure of liquid jet at super cavitation and imperfect hydraulic flip are quite similar [146].

The relationship between liquid jet angle θ and normalized cavitation length L_c/L at low and high needle lifts is shown in Figure 81. From Figure 81, it can be seen that for Z/D = 3, θ is suppressed (θ ≤ 7 degrees) at THF (L_c/L = 1), resulting in the small average jet angle, as small as that found at no cavitation regime. Meanwhile, for Z/D = 0.5, θ at IHF is more or less comparable to θ at super cavitation regime. Another thing that can be observed is the fact that θ at all geometrical cavitation regime is larger for Z/D = 0.5 than that for Z/D = 3. For Z/D = 3, large θ (θ ≥ 20 degrees) only occurs when L_c/L ≥ 0.7. In other words, in the case of high needle lift, large θ appears only at super cavitation regime. On the other hand, for Z/D = 0.5, large θ can be found in all the range of L_c/L, including the case where L_c/L = 0. This fact shows that while θ is mainly governed by geometrical cavitation at high needle lift, θ at low needle lift is not only affected by geometrical cavitation but also by the helical flow in the nozzle.

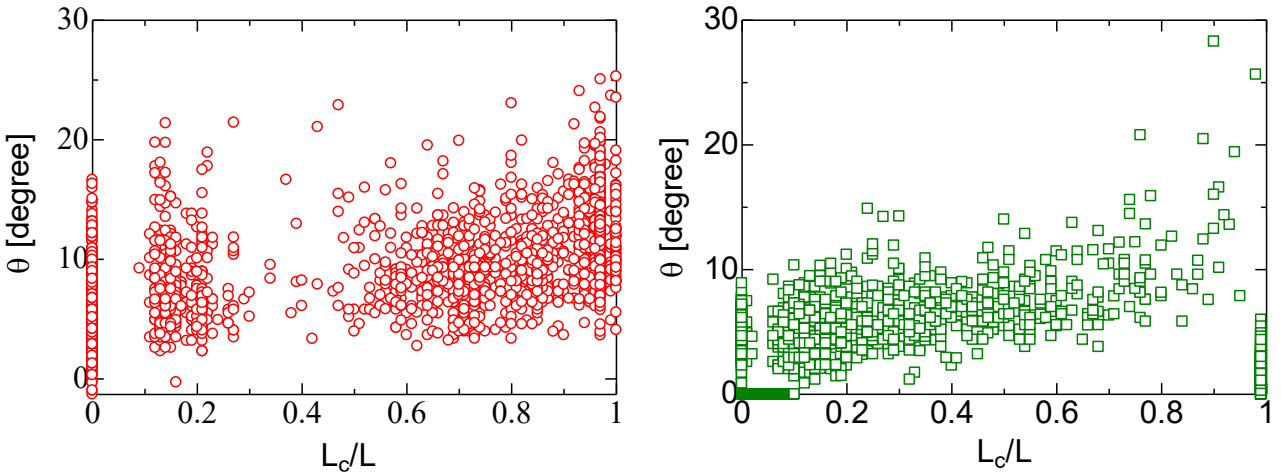

(a) Low needle lift (Z/D = 0.5) (b) High needle lift (Z/D = 3)

Figure 81 θ vs L_c/L

4.3.2 Individual effects of string cavitation on discharged liquid jet

Representative images of string cavitation in the sac at low needle lift are shown in Figure 82. String cavitation may occur as a result of vortex ring flow inside the sac of fuel injectors. When a bubble nucleus travels to the core of the vortex, it will expand and turn into a string-like cavity [147] similar to those commonly found at the blade tip of a propeller. Because the vortex ring envelops the entire sac, multiple string cavitations may appear at the same time.

High-speed images of the sac, main nozzle, and the discharged liquid jet at Z/D = 0.5 and 3 are shown in Figure 83. To clearly show the effect of string cavitation on the liquid jet, images at no-cavitation regime are shown. String cavitation was only observed at low needle lift. The jet angle at low needle lift during the period of 40 ms is larger than that at high needle lift, even without string

cavitation. When string cavitation occurs, the jet angle is further increased. The occurrence of string cavitation in the sac and the nozzle of fuel injectors has been reported to affect the discharged spray greatly by various studies [47], [50], [53], [90], [148]. Some of the studies have also reported that string cavitation might have a greater influence on the liquid jet than geometrical cavitation [47], [50], [53], [90]. When string cavitation reaches the proximity of nozzle exit, the helical flow near the nozzle exit became dominant, which results in a hollow cone liquid jet [48], [50], [53], [148]

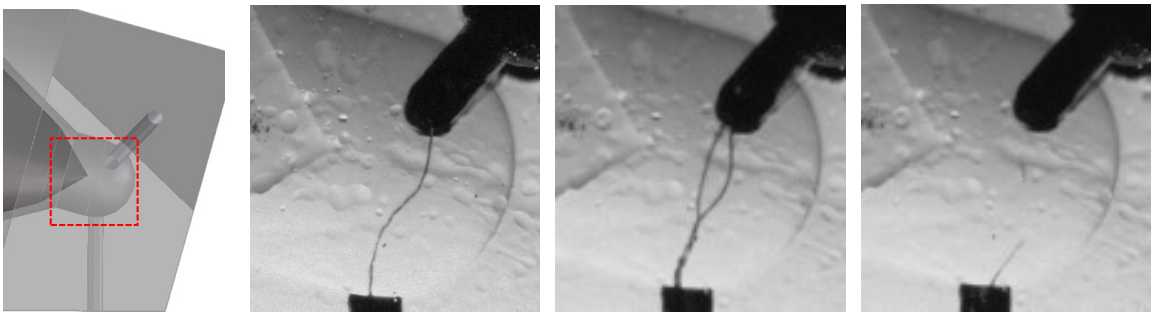

(a) Front view

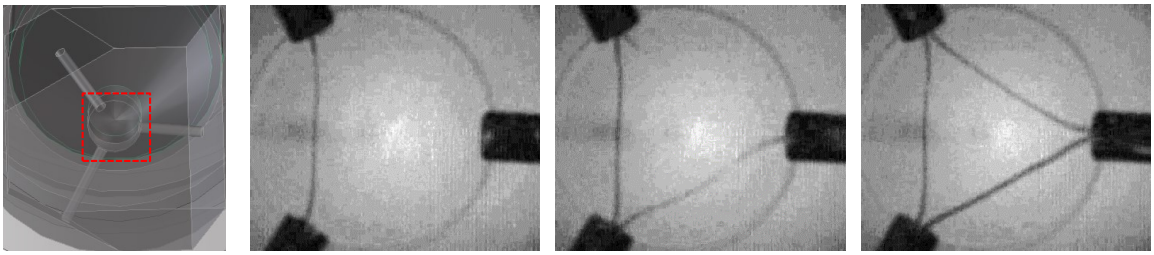

(b) Bottom view

Figure 82 String cavitation in the sac

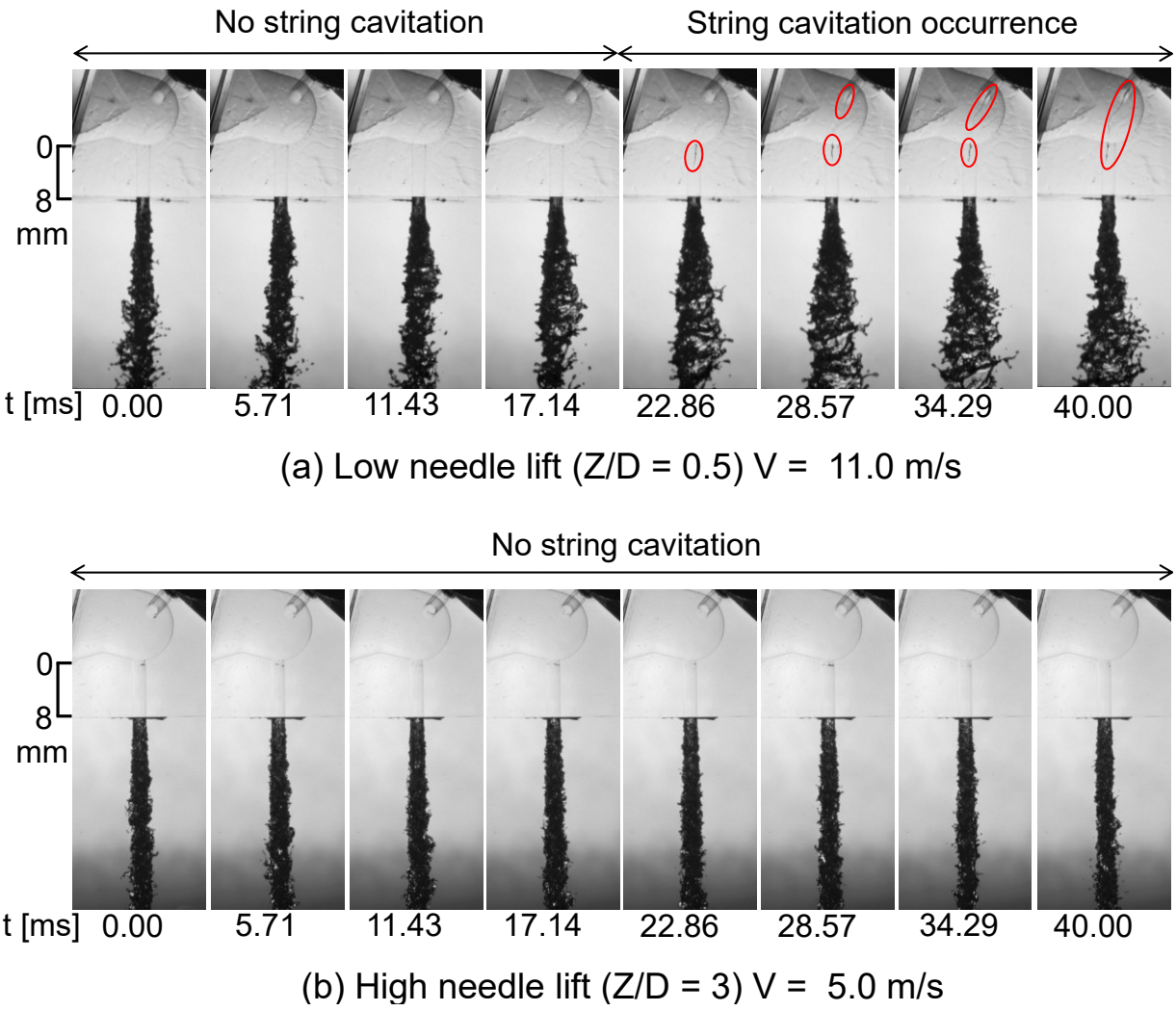

Figure 83 High-speed images of the sac, nozzle, and discharged liquid jet

As stated above, the effect of string cavitation on the discharged liquid jet can be qualitatively observed. However, the individual effects of string cavitation and geometrical cavitation on the liquid jet in multi-hole injector when both types of cavitation occur simultaneously have not been clarified yet. Andriotis and Gavaises [47] have made some considerable effort to separate the effects of string cavitation and geometrical cavitation in single-hole, two-hole, and five-hole injectors. However, they only obtained conclusive results for the single-hole injector. In the present study, in order to clarify the individual effects of string cavitation and that of geometrical cavitation on θ in a multi-hole injector, high-speed visualization of the sac, main nozzle, and discharged liquid jet was conducted. From the captured high-speed images, measurements of L_c/L, θ, and string cavitation occurrence were conducted, as previously described in Section 4.2.1. Measurements were carried out on 350 frames, or equal to 100 ms time period. The results for high and low needle lifts are presented in Figure 84 and 79, respectively. For string cavitation occurrence, 1 denotes the frames where string cavitations were observed while 0 are frames without string cavitation. The average value of measured L_c/L, θ, and string cavitation occurrence rate for both needle lifts are shown in Figure 86. Each data points in Figure 86 was obtained by averaging the measured data from 350 frames.

Under high needle lift condition, measured θ increases with L_c/L, in accordance with the observation by Sou et al. [97]. At THF regime, θ decreases drastically. The same θ trend can be clearly seen in Figure 86. The averaged L_c/L for Z/D = 3 in Figure 86 is shorter than expected. L_c/L is less than 0.4 at super cavitation regime, due to the large fluctuation of L_c/L. As θ is affected by L_c/L, the fluctuation can also be seen in the measured θ, with peaks of θ occurring concurrently with peaks of L_c/L. This is especially obvious for large L_c/L. For example, in Figure 84, at the super cavitation regime (V = 14.1 m/s), peaks of L_c/L and increases in θ can be observed at t = 23, 50, and 78 ms. From this result, it can be concluded that the θ of multi-hole injector at high needle lift is largely dependent on geometrical cavitation, similar to symmetrical single-hole injector [95].

Figure 85 shows that the measured θ at all cavitation regime for low needle lift is larger than that for high needle lift. It should be pointed out that there are instances of sudden increases in θ when string cavitation occurs. For example, at t ≈ 50 and 63 ms in Figure 85(a), t ≈ 30 and 60 ms in Figure 85(b), and t ≈ 20 ms in Figure 85(c). However, one might notice that the increases in measured θ do not always happen at the same time with string cavitation occurrences. This is especially true for longer L_c/L, where geometrical cavitation makes it difficult to confirm string cavitation occurrences in the nozzle. The string cavitation occurrence rate shown in Figure 86 shows that string cavitation occurrence rate is lower at $L_c/L \geq 0.7$.

Comparing Figure 84 and 79, it can be clarified that string cavitation at low needle lift exhibits larger influence on liquid jet angle than geometrical cavitation. However, the additional increase in θ caused by string cavitation is relatively small (5 – 10 degrees) when geometrical cavitation exists. The result is consistent with that reported by Andriotis and Gavaises [47] for single-hole nozzle.

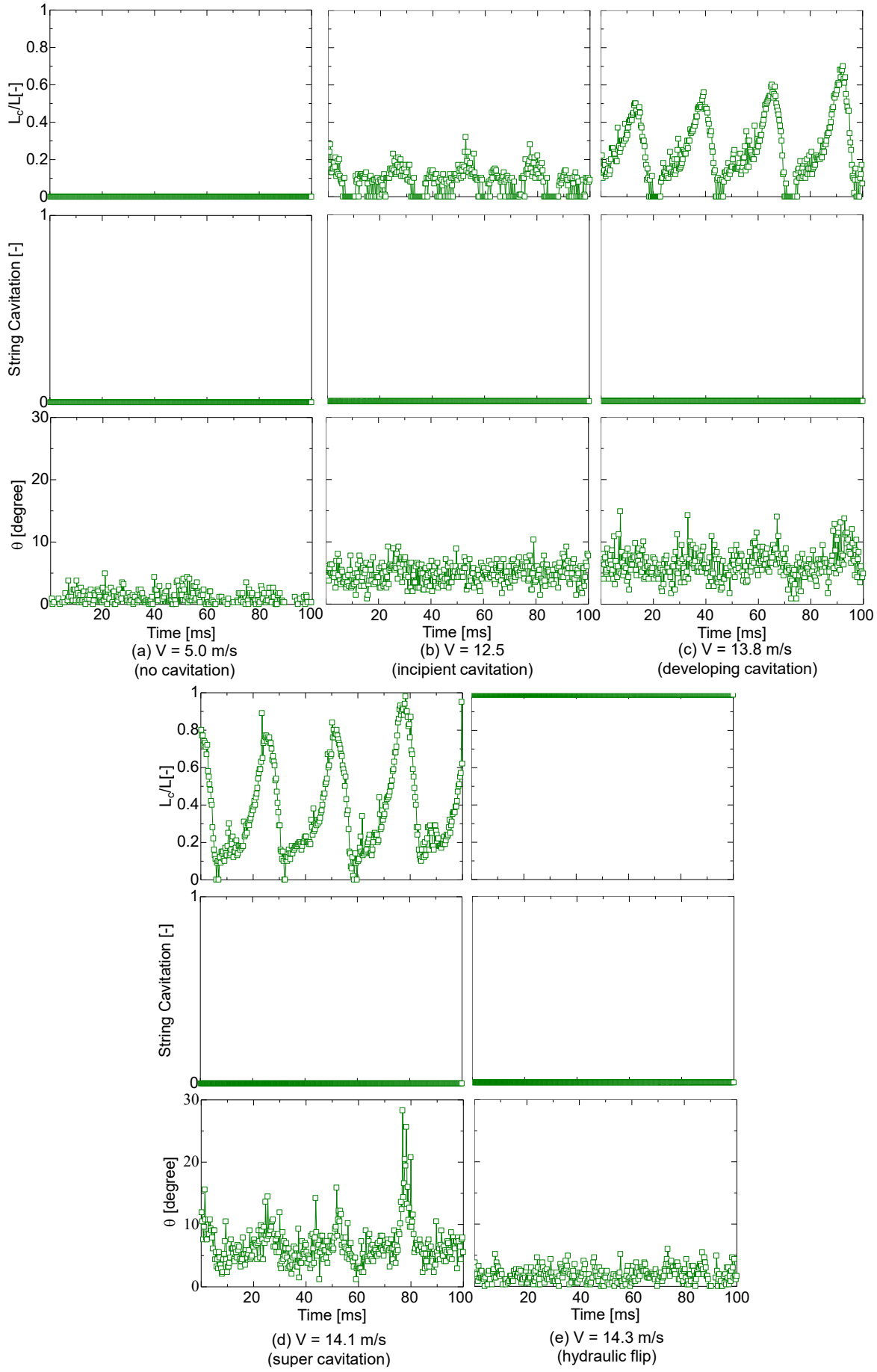

Figure 84 String cavitation occurrences, L_c/L, and θ at high needle lift (Z/D = 3)

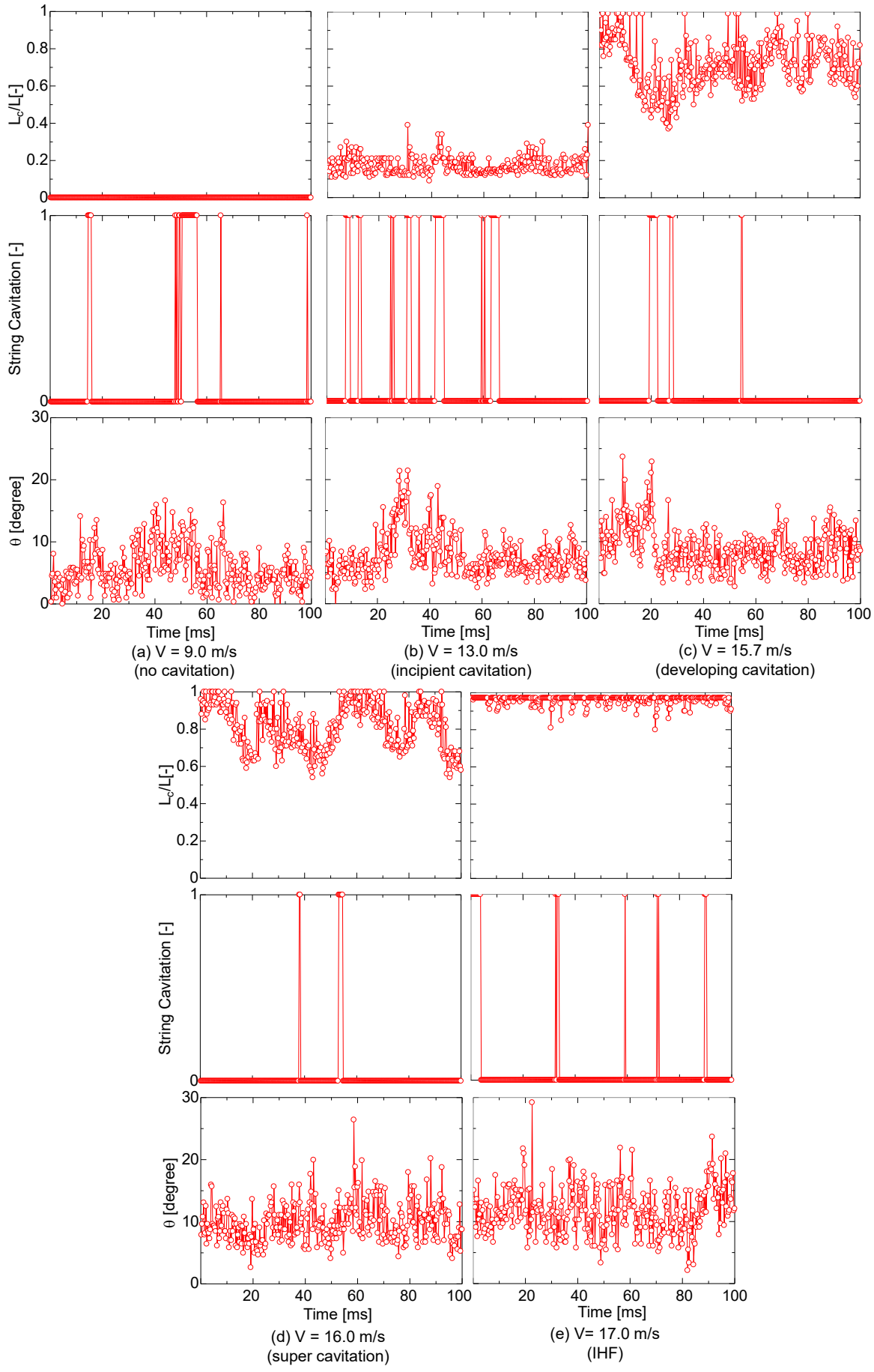

Figure 85 String cavitation occurrences, L_c/L, and θ at low needle lift (Z/D = 0.5)

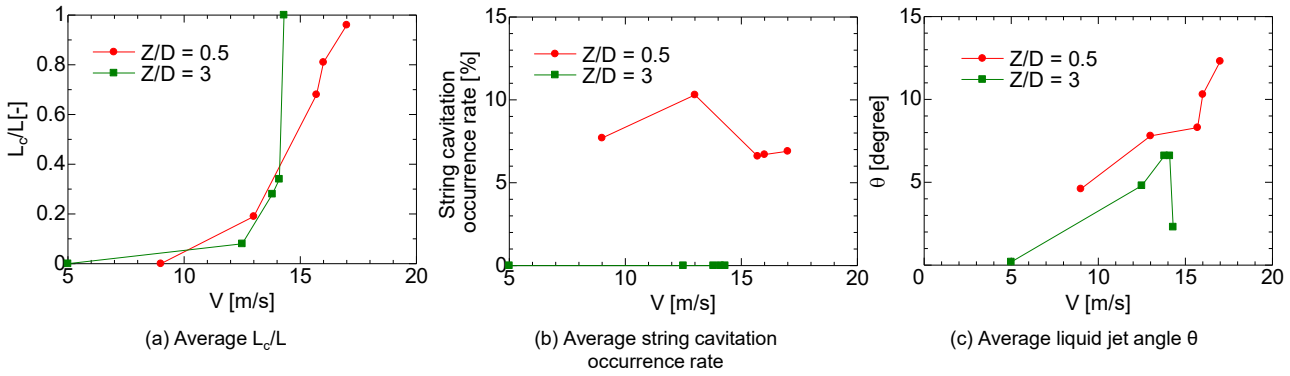

(a) Average L_c/L (b) Average string cavitation occurrence rate (c) Average liquid jet angle θ

Figure 86 Averaged L_c/L, string cavitation occurrence rate, and θ

4.3.3 Effects of needle lift on string cavitation occurrences

This section presents the results of the TSPIV experiment. String cavitation can only occur at places with strong vortical flow, such as the sac at low needle lift [90], [149]. The vortex ring flow at low needle lift may induce helical flow in the nozzle, resulting in a hollow cone liquid jet and increases θ. In other words, the increase in θ at low needle lift might not be directly induced by string cavitation itself, but probably by the helical flow in the nozzle. At low needle lift, string cavitation does not always appear even when there is a vortex ring flow in the sac. Because of this, string cavitation might only occurs when the vortex is particularly strong, thus string cavitation occurrence can serve as an indicator of a strong vortex. It is of great interest to conduct flow measurement in the sac to explore the conditions that lead to instances of string cavitation occurrence. First, time-averaged velocity distributions at the center plane r23 of the sac are shown in Figure 87. It should be addressed that because the diameter of the calibration plate is smaller than the size of the sac (sac diameter is 10 mm, while calibration plate diameter is 8 mm), the decrease in accuracy near the sac wall cannot be avoided. For Z/D = 3 velocity distribution is relatively uniform, while for Z/D = 0.5, the downward velocity near the center of the sac (x = 0 mm) is smaller than that near the sac wall due to the needle valve, as illustrated in Figure 87(a) and (b). With such velocity gradient, it is possible vortex ring flow to induce string cavitation occurrence. A closer look at the instantaneous flow field around string cavitation is needed to investigate the transient behavior of string cavitation.

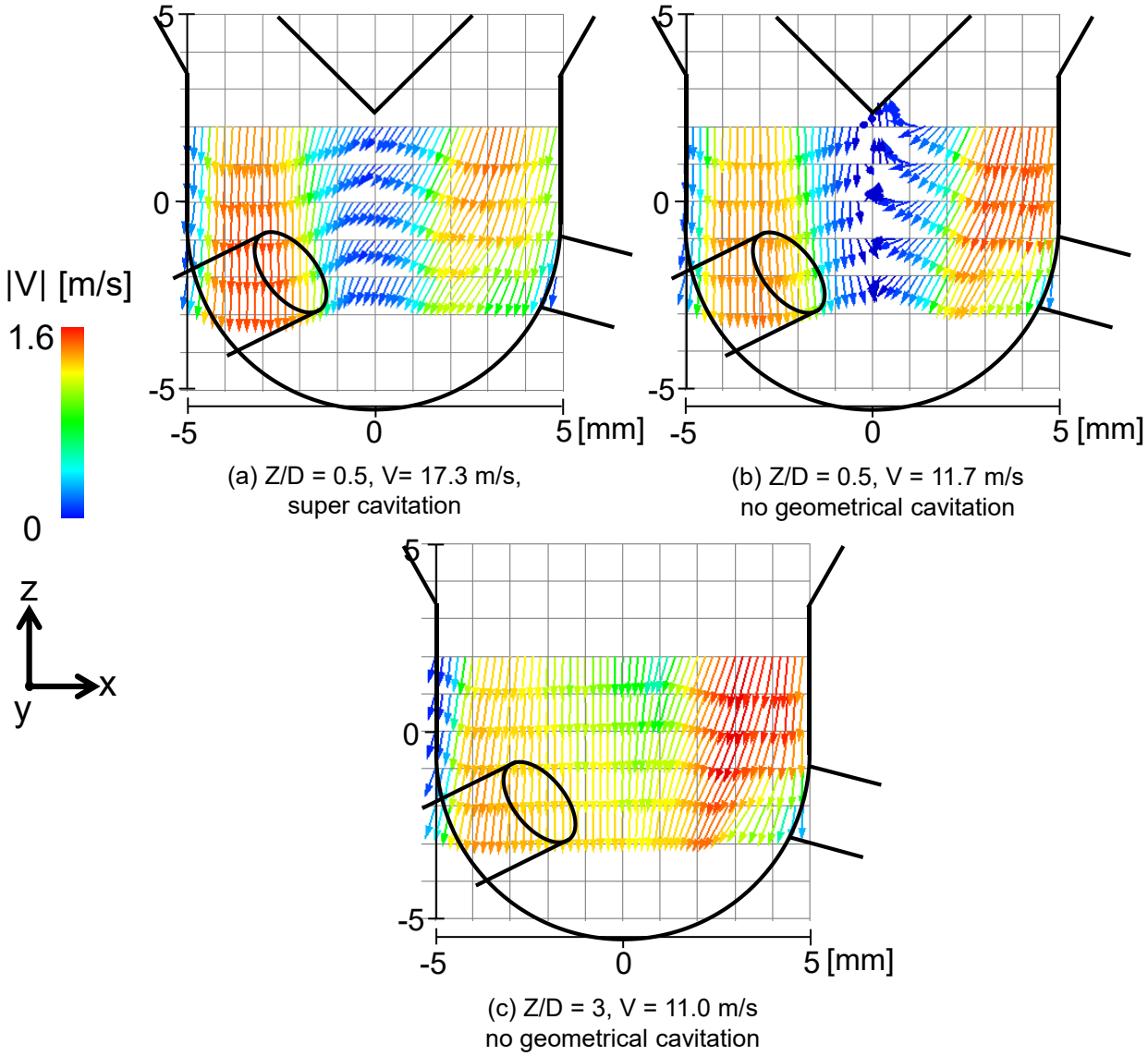

Figure 87 Time-averaged velocity distribution in the center plane of the sac

As previously explained, string cavitation shows a transient behavior. To resolve this, instantaneous velocity distributions before and during occurrences of string cavitation at r23 measurement plane are shown in Figure 89 for V = 17.3 m/s (super cavitation regime). Due to the low temporal resolution of the TSPIV images and the randomness of string cavitation occurrences, a virtual time parameter t_v is introduced to examine the time history of instantaneous velocity field before and during string cavitation occurrences. The definition of t_v is shown in Figure 88, where t_v = 0 is defined as the onset of string cavitation occurrence. Using t_v, several instances of measured flow fields are considered as a single event before and during the occurrence of string cavitation. In the cases shown in Figure 89(c) and (d), string cavitation occurs between nozzle 2 and nozzle 3 (SC23). From Figure 89, it is can be seen that the inflow from needle seat is stronger near the sidewall of the sac and appearance of vortex ring can be found in the sac during string cavitation occurrence. The string cavitation is clarified to originate from this vortex ring.

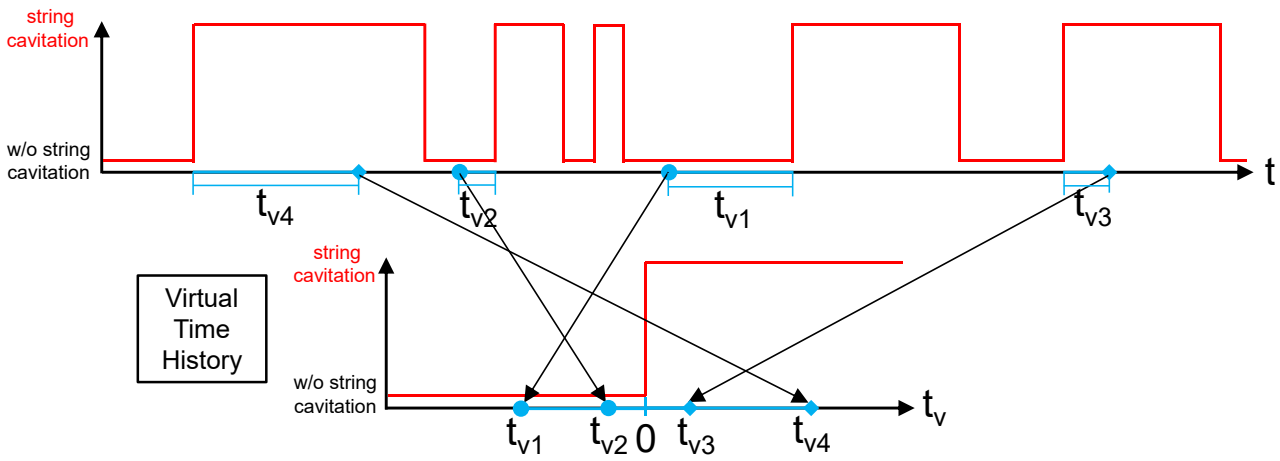

Figure 88 Definition of virtual time t_v

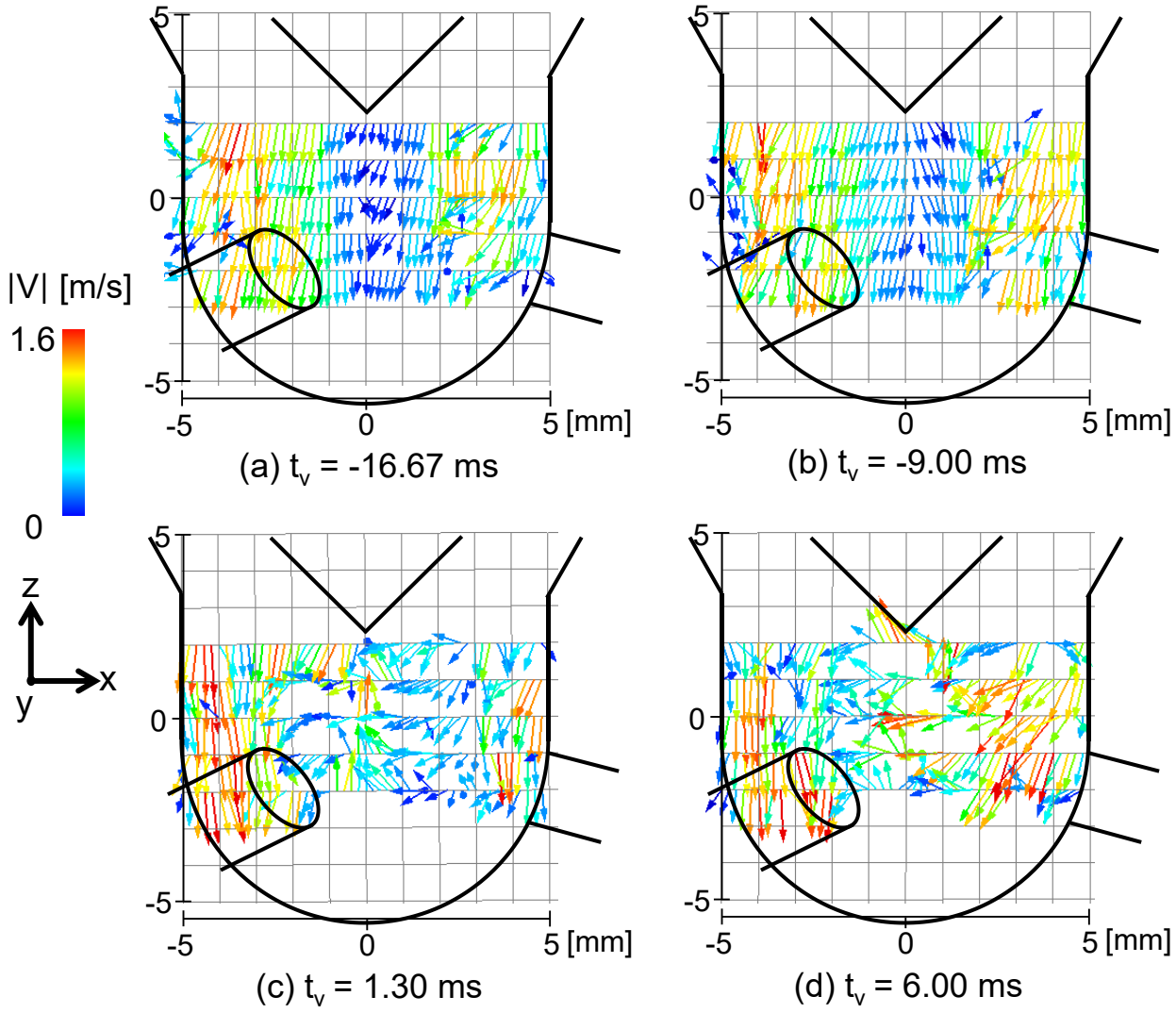

Figure 89 Instantaneous velocity distribution in the center plane of the sac at Z/D = 0.5 (V = 17.3 m/s)

A detailed look at the contour of vertical flow velocity V_z on the horizontal plane near the nozzle inlet (z = -2 mm) is shown in Figure 90. While V_z near the center axis of the sac is close to zero when there is no string cavitation, V_z shows a clear increase in the upward direction when string cavitation occurs.

The radial profiles of V_z at z = 0, -1, and -2 mm for t_v = -9.00 and 1.30 ms are shown in Figure 91. Vortex ring flow can be observed before and during string cavitation occurrence, as evident from the positive V_z in the middle of the sac and negative velocity everywhere else. However, in Figure 91(b), a larger gradient in V_z is apparent for $\partial V_z/\partial$(r23) at the regions near r23 = -2 mm, where string cavitation SC23 passes through r23. As higher gradient in V_z is indicative of a higher vortex strength, this proves that string cavitation can serve as an indicator of the vortex strength. String cavitation is formed when a bubble nucleus is trapped in the vortex core at the exact time when the V_z gradient becomes high (i.e. vortex strength is high). In this case, the microbubble will elongate and turns into a string-like cavity, as described by Choi et al. [59]. This inception process and the unsteady flow in the sac contribute to the randomness of string cavitation occurrence in fuel injectors. To summarize: In the case of low needle lift, vortex ring flow always forms in the sac, even when there is no string cavitation. The vortex ring flow makes it possible for string cavitation to occur at low needle lift if there is a trapped bubble nucleus in the vortex when the vortex is strong. As the high pressure utilized in modern common rail diesel injectors increases the gas solubility of the fuel, it is almost impossible to remove all nuclei in liquid fuel. Coupled with the fact that real-size injectors utilize needle lift that is quite low, where the needle lift at full open condition is approximately equivalent to Z/D=1, this means that string cavitation could occur more easily in real injectors. Considering these facts, attention should especially be paid to the flow field when considering cavitation control strategy in the development of multi-hole fuel injectors. It is important to note that the Reynolds number in this experiment is similar to those found on normal operating conditions of diesel injectors [53], [90], which means that it is possible for flow conditions found in the current study to also occur in real injectors.

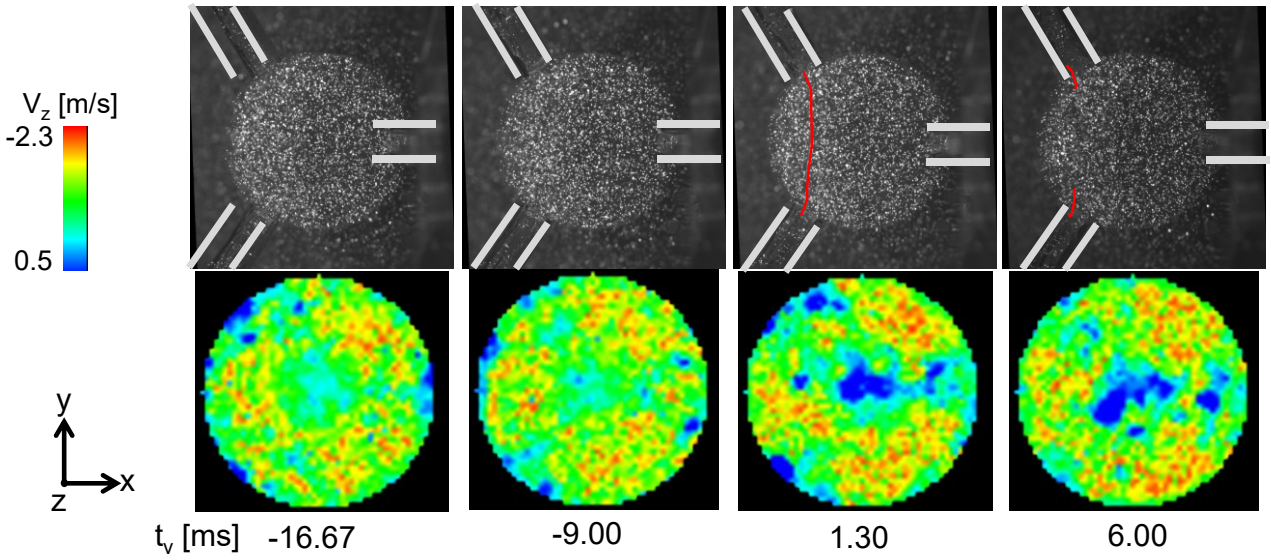

Figure 90 Instantaneous V_z contour (z = -2 mm) at Z/D = 0.5 (V = 17.3 m/s)

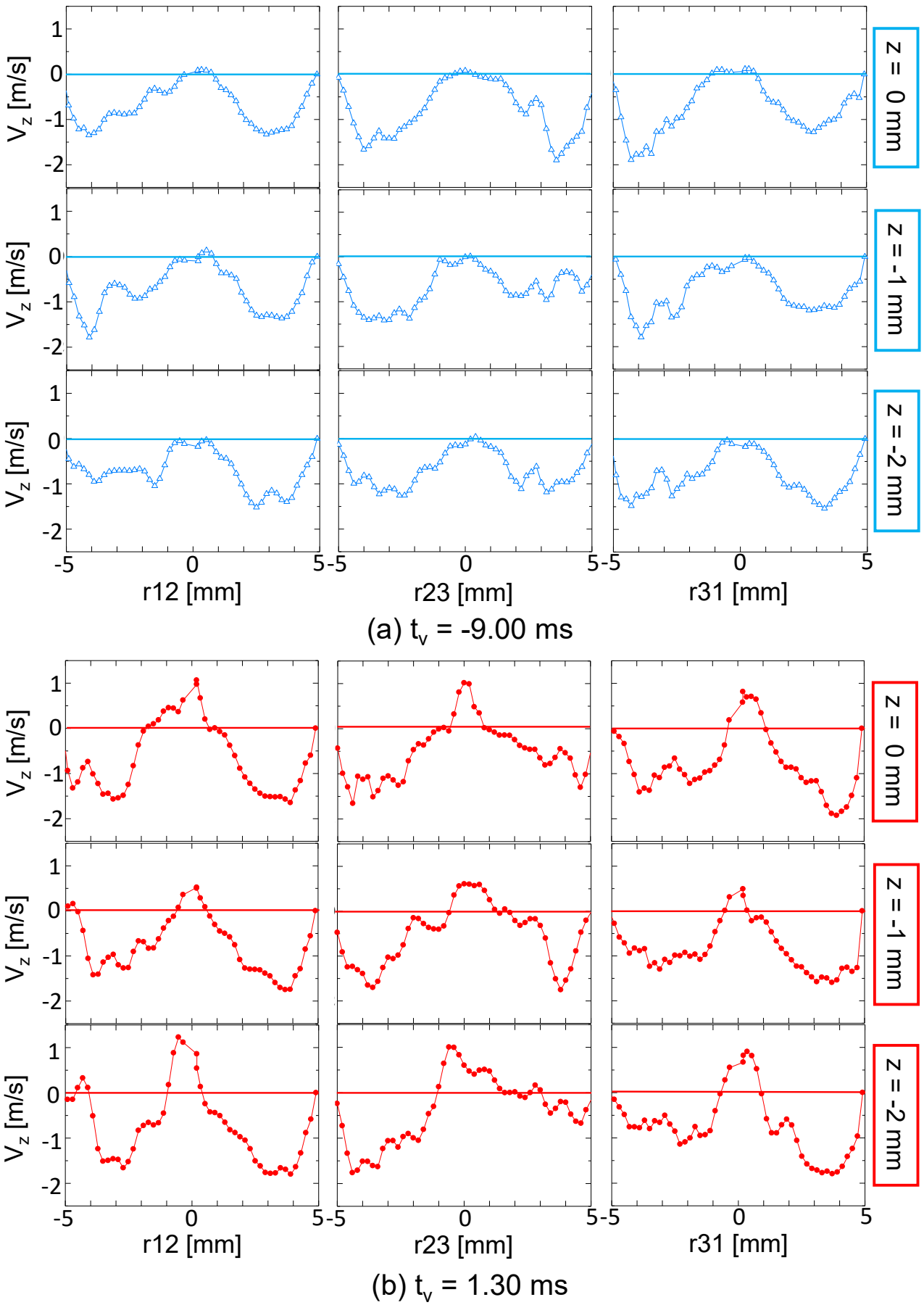

Figure 91 Instantaneous V_z radial profile at low needle lift, Z/D = 0.5, z = -2 mm

Finally, the contour and radial profile of V_z at high needle lift (Z/D =3) are shown in Figure 92 and 87, respectively. Since no string cavitation is observed at high needle lift, the virtual time parameter t_v is not needed. Measurement can be shown for continuous time history t even with the low temporal resolution, as the flow is relatively unchanged. The V_z contour is shown in Figure 92, while the radial profile of V_z is shown in Figure 93. As expected, the contour is relatively uniform across the sac. The radial profile of V_z is relatively flat, with the exceptions at the region near the sac wall. This uniform velocity field explains the non-appearance of string cavitation at high needle lift.

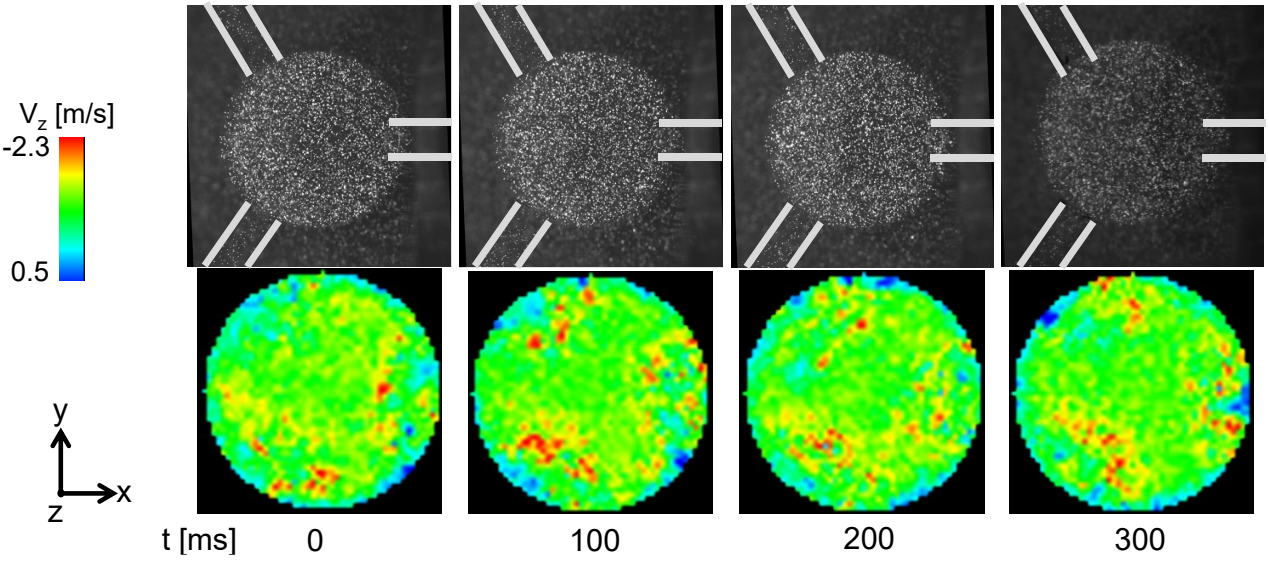

Figure 92 Instantaneous V_z contour (z = -2 mm) at high needle lift (V = 11.0 m/s)

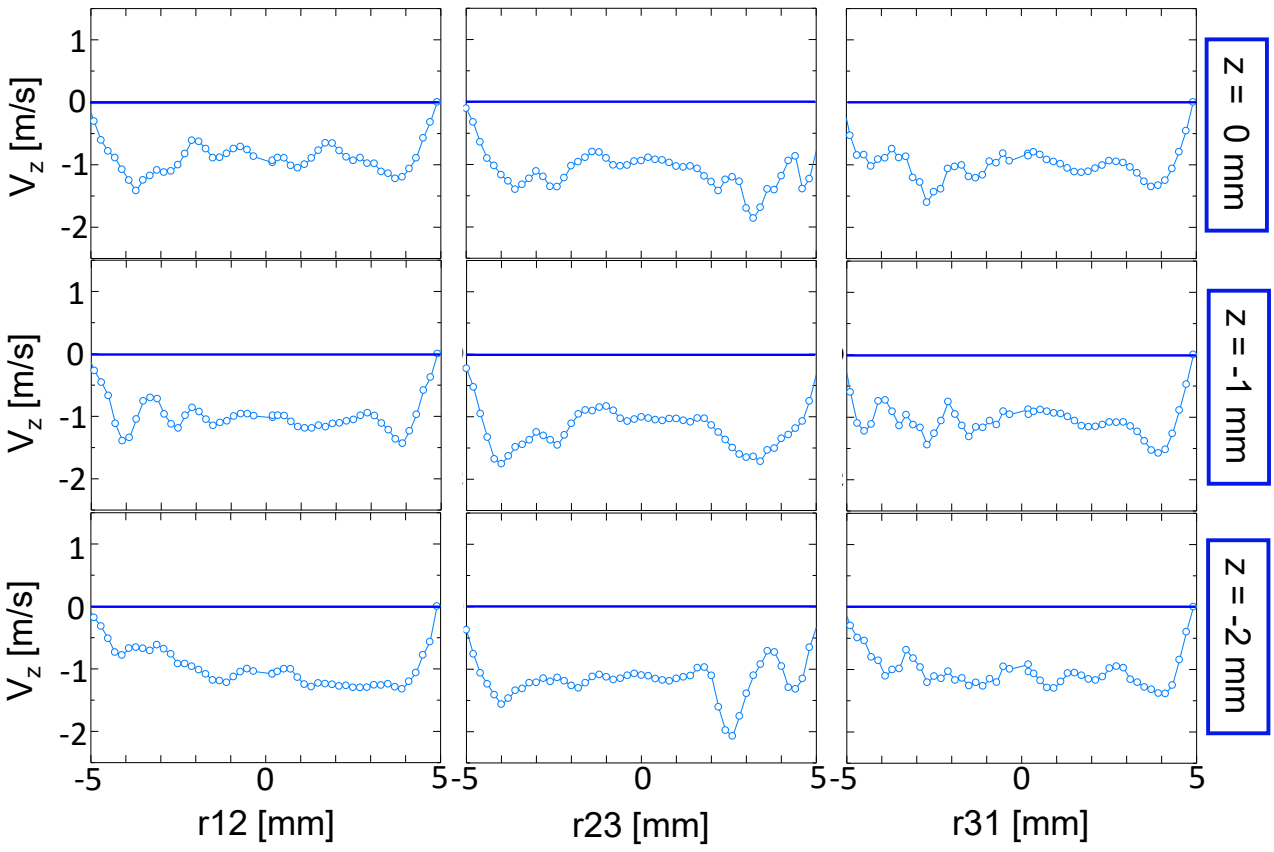

Figure 93 Instantaneous V_z radial profile at high needle lift, Z/D = 3, z = -2 mm; t = 0.00 ms

4.4 Summary

High-speed imaging of an enlarged three-hole mini-sac fuel injector and its discharged liquid jet at two different needle lifts was carried out to investigate the effect of string cavitation and geometrical cavitation to the discharged liquid jet angle. Moreover, to obtain detailed information of flow pattern inside the sac, tomographic-stereo PIV experiment in the sac was carried out. From the experimental investigations, the following results were obtained:

1. Low needle lift in fuel injector causes the formation of vortex ring flow in the sac, which may induce helical flow in the nozzle, resulting in a large liquid jet angle.
2. At the core of strong vortex ring flow in the sac, string cavitation may occur, particularly when the radial gradient of vertical velocity V_z is large. Because of this, string cavitation may serve as the indicator of vortex strength in the sac and the aforementioned increase in jet angle at low needle lift becomes large when string cavitation occurs.
3. In the case of high needle lift, flow pattern in the sac becomes relatively uniform, with small V_z gradient. This makes it harder for string cavitation to form. As a result, the liquid jet angle at high needle lift is mainly governed by geometrical cavitation.

5 CONCLUSIONS

In this dissertation, in-nozzle cavitation and its effects on discharged liquid jet was investigated using nozzles with various sizes and geometries. X-ray imaging conducted using 2D nozzles with various sizes and geometries was carried out to understand how the difference in size and upstream geometry of the nozzle affects the dynamics of cavitation bubble morphology in the nozzle. Comparison of steady and transient injection was carried out using the same nozzle, to verify the validity of studies carried out under steady injection condition. Lastly, a high-speed imaging and TSPIV of an enlarged 3-hole mini-sac diesel injector was carried out to investigate the complex flow field in injectors with realistic geometry, which can lead to the formation of string cavitation. The following conclusions were obtained:

- Under low flow velocity, in-nozzle cavitation first emerges as a cloud of individual cavitation bubbles. The bubbles have a highly distorted circumference, with slanted shapes caused by the recirculation flow velocity profile in the nozzle. As turbulent eddy scale is directly proportional to the nozzle size, the size of the bubbles tends to change in proportion to the nozzle size.
- Cavitation bubble dynamics in the nozzle is not governed by Rayleigh-Plesset equation.
- Cavitation inception process in the nozzle is caused by two kinds of heterogeneous nucleation. The first one results from an expansion of a microbubble that is trapped in the nozzle surface, while the second one results from the breakup of a bubble that enters from upstream of the nozzle and breaks up near velocity boundary layer.
- Under high flow velocity, the cloud of bubbles turned into a single large cavitation film. For mini-sac nozzle, the cavitation film has a highly distorted shape compared to cavitation film in symmetric nozzles. This is caused by stronger turbulence in the nozzle, resulting from the asymmetric inflow from the upstream of the mini-sac nozzle.
- A perturbation length scale λ was introduced to evaluate the structure of the gas-liquid interface of the wavy liquid jet core. It was found that λ is smaller at the super cavitation regime, which is caused by cavitation-induced turbulence near the nozzle exit. In addition, the normalized perturbation length scale λ/W shows that jet deformation is suppressed with the decrease in nozzle size.
- At the hydraulic flip regime, λ of the mini-sac nozzle is very small, which indicates that jet deformation still occurs. This is by the imperfect hydraulic flip, which caused in a periodic flow reattachment to the nozzle wall. Thus, a similar turbulence-inducing mechanism as those found at super cavitation regime occurs, promoting jet deformation even at hydraulic flip regime.
- Correlations obtained from steady injection data can be used to predict the growth of in-nozzle cavitation and the discharged liquid jet angle during transient injection process where the

duration of the flow rate increase is much longer than the time scale of flow development in the nozzle

- Low needle lift in fuel injector causes the formation of vortex ring flow in the sac. When the gradient of vertical velocity V_z is large, a microbubble that traveled to the core of the vortex ring will develop into a string cavitation.
- At high needle lift, the flow pattern in the sac is relatively uniform and V_z gradient is small, thus it is harder for string cavitation to form.
- The aforementioned vortex ring flow can also induce helical flow in the nozzle, resulting in a comparatively larger jet angle at low needle lift. As string cavitation is formed when there is a particularly strong vortex, the jet angle is increased further when string cavitation occurs. As this mechanism does not exist at high needle lift, the liquid jet angle at high needle lift is mainly governed by geometrical cavitation.

It was found that cavitation in the nozzle is composed of highly asymmetrical bubbles under incipient regime and cavitation films under super cavitation regime. The development of cavitation bubble scales proportionally to the nozzle size, and is not governed by the commonly used Rayleigh-Plesset equations. These findings is an important input for the development of in-nozzle cavitation numerical simulations that are commonly used for fuel injector designs. In addition, it was found that the formation of vortex ring flow in the sac was the mechanism behind string cavitation formation. Preventing such flow field from occurring in the sac (i.e. changing the inflow angle from the needle valve to prevent vortex ring flow) can help to suppress string cavitation formation. Based on these knowledge, a better strategy for next-generation fuel injector design can be obtained.

6 BIBLIOGRAPHY

[1] United Nations Framework Convention on Climate Changes, “Kyoto Protocol Status of Ratification,” 2009. .

[2] M. P. Walsh, “PM2.5: global progress in controlling the motor vehicle contribution,” *Front. Environ. Sci. Eng.*, vol. 8, no. 1, pp. 1–17, 2014.

[3] World Health Organization, “WHO Air quality guidelines for particulate matter, ozone, nitrogen dioxide and sulfur dioxide: global update 2005: summary of risk assessment,” *Geneva World Heal. Organ.*, pp. 1–22, 2006.

[4] O. Raaschou-Nielsen, “Air pollution and lung cancer incidence in 17 European cohorts: Prospective analyses from the European Study of Cohorts for Air Pollution Effects (ESCAPE),” *Lancet Oncol.*, vol. 14, no. 9, pp. 813–822, 2013.

[5] C. Shisong *et al.*, “Comparison of remotely sensed PM2.5 concentrations between developed and developing countries: Results from the US, Europe, China, and India,” *J. Clean. Prod.*, vol. 182, pp. 672–681, 2018.

[6] D. Kodjak, “Policies to Reduce Fuel Consumption, Air Pollution, And Carbon Emissions from Vehicles in G20 Nations,” 2015.

[7] I. Gilles-Birth, S. Bernhardt, U. Spicher, and M. Rechs, “A Study of the In-Nozzle Flow Characteristic of Valve Covered Orifice Nozzles for Gasoline Direct Injection,” in *SAE Technical Papers*, 2005, no. 724.

[8] G. Fontaras, N. G. Zacharof, and B. Ciuffo, “Fuel consumption and CO2 emissions from passenger cars in Europe – Laboratory versus real-world emissions,” *Prog. Energy Combust. Sci.*, vol. 60, pp. 97–131, 2017.

[9] The Economist, “Exhaustive analysis,” London, 2016.

[10] J. P. Skeete, “Examining the role of policy design and policy interaction in EU automotive emissions performance gaps,” *Energy Policy*, vol. 104, no. February, pp. 373–381, 2017.

[11] J. L. Jiménez, J. Valido, and N. Molden, “The drivers behind differences between official and actual vehicle efficiency and CO 2 emissions,” *Transp. Res. Part D Transp. Environ.*, vol. 67, no. January, pp. 628–641, 2019.

[12] E. Magdalinski, “THREE YEARS AFTER DIESELGATE: WHERE DO WE STAND?,” 2018. [Online]. Available: http://institutdelors.eu/publications/three-years-after-dieselgate-where-do-we-stand/?lang=en#_ftn13. [Accessed: 17-Apr-2019].

[13] T. Bunsen *et al.*, “Global EV Outlook 2018,” 2018.

[14] C. McKerracher, S. Morsy, N. Kou, L. Goldie-Scot, A. O’Donovan, and D. Doherty, “Electric Vehicle Outlook: 2018,” *BloombergNEF*, 2018. [Online]. Available: https://bnef.turtl.co/story/evo2018. [Accessed: 16-Apr-2019].

[15] T. Hazeldine, S. Kollamthodi, C. Brannigan, M. Morris, and L. Deller, “Market outlook to 2022 for battery electric vehicles and plug-in hybrid electric vehicles (Final Report to the Committee

on Climate Change)," 2009.

[16] G. Haddadian, M. Khodayar, and M. Shahidehpour, "Accelerating the Global Adoption of Electric Vehicles: Barriers and Drivers," *Electr. J.*, vol. 28, no. 10, pp. 53–68, 2015.

[17] W. Sierzchula, S. Bakker, K. Maat, and B. Van Wee, "The influence of financial incentives and other socio-economic factors on electric vehicle adoption," *Energy Policy*, vol. 68, pp. 183–194, 2014.

[18] P. Lebeau, C. Macharis, and J. Van Mierlo, "Exploring the choice of battery electric vehicles in city logistics: A conjoint-based choice analysis," *Transp. Res. Part E Logist. Transp. Rev.*, vol. 91, pp. 245–258, 2016.

[19] K. Y. Bjerkan, T. E. Nørbech, and M. E. Nordtømme, "Incentives for promoting Battery Electric Vehicle (BEV) adoption in Norway," *Transp. Res. Part D Transp. Environ.*, vol. 43, pp. 169–180, 2016.

[20] W. Li, R. Long, H. Chen, and J. Geng, "A review of factors influencing consumer intentions to adopt battery electric vehicles," *Renew. Sustain. Energy Rev.*, vol. 78, no. April, pp. 318–328, 2017.

[21] T. Higgins and C. Rollet, "Tesla Sales Fall to Zero in Hong Kong After Tax Break Is Slashed," *The Wall Street Journal*, 2017. [Online]. Available: https://www.wsj.com/articles/teslas-hong-kong-sales-gutted-by-tax-change-1499598003. [Accessed: 17-Apr-2019].

[22] N. E. Boudette, "Tesla Sales Slump as '19 Starts Is Hinted At in State Data," *The New York Times*, 2019. [Online]. Available: https://www.nytimes.com/2019/03/22/business/tesla-sales.html. [Accessed: 17-Apr-2019].

[23] Deloitte, "21 million more electric vehicles expected worldwide by 2030," 2019. [Online]. Available: https://www2.deloitte.com/uk/en/pages/press-releases/articles/21-million-more-electric-vehicles-expected-worldwide-by-2030.html. [Accessed: 17-Apr-2019].

[24] B. K. Sovacool, "The History and Politics of Energy Transitions: Comparing Contested Views and Finding Common Ground," *Polit. Econ. Clean Energy Transitions*, no. June, pp. 16–35, 2017.

[25] A. H. Lefebvre and V. G. McDonnell, *Atomization and Sprays*, 2nd ed. Taylor & Francis, 2017.

[26] H. Whitelaw, F. Payri, and C. Arcoumanis, *Thermo- and Fluid Dynamic Processes in Diesel Engines 2*. New York: Springer-Verlag, 2004.

[27] S. Moon, Y. Gao, S. Park, J. Wang, N. Kurimoto, and Y. Nishijima, "Effect of the number and position of nozzle holes on in- and near-nozzle dynamic characteristics of diesel injection," *Fuel*, vol. 150, pp. 112–122, 2015.

[28] N. Mitroglou, M. Gavaises, J. M. Nouri, and C. Arcoumanis, "Cavitation Inside Enlarged And Real-Size Fully Transparent Injector Nozzles And Its Effect On Near Nozzle Spray Formation," in *Droplet Impact Phenomena and Spray Investigations Workshop 2011*, 2011.

[29] A. Sou *et al.*, "X-Ray Visualization of Cavitation in Nozzles with Various Sizes," in *Proceedings of 13th International Conference on Liquid Atomization and Spray Systems (ICLASS 2015)*,

2015.

[30] R. Prasetya, A. Sou, S. Moon, R. H. Pratama, Y. Wada, and H. Yokohata, “X-Ray Phase Contrast Imaging of Cavitation and Discharged Liquid Jet in Nozzles with Various Sizes,” *Atomization and Sprays*, vol. 29, no. 1, pp. 59–78, 2019.

[31] A. R. Osta, J. Lee, K. A. Sallam, and K. Fezzaa, “Study of the effects of the injector length/diameter ratio on the surface properties of turbulent liquid jets in still air using X-ray imaging,” *Int. J. Multiph. Flow*, vol. 38, no. 1, pp. 87–98, Jan. 2012.

[32] K.-S. Im, S.-K. Cheong, C. F. Powell, M.-C. D. Lai, and J. Wang, “Unraveling the geometry dependence of in-nozzle cavitation in high-pressure injectors.,” *Sci. Rep.*, vol. 3, p. 2067, 2013.

[33] R. Prasetya, M. Mashida, Y. Yamada, and A. Sou, “Effect of Nozzle Inlet Roundness and Nozzle Length on Cavitation and Liquid Jet,” in *Proceedings of 13th International Conference on Liquid Atomization and Spray Systems (ICLASS 2015)*, 2015.

[34] H. Chaves, F. Bauz, and E. M. Lopez, “Scaling of Cavitation in Nozzles Depending on Rounding of the Inlet and on Fuel Properties Using Transparent Nozzles,” in *Proceedings of 27th European Conference on Liquid Atomization and Spray Systems (ILASS-Europe 2016)*, 2016, no. September.

[35] D. P. Schmidt and M. L. Corradini, “The internal flow of diesel fuel injector nozzles: A review,” *Int. J. Engine Res.*, vol. 2, no. 1, pp. 1–22, 2001.

[36] J. I. Thornycroft and S. W. Barnaby, “Torpedo-Boat Destroyers,” *J. Am. Soc. Nav. Eng.*, vol. 14, no. 2, pp. 396–408, 2010.

[37] C. E. Brennen, *Cavitation and bubble dynamics*. New York: Oxford University Press, 1995.

[38] J. Rooze, E. V. Rebrov, J. C. Schouten, and J. T. F. Keurentjes, “Dissolved gas and ultrasonic cavitation - A review,” *Ultrason. Sonochem.*, vol. 20, no. 1, pp. 1–11, 2013.

[39] J. P. Padilla-Martinez, C. Berrospe-Rodriguez, G. Aguilar, J. C. Ramirez-San-Juan, and R. Ramos-Garcia, “Optic cavitation with CW lasers: A review,” *Phys. Fluids*, vol. 26, no. 12, 2014.

[40] S. Li, C. E. Brennen, and Y. Matsumoto, “Introduction for amazing (cavitation) bubbles,” *Interface Focus*, vol. 5, no. 5, p. 20150059, Oct. 2015.

[41] Lord Rayleigh, “On the pressure developed in a liquid during the collapse of a spherical cavity,” *London, Edinburgh, Dublin Philos. Mag. J. Sci.*, vol. 34, no. 200, pp. 94–98, 1917.

[42] M. S. Plesset, “The Dynamics of Cavitation Bubbles,” *ASME J. Appl. Mech.*, vol. 16, pp. 228–231, 1949.

[43] W. LAUTERBORN and A. PHILIPP, “Cavitation erosion by single laser-produced bubbles,” *J. Fluid Mech.*, vol. 361, pp. 75–116, 1998.

[44] P. Ignaciuk and L. Gil, “Damages To Injectors in Diesel Engines,” *Adv. Sci. Technol. Res. J.*, vol. 8, no. 21, pp. 58–61, 2014.

[45] M. Gavaises, D. Papoulias, A. Andriotis, E. Giannadakis, and A. Theodorakakos, “Link Between Cavitation Development and Erosion Damage in Diesel Injector Nozzles,” in *SAE Technical Papers*, 2007, vol. 2007, no. 724, pp. 776–790.

[46] M. Arai, *Physics Behind Diesel Spray and Its Combustion*. Saarbrücken: Lambert Academic Publishing, 2016.

[47] A. Andriotis and M. Gavaises, “Influence of vortex flow and cavitation on near-nozzle diesel spray dispersion angle,” *Atomization and Sprays*, vol. 19, no. 3, pp. 247–261, 2009.

[48] C. Soteriou, R. J. Andrews, N. Torres, M. Smith, and R. Kunkulagunta, “Through the Diesel Nozzle Hole - A Journey of Discovery II,” in *Proceedings of 17th European Conference on Liquid Atomization and Spray Systems (ILASS-Europe 2001)*, 2001, no. September.

[49] C. Arcoumanis, H. Flora, M. Gavaises, and M. Badami, “Cavitation in Real-Size Multi-Hole Diesel Injector Nozzles,” in *SAE Technical Papers*, 2000, no. 724.

[50] R. H. Pratama, A. Sou, T. Katsui, and S. Nishio, “String cavitation in a fuel injector,” *Atomization and Sprays*, vol. 27, no. 3, pp. 189–205, 2017.

[51] A. Andriotis, M. Gavaises, and C. Arcoumanis, “Vortex flow and cavitation in diesel injector nozzles,” *J. Fluid Mech.*, vol. 610, no. August 2008, pp. 195–215, Sep. 2008.

[52] N. Mitroglou, M. McLorn, M. Gavaises, C. Soteriou, and M. Winterbourne, “Instantaneous and ensemble average cavitation structures in Diesel micro-channel flow orifices,” *Fuel*, vol. 116, pp. 736–742, 2014.

[53] H. Watanabe, M. Nishikori, T. Hayashi, M. Suzuki, N. Kakehashi, and M. Ikemoto, “Visualization analysis of relationship between vortex flow and cavitation behavior in diesel nozzle,” *Int. J. Engine Res.*, vol. 16, no. 1, pp. 5–12, 2015.

[54] Z. He, Z. Zhang, G. Guo, Q. Wang, X. Leng, and S. Sun, “Visual Experiment of Transient Cavitating Flow in the Real-Size Diesel Injector Nozzle,” *Int. Commun. Heat Mass Transf.*, vol. 78, pp. 13–20, 2016.

[55] Y. Gao, M. Wei, F. Yan, L. Chen, G. Li, and L. Feng, “Effects of cavitation flow and stagnant bubbles on the initial temporal evolution of diesel spray,” *Exp. Therm. Fluid Sci.*, vol. 87, pp. 69–79, 2017.

[56] C. Wang, A. Moro, F. Xue, X. Wu, and F. Luo, “The influence of eccentric needle movement on internal flow and injection characteristics of a multi-hole diesel nozzle,” *Int. J. Heat Mass Transf.*, vol. 117, pp. 818–834, 2018.

[57] C. Arcoumanis, H. Flora, M. Gavaises, N. Kampanis, and R. Horrocks, “Investigation of Cavitation in a Vertical Multi-Hole Injector,” in *SAE Technical Papers*, 1999, vol. 108, pp. 661–678.

[58] R. E. A. Arndt, “Cavitation in Vortical Flows,” *Annu. Rev. Fluid Mech.*, vol. 34, no. 1, pp. 143–175, Jan. 2002.

[59] J. Choi, C. T. Hsiao, G. Chahine, and S. Ceccio, “Growth, oscillation and collapse of vortex cavitation bubbles,” *J. Fluid Mech.*, vol. 624, pp. 255–279, 2009.

[60] M. Linne, “Imaging in the optically dense regions of a spray: A review of developing techniques,” *Prog. Energy Combust. Sci.*, vol. 39, no. 5, pp. 403–440, 2013.

[61] K. H. Goney and M. L. Corradini, “Isolated Effects of Ambient Pressure, Nozzle Cavitation and

Hole Inlet Geometry on Diesel Injection Spray Characteristics," in *SAE Technical Papers*, 2000, no. 724.

[62] F. Payri, V. Bermúdez, R. Payri, and F. J. Salvador, "The influence of cavitation on the internal flow and the spray characteristics in diesel injection nozzles," *Fuel*, vol. 83, no. 4–5, pp. 419–431, 2004.

[63] Y. Chen and S. D. Heister, "Two-phase modeling of cavitated flows," *Comput. Fluids*, vol. 24, no. 7, pp. 799–809, 1995.

[64] A. Niedzwiedzka, G. H. Schnerr, and W. Sobieski, "Review of numerical models of cavitating flows with the use of the homogeneous approach," *Arch. Thermodyn.*, vol. 37, no. 2, pp. 71–88, 2016.

[65] D. P. Schmidt, C. J. Rutland, and M. L. Corradini, "A Numerical Study of Cavitating Flow Through Various Nozzle Shapes," in *SAE Technical Papers*, 1997.

[66] D. P. Schmidt, C. J. Rutland, M. L. Corradini, P. Roosen, and O. Genge, "Cavitation in Two-Dimensional Asymmetric Nozzles," in *SAE Technical Papers*, 1999.

[67] F. Payri, X. Margot, S. Patouna, F. Ravet, and M. Funk, "A CFD Study of the Effect of the Needle Movement on the Cavitation Pattern of Diesel Injectors," in *SAE Technical Papers*, 2009.

[68] E. Giannadakis, M. Gavaises, and C. Arcoumanis, "Modelling of cavitation in diesel injector nozzles," *J. Fluid Mech.*, vol. 616, pp. 153–193, 2008.

[69] D. J. Duke, D. P. Schmidt, K. Neroorkar, A. L. Kastengren, and C. F. Powell, "High-resolution large eddy simulations of cavitating gasoline-ethanol blends," *Int. J. Engine Res.*, vol. 14, no. 6, pp. 578–589, 2013.

[70] F. Örley, T. Trummler, S. Hickel, M. S. Mihatsch, S. J. Schmidt, and N. A. Adams, "Large-eddy simulation of cavitating nozzle flow and primary jet break-up," *Phys. Fluids*, vol. 27, no. 8, 2015.

[71] P. Koukouvinis, M. Gavaises, J. Li, and L. Wang, "Large Eddy Simulation of Diesel injector including cavitation effects and correlation to erosion damage," *Fuel*, vol. 175, pp. 26–39, 2016.

[72] H. Vahedi Tafreshi and B. Pourdeyhimi, "The effects of nozzle geometry on waterjet breakup at high Reynolds numbers," *Exp. Fluids*, vol. 35, no. 4, pp. 364–371, 2003.

[73] L. Postrioti, F. Mariani, and M. Battistoni, "Experimental and numerical momentum flux evaluation of high pressure Diesel spray," *Fuel*, vol. 98, pp. 149–163, 2012.

[74] M. Battistoni, Q. Xue, S. Som, and E. Pomraning, "Effect of Off-Axis Needle Motion on Internal Nozzle and Near Exit Flow in a Multi-Hole Diesel Injector," *SAE Int. J. Fuels Lubr.*, vol. 7, no. 1, pp. 2014-01–1426, 2014.

[75] P. Dong, T. Inaba, K. Nishida, and D. Shimo, "Characteristics of the internal flow and the near-field spray of a single-hole injector and a multi-hole injector for diesel engines," *Proc. Inst. Mech. Eng. Part D J. Automob. Eng.*, vol. 230, no. 5, pp. 632–649, 2016.

[76] J.-C. Chang, S.-B. Huang, and C.-M. Lin, “Effects of Inlet Surface Roughness, Texture, and Nozzle Material on Cavitation,” *Atomization and Sprays*, vol. 16, no. 3, pp. 299–318, 2006.

[77] W. Bergwerk, “Flow Pattern in Diesel Nozzle Spray Holes,” *Proc. Inst. Mech. Eng.*, vol. 173, no. 1, pp. 655–660, 1959.

[78] W. H. Nurick, “Orifice Cavitation and Its Effect on Spray Mixing,” *J. Fluids Eng.*, vol. 98, no. 4, p. 681, 1976.

[79] H. Hiroyasu, M. Arai, and M. Shimizu, “Break-up Length of a Liquid Jet and Internal Flow in a Nozzle,” in *Proceedings of 5th International Conference on Liquid Atomization and Spray Systems (ICLASS 1991)*, 1991, pp. 275–282.

[80] H. Hiroyasu, M. Arai, and M. Shimizu, “Effect of Internal Flow Conditions Inside Injector Nozzles on Jet Breakup Processes,” *Recent Advances in Spray Combustion: Spray Atomization and Drop Burning Phenomena Volume I*. pp. 173–184, 1996.

[81] H. Chaves, M. Knapp, A. Kubitzek, F. Obermeier, and T. Schneider, “Experimental Study of Cavitation in the Nozzle Hole of Diesel Injectors Using Transparent Nozzles,” in *SAE Technical Papers*, 1995.

[82] C. Soteriou, R. Andrews, and M. Smith, “Direct Injection Diesel Sprays and the Effect of Cavitation and Hydraulic Flip on Atomization,” in *SAE Technical Papers*, 1995, no. 412.

[83] H. Roth, M. Gavaises, and C. Arcoumanis, “Cavitation Initiation, Its Development and Link with Flow Turbulence in Diesel Injector Nozzles,” in *SAE Technical Papers*, 2002.

[84] S. H. Park, H. K. Suh, and C. S. Lee, “Effect of cavitating flow on the flow and fuel atomization characteristics of biodiesel and diesel fuels,” *Energy and Fuels*, vol. 22, no. 1, pp. 605–613, 2008.

[85] Z. He, Z. Shao, Q. Wang, W. Zhong, and X. Tao, “Experimental study of cavitating flow inside vertical multi-hole nozzles with different length-diameter ratios using diesel and biodiesel,” *Exp. Therm. Fluid Sci.*, vol. 60, pp. 252–262, 2015.

[86] X. Zhang *et al.*, “Effect of fuel temperature on cavitation flow inside vertical multi-hole nozzles and spray characteristics with different nozzle geometries,” *Exp. Therm. Fluid Sci.*, vol. 91, pp. 374–387, 2018.

[87] C. Badock, R. Wirth, A. Fath, and A. Leipertz, “Investigation of cavitation in real size diesel injection nozzles,” *Int. J. Heat Fluid Flow*, vol. 20, no. 5, pp. 538–544, 1999.

[88] M. Gavaises, C. Arcoumanis, and E. Abo-Serie, “Nozzle Hole Film Formation and its Link to Spray Characteristics in Swirl-Pressure Atomizers for Direct Injection Gasoline Engines,” in *SAE Technical Papers*, 2002.

[89] H. Chaves, R. Miranda, and R. Knake, “Particle Image Velocimetry Measurements of the Cavitating Flow in a Real Size Transparent VCO Nozzle,” in *Proceedings of 6th International Conference on Multiphase Flow*, 2007.

[90] T. Hayashi, M. Suzuki, and M. Ikemoto, “Effects of internal flow in a diesel nozzle on spray combustion,” *Int. J. Engine Res.*, vol. 14, no. 6, pp. 646–654, 2013.

[91] S. Moon, W. Huang, and J. Wang, “First observation and characterization of vortex flow in steel micronozzles for high-pressure diesel injection,” *Exp. Therm. Fluid Sci.*, vol. 105, no. July 2018, pp. 342–348, 2019.

[92] L. C. Ganippa, G. Bark, S. Andersson, and J. Chomiak, “The Structure of Cavitation and its Effect on the Spray Pattern in a Single-Hole Diesel Nozzle,” in *SAE Technical Papers*, 2001.

[93] A. Sou and R. H. Pratama, “Effects of Asymmetric Inflow on Cavitation in Fuel Injector and Discharged Liquid Jet,” *Atomization and Sprays*, vol. 26, no. 9, pp. 939–959, 2016.

[94] N. Mitroglou, V. Stamboliyski, I. K. Karathanassis, K. S. Nikas, and M. Gavaises, “Cloud cavitation vortex shedding inside an injector nozzle,” *Exp. Therm. Fluid Sci.*, vol. 84, pp. 179–189, 2017.

[95] A. Sou, M. I. Maulana, S. Hosokawa, and A. Tomiyama, “Ligament Formation Induced by Cavitation in a Cylindrical Nozzle,” *Journal of Fluid Science and Technology*, vol. 3, no. 5, pp. 633–644, 2008.

[96] A. Sou, A. Tomiyama, S. Hosokawa, S. Nigorikawa, and M. Tatsutoshi, “Cavitation in a Two-Dimensional Nozzle and Liquid Jet Atomization,” *JSME Int. J. Ser. B Fluids Therm. Eng.*, vol. 49, no. 4, pp. 1253–1259, 2006.

[97] A. Sou, S. Hosokawa, and A. Tomiyama, “Effects of cavitation in a nozzle on liquid jet atomization,” *Int. J. Heat Mass Transf.*, vol. 50, no. 17–18, pp. 3575–3582, 2007.

[98] A. Sou, M. I. Maulana, K. Isozaki, S. Hosokawa, and A. Tomiyama, “Effects of Nozzle Geometry on Cavitation in Nozzles of Pressure Atomizers,” *Journal of Fluid Science and Technology*, vol. 3, no. 5, pp. 622–632, 2008.

[99] A. Sou, S. Hosokawa, and A. Tomiyama, “Cavitation in Nozzles of Plain Orifice Atomizers with Various Length-to-Diameter Ratios,” *Atomization and Sprays*, vol. 20, no. 6, pp. 513–524, 2010.

[100] U. Iben, A. Morozov, E. Winklhofer, and F. Wolf, “Laser-pulse interferometry applied to high-pressure fluid flow in micro channels,” *Exp. Fluids*, vol. 50, no. 3, pp. 597–611, 2011.

[101] C. Mauger, L. Mees, M. Michard, A. Azouzi, and S. Valette, “Shadowgraph, Schlieren and interferometry in a 2D cavitating channel flow,” *Exp. Fluids*, vol. 53, no. 6, pp. 1895–1913, 2012.

[102] C. Mauger, L. Méès, M. Michard, and M. Lance, “Velocity measurements based on shadowgraph-like image correlations in a cavitating micro-channel flow,” *Int. J. Multiph. Flow*, vol. 58, pp. 301–312, 2014.

[103] B. A. Reid, G. K. Hargrave, C. P. Garner, and G. Wigley, “An investigation of string cavitation in a true-scale fuel injector flow geometry at high pressure,” *Phys. Fluids*, vol. 22, no. 3, pp. 1–3, 2010.

[104] B. A. Reid, G. K. Hargrave, C. P. Garner, and R. M. McDavid, “An optical comparison of the cavitation characteristics of diesel and bio-diesel blends in a true-scale nozzle geometry,” *Int. J. Engine Res.*, vol. 14, no. 6, pp. 622–629, 2013.

[105] B. A. Reid *et al.*, “On the formation of string cavitation inside fuel injectors,” *Exp. Fluids*, vol. 55, no. 1, pp. 1–8, 2014.

[106] C. Arcoumanis, M. Gavaises, J. M. Nouri, E. Abdul-Wahab, and R. W. Horrocks, “Analysis of the Flow in the Nozzle of a Vertical Multi-Hole Diesel Engine Injector,” in *SAE Technical Papers*, 1998.

[107] T. Hayashi, M. Suzuki, and M. Ikemoto, “Visualization of Internal Flow and Spray Formation with Real Size Diesel Nozzle,” in *Proceedings of 12th International Conference on Liquid Atomization and Spray Systems (ICLASS 2012)*, 2012.

[108] Z. Falgout and M. Linne, “Novel design for transparent high-pressure fuel injector nozzles,” *Rev. Sci. Instrum.*, vol. 87, no. 8, 2016.

[109] R. Budwig, “Refractive index matching methods for liquid flow investigations,” *Exp. Fluids*, vol. 17, no. 5, pp. 350–355, Sep. 1994.

[110] R. Payri, F. J. Salvador, J. Gimeno, and O. Venegas, “A Technique to Match the Refractive Index of Different Diesel Fuels with the Refractive Index of Transparent Materials to Improve the Experimental Visualization,” *Exp. Tech.*, vol. 40, no. 1, pp. 261–269, 2013.

[111] T. J. Heindel, “A Review of X-Ray Flow Visualization With Applications to Multiphase Flows,” *J. Fluids Eng.*, vol. 133, no. 7, p. 074001, 2011.

[112] A. Kastengren and C. F. Powell, “Synchrotron X-ray techniques for fluid dynamics,” *Exp. Fluids*, vol. 55, no. 3, 2014.

[113] D. J. Duke, A. L. Kastengren, F. Z. Tilocco, A. B. Swantek, and C. F. Powell, “X-Ray Radiography Measurements of Cavitating Nozzle Flow,” *Atomization and Sprays*, vol. 23, no. 9, pp. 841–860, 2013.

[114] D. J. Duke *et al.*, “X-ray radiography of cavitation in a beryllium alloy nozzle,” *Int. J. Engine Res.*, vol. 18, no. 1–2, pp. 39–50, Feb. 2017.

[115] M. Battistoni, D. J. Duke, A. B. Swantek, F. Z. Tilocco, C. F. Powell, and S. Som, “Effects of Noncondensable Gas on Cavitating Nozzles,” *Atomization and Sprays*, vol. 25, no. 6, pp. 453–483, 2015.

[116] D. J. Duke, A. Swantek, A. Kastengren, K. Fezzaa, and C. Powell, “Recent Developments in X-ray Diagnostics for Cavitation,” *SAE Int. J. Fuels Lubr.*, vol. 8, no. 1, pp. 135–146, 2015.

[117] D. J. Duke, A. L. Kastengren, A. B. Swantek, K. E. Matusik, and C. F. Powell, “X-ray fluorescence measurements of dissolved gas and cavitation,” *Exp. Fluids*, vol. 57, no. 10, pp. 1–14, 2016.

[118] D. J. Duke, A. L. Kastengren, K. E. Matusik, and C. F. Powell, “Hard X-ray fluorescence spectroscopy of high pressure cavitating fluids in aluminum nozzles,” *Int. J. Multiph. Flow*, vol. 0, pp. 1–11, 2018.

[119] D. J. Duke *et al.*, “X-ray Imaging of Cavitation in Diesel Injectors,” *SAE Int. J. Engines*, vol. 7, no. 2, pp. 2014-01–1404, 2014.

[120] S. Moon *et al.*, “High-Speed X-ray Imaging of In-Nozzle Cavitation and Emerging Jet Flow of

Multi-Hole GDI Injector under Practical Operating Conditions," in *Proceedings of 13th International Conference on Liquid Atomization and Spray Systems (ICLASS 2015)*, 2015.

[121] S. Minami, R. H. Pratama, R. Prasetya, A. Sou, T. Miwa, and S. Moon, "X-Ray Visualization and Effects of Nozzle Size on Cavitation," in *Proceedings of the 24th ILASS-Japan Symposium*, 2015.

[122] I. K. Karathanassis *et al.*, "High-speed visualization of vortical cavitation using synchrotron radiation," *J. Fluid Mech.*, vol. 838, pp. 148–164, 2018.

[123] I. K. Karathanassis, K. Trickett, P. Koukouvinis, J. Wang, R. Barbour, and M. Gavaises, "Illustrating the effect of viscoelastic additives on cavitation and turbulence with X-ray imaging," *Sci. Rep.*, vol. 8, no. 1, pp. 1–15, 2018.

[124] H. Naseri *et al.*, "Turbulence and Cavitation Suppression by Quaternary Ammonium Salt Additives," *Sci. Rep.*, vol. 8, no. 1, pp. 1–15, 2018.

[125] W. Merzkirch, *Flow Visualization*, 2nd ed. Orlando, Florida: Acadmic Press, Inc., 1987.

[126] M. P. Dudukovic, "Opaque Multiphase Reactors: Experimentation, Modeling and Troubleshooting," *Oil Gas Sci. Technol.*, vol. 55, no. 2, pp. 135–138, 2000.

[127] A. J. Smits and T. T. Lim, *Flow Visualization: Techniques and Examples*, 2nd ed. London, UK: Imperial College Press, 2012.

[128] M. Raffel, C. E. Willert, F. Scarano, C. J. Kähler, S. T. Wereley, and J. Kompenhans, *Particle Image Velocimetry: A Practical Guide*, 3rd ed. Cham: Springer International Publishing, 2018.

[129] R. J. Adrian, "Twenty years of particle image velocimetry," *Exp. Fluids*, vol. 39, no. 2, pp. 159–169, 2005.

[130] A. K. Prasad, "Stereoscopic particle image velocimetry," *Exp. Fluids*, vol. 29, no. 2, pp. 103–116, 2000.

[131] H. Hu, T. Saga, T. Kobayashi, N. Taniguchi, and M. Yasuki, "Dual-plane stereoscopic particle image velocimetry: System set-up and its application on a lobed jet mixing flow," *Exp. Fluids*, vol. 31, no. 3, pp. 277–293, 2001.

[132] N. Yamamoto and K. Nishino, "Tomographic stereo PIV measurements of the turbulent flow around a pitched-blade turbine," in *Proceedings of 12th International Symposium on Particle Image Velocimetry, ISPIV 2017*, 2017.

[133] A. Snigirev, I. Snigireva, V. Kohn, S. Kuznetsov, and I. Schelokov, "On the possibilities of x-ray phase contrast microimaging by coherent high-energy synchrotron radiation," *Rev. Sci. Instrum.*, vol. 66, no. 12, pp. 5486–5492, 1995.

[134] P. Cloetens, R. Barrett, J. Baruchel, J.-P. Guigay, and M. Schlenker, "Phase Objects in Synchroton Radiation Hard X-ray Imaging," *J. Phys. D. Appl Phys*, vol. 29, pp. 133–146, 1996.

[135] A. Vabre *et al.*, "Synchrotron ultra-fast X-ray imaging of a cavitating flow in a Venturi profile," *Nucl. Instruments Methods Phys. Res. Sect. A Accel. Spectrometers, Detect. Assoc. Equip.*, vol. 607, no. 1, pp. 215–217, 2009.

[136] K. Inoue *et al.*, "Present status of high flux beamline (BL40XU) at SPring-8," *Nucl. Instruments*

Methods Phys. Res. Sect. A Accel. Spectrometers, Detect. Assoc. Equip., vol. 467–468, pp. 674–677, 2001.

[137] T. Salditt, K. Giewekemeyer, C. Fuhse, S. P. Krüger, R. Tucoulou, and P. Cloetens, "Projection phase contrast microscopy with a hard x-ray nanofocused beam: Defocus and contrast transfer," *Phys. Rev. B - Condens. Matter Mater. Phys.*, vol. 79, no. 18, pp. 1–6, 2009.

[138] RIKEN, "BL40XU OUTLINE," 2018. [Online]. Available: http://www.spring8.or.jp/wkg/BL40XU/instrument/lang-en/INS-0000000353/instrument_summary_view.

[139] O. Coutier-Delgosha *et al.*, "Local Measurements in Cavitating Flow by Ultra-Fast X-Ray Imaging," in *Proceedings of the ASME 2009 Fluids Engineering Division Summer Meeting - FEDSM2009*, 2009.

[140] M. Dular, I. Khlifa, S. Fuzier, M. Adama Maiga, and O. Coutier-Delgosha, "Scale effect on unsteady cloud cavitation," *Exp. Fluids*, vol. 53, no. 5, pp. 1233–1250, 2012.

[141] R. H. Pratama, "Cavitation in a Nozzle of Fuel Injector for Diesel Engine," Kobe University, 2016.

[142] M. P. Olbinado *et al.*, "MHz frame rate hard X-ray phase-contrast imaging using synchrotron radiation," *Opt. Express*, vol. 25, no. 12, p. 13857, Jun. 2017.

[143] M. Nikl, "Scintillation detectors for x-rays," *Meas. Sci. Technol.*, vol. 17, no. 4, 2006.

[144] N. Otsu, "A Threshold Selection Method from Gray-Level Histograms," *IEEE Trans. Syst. Man. Cybern.*, vol. 9, no. 1, pp. 62–66, 1979.

[145] T. Yoda, "Reduction of Diesel Combustion Noise by Controlling Fuel Injection," *Denso Tech. Rev.*, vol. 15, pp. 110–114, 2010.

[146] R. Prasetya *et al.*, "X-Ray Imaging and Measurement of Cavitation Flow in Fuel Injector Nozzles with Various Geometries," in *Proceedings of 19th Annual Conference of ILASS-Asia (ILASS-Asia 2017)*, 2017.

[147] M. Gavaises, A. Andriotis, D. Papoulias, N. Mitroglou, and A. Theodorakakos, "Characterization of string cavitation in large-scale Diesel nozzles with tapered holes," *Phys. Fluids*, vol. 21, no. 5, 2009.

[148] X. Zhang, S. Moon, J. Gao, E. M. Dufresne, K. Fezzaa, and J. Wang, "Experimental study on the effect of nozzle hole-to-hole angle on the near-field spray of diesel injector using fast X-ray phase-contrast imaging," *Fuel*, vol. 185, pp. 142–150, 2016.

[149] N. Mitroglou and M. Gavaises, "Mapping of cavitating flow regimes in injectors for medium-/heavy-duty diesel engines," *Int. J. Engine Res.*, vol. 14, no. 6, pp. 590–605, 2013.